

Measuring Neutron Polarisation in Deuteron Photo-disintegration with the CLAS Start Counter

William Andrew Booth

Doctor of Philosophy

University of York
School of Physics, Engineering and Technology

September 2024

Abstract

Deuteron photo-disintegration ($\gamma d \rightarrow np$) is a reaction that represents the simplest case in which nuclear and hadron physics models can be tested. Despite this, associated polarisation analyses are limited in terms of angular coverage and energy ranges, especially in observables related to the recoil neutron. This is largely due to a lack in dedicated polarimetry equipment, and represents a roadblock in global progress to understand high-energy phenomena such as hexaquarks, and quark-gluon degrees of freedom.

To address this problem, this PhD thesis pioneers a new methodology for the parasitic measurement of nucleon polarisation using kinematic reconstruction of (spin-dependent) nucleon-nucleus scattering of reaction products, prior to their detection in large acceptance particle detector apparatus. Following this novel approach, which requires no dedicated polarimeter, a determination of the double polarisation observable, C_{χ}^n , from deuteron photo-disintegration is presented, using Jefferson Lab's CLAS detector. The analysis utilises the (n,p) charge exchange reaction in CLAS's "start counter" (plastic scintillator) to determine the final state neutron polarisations. The results present the first ever data for this observable above 0.7 GeV (photon beam energy) and significantly extend the angular range of the world data set. This new data is largely statistically consistent with the previous measurement of C_{χ}^n by Bashkanov *et al.* [1] in the overlapping energy range of 0.4-0.7 GeV.

It is planned for the statistical accuracy of the presented result to be increased by the inclusion of additional data. The analysis herein serves as a key proof of concept for future applications, including a recommended similar analysis to be implemented with data from the more modern CLAS12 detector. This paves the way for a plethora of additional analyses using existing data sets that would provide crucial new constraints for hadron and nuclear physics.

Table of contents

Abstract	i
List of figures	vii
List of tables	xi
Acknowledgements	xiii
Declaration	xv
1 Introduction	1
1.1 The Standard Model	2
1.2 Hadrons	5
1.3 Spin	7
1.4 Isospin	8
1.5 Cross Section	11
1.6 Polarisation Analysis	14
1.6.1 Photon Polarisation	14
1.6.2 Neutron Polarisation	16
1.6.3 Polarisation Observables	17
2 Motivation	19
2.1 Deuteron Photo-disintegration	20
2.1.1 Probing Higher Energies	22
2.2 Dibaryons and Hexaquarks	23
2.2.1 $d^*(2380)$	24
	iii

Table of contents

2.2.2	Dibaryon Multiplets	25
2.3	Short Range Correlations	26
3	Past Measurements	27
3.1	Historic Experimental Status	27
3.1.1	Regarding Energy Ranges	28
3.2	MAMI Analysis (2023)	29
4	Experimental Facility - Jefferson Lab	33
4.1	CEBAF	34
4.1.1	The Injector	35
4.1.2	Linear Accelerators	35
4.1.3	Recirculation Arcs	37
4.1.4	Beam Delivery	38
4.2	Hall B	38
4.2.1	The Bremsstrahlung Tagging Facility	39
4.3	CLAS	44
4.3.1	The Start Counter (SC)	45
4.3.2	Torus Magnet	47
4.3.3	Drift Chambers (DC)	48
4.3.4	Cherenkov counters (CC)	50
4.3.5	Time-of-Flight Counters (TOF)	52
4.3.6	Electromagnetic Calorimeters (EC and LAC)	53
4.3.7	Triggers and Data Acquisition (DAQ)	54
4.4	The E-06-103 experiment (g13)	55
4.4.1	The Cryo-target	56
4.4.2	Data Corrections	56
5	Analysis	59
5.1	The Reaction of Interest	60
5.1.1	Angle Definitions	60
5.2	Event Selection	62

5.2.1	Preliminary Skim	62
5.2.2	Defining p_1 and p_2 Using DOCA	62
5.2.3	$\Delta\beta$ Selection	67
5.2.4	Photon Coincidence Time	68
5.2.5	POCA Z-vertex Selection	69
5.2.6	Diametric SC Paddle Restriction	70
5.2.7	Missing Pion Mass Cut	71
5.2.8	Final 2D missing mass selection	72
5.2.9	Data reduction summary	75
5.3	$C_{\mathcal{X}}$ extraction	77
5.3.1	Analysing Power A_y	78
5.3.2	Maximum Likelihood Introduction	80
5.3.3	Minimum Log-likelihood Formula	80
5.3.4	Parameterisation	81
5.3.5	Minimisation	82
5.3.6	Background $C_{\mathcal{X}}$ Measurement	84
5.3.7	Sideband Subtraction	85
5.3.8	Systematic Uncertainty of P_y	85
5.3.9	Capturing Statistical Uncertainty (Bootstrap technique)	87
5.3.10	Statistical Error Propagation	90
5.3.11	Assuming Background $C_{\mathcal{X}} = 0$	90
5.3.12	Binned Asymmetries Method	92
6	Results	95
7	Future Work	99
7.1	Including g13b	99
7.2	Systematic Studies	100
7.2.1	Data Selection	100
7.2.2	Method of $C_{\mathcal{X}}$ Extraction	100
7.2.3	$C_{\mathcal{X}}$ Parameterisation	101
7.2.4	Signal Ratio Variation	101

Table of contents

7.2.5	$C_{x'BG}$ Variation	101
7.3	Measuring P_y	102
7.4	Extending to CLAS12 and the SVT	102
7.4.1	Other Detector Systems	104
Bibliography		105
Appendix A Establishing the electron efficiency of CLAS12's Forward Tagger		111
A.1	Experimental Setup	112
A.2	Analysis	113
A.3	Formula to remove background contributions	115
A.4	Establishing R	118
A.5	Establishing Eff_{BG}	119
A.6	Considering Electron Theta	121
A.7	Results	122
Appendix B Relativistic Kinematics		125
Appendix C Supplementary Formulae		131
C.1	DOCA formula	131
C.2	$C_{x'}$ sideband subtraction	133
C.2.1	Deriving $\delta C_{x'}$	133
C.2.2	Origins of Variable Errors	134

List of figures

1.1	The standard model of fundamental particles	2
1.2	Particle families	5
1.3	Baryon $J = \frac{1}{2}, \frac{3}{2}$ Multiplets	9
1.4	Scattering angle diagram	12
1.5	Solid angle diagram	12
1.6	Photon polarisation diagrams	15
2.1	Deuteron photo-disintegration	20
2.2	Previous $d(\gamma, p)n$ cross section measurements and models	22
2.3	Hexaquark diagram	24
2.4	The deuteron antidecuplet	25
2.5	The $d^*(2380)$ antidecuplet	25
2.6	The EMC effect	26
3.1	JLab P_y^p and C_x^p measurements and predictions for $\theta_{sc} = 90^\circ$	29
3.2	Surface of C_x^p values and errors by M. Bashkanov <i>et al.</i>	31
3.3	Fixed angle values of C_x^p by M. Bashkanov <i>et al.</i>	32
4.1	JLab aerial photograph	33
4.2	CEBAF overview	34
4.3	The CEBAF Injector	35
4.4	CEBAF niobium cavity photograph	36
4.5	CEBAF linac cryo-unit diagram	36
4.6	CEBAF recirculation arcs photo	37

List of figures

4.7	Hall B side-view	38
4.8	Overview of photon tagging system	40
4.9	Hodoscope counters diagram	41
4.10	T-counter timing resolution	42
4.11	Coherent bremsstrahlung peaks seen in linear polarisation	43
4.12	Photo of CLAS	44
4.13	CLAS schematic diagram	44
4.14	Start Counter render	45
4.15	Start Counter cross section	46
4.16	Start Counter paddle cross section	47
4.17	CLAS torus magnetic field contours	47
4.18	Drift Chamber layout	48
4.19	Drift Chamber photograph	48
4.20	Drift Chamber detection representation	50
4.21	Cherenkov counter module	51
4.22	Cherenkov counter sector	51
4.23	Time of Flight sector	52
4.24	Electromagnetic calorimeter module	53
4.25	Calorimeter reconstruction	53
4.26	Large-angle calorimeter	54
4.27	g13 cryo-target render	56
5.1	The reaction of interest	60
5.2	DOCA comparison diagram	63
5.3	DOCA distribution histogram	64
5.4	Δ DOCA histogram	65
5.5	p_1 vs p_2 $MM^2(\gamma d \rightarrow pX)$ comparison	67
5.6	Visualisation of $\Delta\beta$ cuts	68
5.7	Coincidence time for all photons	69
5.8	Coincidence time cut	69
5.9	POCA-z vertex cut	70
5.10	SC paddle separation between protons	71

5.11 $MM^2(\gamma d \rightarrow p_1 p_2 X)$ histogram	72
5.12 2D missing mass region of interest	72
5.13 Final missing mass selection	73
5.14 Fitting data between each cut	76
5.15 SAID model of analysing power	79
5.16 Data distribution between $\pm A_y$ values	79
5.17 Data distribution among E_γ vs θ_N	81
5.18 Raw $C_{X'}$ extraction	83
5.19 Raw $C_{X'}$ extraction ($\theta_N = 90^\circ$)	83
5.20 Background $C_{X'}$ extraction	84
5.21 Background $C_{X'}$ vs E_γ at θ_N extraction	84
5.22 Sideband subtraction visualised	85
5.23 P_y systematic uncertainty	86
5.24 Overlapped bootstrap functions	87
5.25 Unfiltered bootstrap functions	88
5.26 Area under bootstrap functions	88
5.27 Fitting bootstrap projections	89
5.28 Raw $C_{X'}$ presented as area plot	89
5.29 All $C_{X'}$ area plots	91
5.30 Effect of setting $C_{X',BG} = 0$	92
5.31 Asymmetry histograms	93
6.1 Final $C_{X'}$ result	95
6.2 Final $C_{X'}$ result, $\theta_N = 90^\circ, 60^\circ$	96
7.1 SVT module composition	103
A.1 CLAS12 diagram	111
A.2 Forward Tagger design	111
A.3 FT-cal arrangement	112
A.4 Single FT-cal crystal	112
A.5 Forward Tagger acceptance	114
A.6 Electron XY position comparison	115

List of figures

A.7	Missing electron mass and region selections	116
A.8	Sampling background efficiency outside the $MM^2(p\pi^+\pi^-)$ peak	120
A.9	Sampling background efficiency outside the $MM^2(p\pi^+\pi^-)$ peak in simulated data	120
A.10	Steps to calculate efficiency	121
A.11	Calculated efficiency results	122

List of tables

1.1	Quark quantum numbers	3
1.2	The fundamental forces	4
1.3	Example hadrons	6
2.1	Polarisation observable definitions	21
3.1	Past measurements of P_y^n	28
5.1	Data reduction overview	76

Acknowledgements

This thesis is the result of many people's support, to whom I offer my sincere gratitude. First and foremost, my resilient and righteous father, Andrew Booth, whose daily phone calls have been a constant source of motivation and reassurance through all my major life transitions. He will occasionally remark how far I've come, which I may fail to fully appreciate, but I at least know that without his voice of wisdom, I wouldn't have made it very far at all.

Next, I extend heartfelt thanks to the relentlessly charitable Nicola and Richard Woosnam, whose generous financial aid and assistance with relocation made the PhD possible. I will be forever thankful that Nicola spontaneously entered my life in November 2018.

I'm proud to have been part of the small hadron group at the University of York, whose friendly, collaborative spirit made my research experience welcoming and stress-free. I wish all of them well, wherever they may go in the future. In particular, I'd like to credit Dr. Stuart Fegan for his constant help and patience through tedious bug-fixing, navigating admin, and all-round emotional support. Stuart is brilliant for checking up on every student in his coffee-fuelled rounds of the offices. He's a pillar of our group and has always been fighting my corner.

I must of course thank our group's amazingly knowledgeable supervisors for initially taking a chance on an awkward pot-washer from Scarborough to take on their cutting-edge project. The fact that I started this PhD with no previous hadron-specific education is a testament to their ability to teach and foster students. Dr. Nicholas Zachariou in particular met with me countless times, office or online, to advise me or make light of my list of scribbled questions and concerns. Whenever I feel stuck, he is consistently able to put me back on track with a renewed sense of direction.

Despite the disruptions of 2020-21 having it off to a slow start, this PhD has been a life-changing experience. Five years ago, I could not have envisioned myself travelling around the world, or presenting my work to whole lecture theatres. This has been a very rewarding end to my days of being a student, and any subsequent career will be owed to those that got me here.

Declaration

I declare that this thesis is a presentation of original work and I am the sole author. This work has not previously been presented for a degree or other qualification at this University or elsewhere. All sources are acknowledged as references.

Chapter 1

Introduction

Understanding what our observable world is fundamentally made of is a seemingly basic pursuit that has nonetheless grown at an accelerative pace, over millennia, into multiple deep and complex scientific fields. Today, particle physics has spawned internationally collaborating laboratories and facilities such as CERN, Fermilab, and Jefferson Lab, all with the shared goal of understanding the sub-atomic world and the nature of matter.

As a PhD student, my first major contribution to this global effort is presented within this thesis, in which I detail my analysis of a substantive sample of Jefferson Lab's particle scattering experimental data, and ultimately provide a measurement of recoil neutron polarisation in the reaction of deuteron photo-disintegration, contributing to a lacking world data-set of associated observables. More importantly, this analysis serves as a demonstration of a novel approach to measuring neutron polarisation that bypasses the need for dedicated polarimetry equipment. It is hoped that this technique paves the way for neutron polarisation to be measured in a plethora of other experiments and reaction channels at Jefferson Lab, allowing for many high-impact analyses in the future.

Before delving into the specifics of my work and research, this introductory chapter will be focused on covering the background knowledge required to understand the analysis and results presented within this thesis; both my own work, and the results of previous measurements.

1.1 The Standard Model

The standard model of particle physics defines elementary, fundamental particles (quarks and leptons) which individually contribute to the known matter of the universe, each being replicated on an astronomical scale. It also defines fundamental force-carrying particles (bosons) which individually contribute to the fundamental forces. The model names and groups these particles into families and generations as shown in Fig. 1.1.

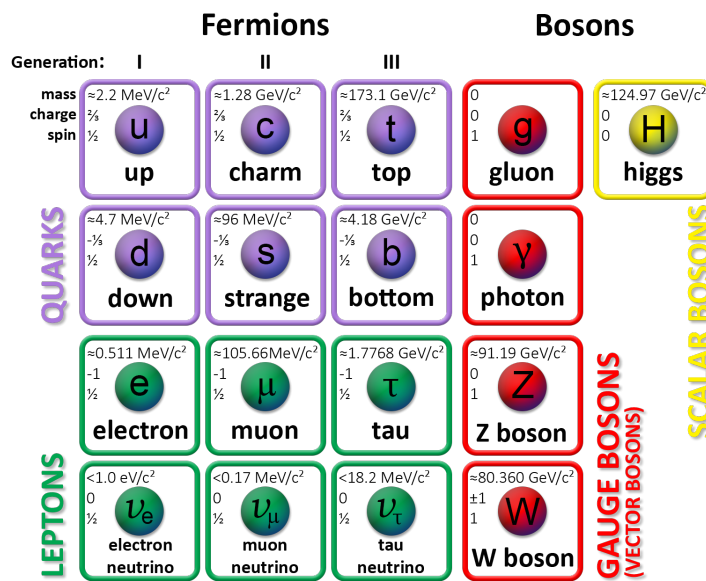


Fig. 1.1 The standard model of fundamental particles, showcasing the currently known fundamental contributors to matter and the fundamental forces; strong, weak and electromagnetic.

Each elementary particle has an indivisible and discrete (quantised) value of electromagnetic charge, q , and spin, s (to be discussed later), as well as having an equivalent anti-particle, which possesses equivalent mass yet opposite quantum values [2]. In particle physics, charge is given in units of e , elementary charge, equal to the magnitude of charge carried by an electron (1.602×10^{-23} Coulombs). Anti-particles are usually denoted by a bar over their respective symbol (e.g. \bar{p}), except in cases such as the positron (the anti-electron) which is most commonly denoted by e^+ . Rest mass, m , is given in units of eV/c^2 , useful for relativistic kinematics (see Appendix B for a brief overview). As seen in the model (Fig. 1.1), all fundamental particles are either fermions or bosons. Fermions come in "generations", with higher generation fermions having more mass, and being energetically unfavourable, making them unstable and hence are less common in nature. For example, the electron

(e^-) has a mass of $0.511 \text{ MeV}/c^2$, and does not naturally decay. The next generation's equivalent particle, the muon (μ^-), is essentially a heavier electron, having a mass ~ 200 times larger, and an average lifetime of $2.2 \mu\text{s}$ before decaying into an electron [3]. Sequentially, the tauon (τ^-) has a mass ~ 17 times the mass of μ^- , and an average lifetime around 7.6 million times shorter. This alludes to some of the challenges particle physicists face when hunting for exotic matter.

The quarks come in 6 types, referred to as flavours, and contribute their properties to larger particles (hadrons) that they constitute (to be explained more in the next section). To help keep track of these properties, there are many quantum numbers associated with quarks, shown in table 1.1.

Table 1.1 Quark quantum numbers

quark flavour	up (u)	down (d)	charm (c)	strange (s)	top (t)	bottom (b)
charge (Q)	$+\frac{2}{3}$	$-\frac{1}{3}$	$+\frac{2}{3}$	$-\frac{1}{3}$	$+\frac{2}{3}$	$-\frac{1}{3}$
Isospin (I)	$\frac{1}{2}$	$\frac{1}{2}$	0	0	0	0
Third component of Isospin (I_3)	$\frac{1}{2}$	$-\frac{1}{2}$	0	0	0	0
Charm (C)	0	0	1	0	0	0
Strangeness (S)	0	0	0	-1	0	0
Topness (T)	0	0	0	0	1	0
Bottomness (B')	0	0	0	0	0	-1
Baryon number (B)	$\frac{1}{3}$	$\frac{1}{3}$	$\frac{1}{3}$	$\frac{1}{3}$	$\frac{1}{3}$	$\frac{1}{3}$
Hypercharge (Y)	$\frac{1}{3}$	$\frac{1}{3}$	$-\frac{2}{3}$	$\frac{1}{3}$	$\frac{1}{3}$	$\frac{1}{3}$

Many quantum numbers first came about because it was observed that particle interactions seemed to have rules, only permitting certain decays/exchanges, as if hidden properties were being conserved. Many of the names first given to these observed *strange* properties have stuck, giving us the names we have today. "Top" and "bottom" are sometimes referred to as "truth" and "beauty" respectively, and some say that "strange" should instead be named "sideways", to maintain the directional theme. Regardless, with the now established standard model, we can understand that, for example, the flavour quantum numbers (strangeness, topness, etc.), are contributed by their respective quarks, and are conserved through interactions mediated by the "strong" force. By convention, the sign of flavour quantum numbers is chosen to be the same as its electric charge [4]. For instance, the negatively charged strange quark has a strangeness of -1.

Baryons are particles made of three quarks. Before the understanding of quarks and the creation of the standard model, baryon conservation was an observed law of the universe, and so quarks inherit this conservation law by being given a baryon number (B) of $\frac{1}{3}$ (there is similarly a lepton number, L , owing to leptons being always conserved in the standard model). The majority of observable matter

is fundamentally made of up and down quarks, but contributions from higher generation quarks are possible. For example, a baryon that contains a contribution from a strange quark (but no quarks of heavier flavour) is known as a hyperon, and there is great interest in how these particles interact with conventional matter. Hypercharge, Y , is another conserved quantum number that builds upon previous, considering in addition these higher generational quarks. An unfortunate consequence of there being so many quantum numbers, particles, and variables in this field, is that sometimes the same symbol can be used for different meanings, such as strangeness and total spin (S), or charge and the general symbol for quark (q). For this reason, the symbol for bottomness, B' is often denoted with a prime symbol, to distinguish it from Baryon number, B .

So far, we have mainly discussed fermions. Fermions follow Fermi-Dirac statistics, meaning they cannot overlap, similar to our familiar world of macroscopic objects - two tennis balls cannot occupy the same space. On the quantum scale, this means that no two fermions may occupy the same quantum state in a quantum system. This is known as the Pauli exclusion principle. Bosons, on the other hand are not constrained by this rule, instead following Bosé-Einstein statistics. This means that multiple bosons can occupy the same space. Bosons are responsible for the fundamental forces, an overview of which is given in Table 1.2. In the standard model, each of the fundamental forces with the exception of gravity has a corresponding gauge boson that mediates it.

Table 1.2 The fundamental forces

Force	Relative Strength	Theory	Mediator
Strong	10	Chromodynamics	Gluon
Electromagnetic	10^{-2}	Electrodynamics	Photon
Weak	10^{-13}	Flavordynamics	W/Z boson
Gravitational	10^{-42}	Geometrodynamics	Graviton (hypothesised)

Table taken from [2]. The author notes that relative strength is ambiguous, as it depends on the source and distance, therefore these numbers should not be taken literally.

To summarise, the standard model represents our current best understanding of the universe, being very successful in its predictions and explanations of particle/hadron physics. However, while proving to be a robust and useful model, it is not a complete theory. It does not explain phenomena such as the universal matter to anti-matter imbalance, the apparent presence of "dark" matter in the universe, nor does it incorporate the full theory of gravity, only having force carrier particles for three of the four fundamental forces; strong, weak and electromagnetic.

1.2 Hadrons

As mentioned in the previous section, all fundamental particles fall under two categories, bosons (integer spin particles) and fermions (half-integer spin particles). A hadron is defined as being a composite particle, consisting of two or more quarks (a bound state). Spin (s) will be explained more clearly in the next section, however, note that quarks are particles of $s = \frac{1}{2}$, which can sum together to make hadrons of both integer and half-integer spins. Therefore hadrons can be either fermions or bosons. Figure 1.2 shows how these family groups overlap.

Baryons are particles comprised of three quarks (qqq), making them fermions. Mesons are particles consisting of one quark and one antiquark ($q\bar{q}$), making them bosons. Rarely, hadrons go beyond this convention (exotic hadrons). The hunt for exotic hadrons is a motivator for many modern analyses, including this project, as will be discussed in more detail later.

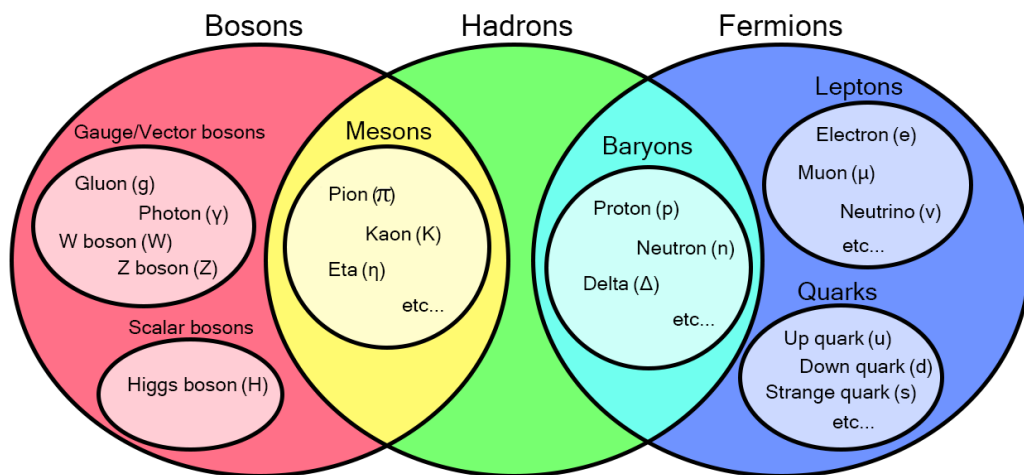


Fig. 1.2 A Venn-diagram to visualise how particle families are grouped.

The hypothesis of quark confinement tells us that unlike leptons, quarks are never free particles, only seen together forming hadrons [5], bound by the strong force. The theory of quantum chromodynamics (QCD), tells us that the strong force is mediated by gluons and involves "colour" exchanges, in which quarks rapidly swap between 3 states that particle physicists refer to as red, green and blue. It is observed that all particles exist as *colour neutral* - possessing a combination of quarks (and/or anti-quarks) that sum to balance each of these 3 colour states. For example, the 3-quark baryon must have one of each red, green and blue. A 2-quark meson may exist as red and anti-red, green and anti-green, or blue and anti-blue. QCD shows that two or more quarks of the same flavour (up, down,

strange, etc) are allowed to exist together in a hadron without violating the Pauli exclusion principle by possessing different colour "charges".

Any given hadron is defined by the flavour of the quarks that constitute it. The well known proton, for example, has the quark structure of uud , which together sum to make an electric charge of 1. A few more examples are shown in Table 1.3 below.

Table 1.3 Examples of some hadrons and their composition. Data taken from [3].

Family	Name	Symbol	Quarks	Charge (Q)	Mass [MeV]
Baryons	Proton	p	uud	+1	938
	Neutron	n	udd	0	940
	Lambda	Λ	uds	0	1116
	Anti-Proton	\bar{p}	$\bar{u}\bar{u}\bar{d}$	-1	938
	Omega	Ω^-	sss	-1	1672
Mesons	Pion(+)	π^+	$u\bar{d}$	+1	140
	Pion(-)	π^-	$\bar{u}d$	-1	140
	Kaon(+)	K^+	$u\bar{s}$	+1	494
	Eta	η	$u\bar{u} / d\bar{d} / s\bar{s}$	0	548

The above list is by no means extensive, but it demonstrates how a particle's charge is a result of its quark content. With the inclusion of both proton and anti-proton (as well both π^+ and π^-), it is also shown how the quark composition of hadrons is mirrored in the equivalent anti-particle. Some hadrons, such as η , are their own anti-particle, as inverting the component quarks would yield an identical arrangement. The η is also an example of a hadron in which the quark content exists as a superposition of multiple possible states, as particles exist more like wave-functions rather than the traditional imagining of billiard balls.

When particle interactions take place, there can be an exchange of these building block quarks, where reactants can rearrange to form products, much like a balanced chemical equation. In hadronic physics, scientists closely study these reactions and exchanges, identifying them through spectroscopic particle experiments. It is through these experiments that theoretically predicted hadrons can be experimentally proven, and reactions/mechanisms can be well-defined with robust statistics, improving existing models and understanding.

1.3 Spin

In nuclear and particle physics, "spin" is the name given to the fundamental property of particles that gives rise to their intrinsic angular momentum (separate from their orbital angular momentum). The name originates from how it was first imagined when hypothesised in 1925 [6], as a spherical particle literally spinning on an axis. However, quantum spin has no classical counterpart, as there is no physical motion involved, and the spinning top model is used only as an analogy [7]. In fact, from the perspective of classical physics, the hypothetical surface of a particle would have to move faster than the speed of light (an impossibility) in order to produce the observed values of angular momentum. Spin is simply a fundamental property like mass or charge. Together with the orbital angular momentum, l , spin contributes to the total angular momentum of a particle, j . These variables are capitalised when denoting the vector sum of a composite system (e.g. a hadron), and given by $J = L + S$.

Being a quantum property, associated values of spin are restricted to being multiples of a fundamental unit, rather than free to assume any arbitrary value. This fundamental unit is denoted by \hbar , the reduced Planck's constant [8]. Additionally, due to spin being a quantum *vector*, there is also restriction in allowed directions that spin may be orientated, with each possible direction often referred to as a state, or a projection (in the Z-axis). For a given particle with spin, s , allowed projections are restricted to being $m_s \hbar$, where m_s is a quantum number that can be $\pm s$ as well as any possible value at integer steps between (e.g. when $s = \frac{3}{2}$, $m_s = -\frac{3}{2}, -\frac{1}{2}, \frac{1}{2}, \frac{3}{2}$). Ultimately, this means that particles with spin can have multiple spin states. The electron, for example, a spin $\frac{1}{2}$ particle, has possible spin states $+\frac{1}{2}$ and $-\frac{1}{2}$, often referred to as spin-up and spin-down. This allows them to pair together (occupying the same atomic orbital) in anti-parallel ($\uparrow\downarrow$) without violating the Pauli exclusion principle. Angular momentum, l , is also similarly restricted to integer multiples of \hbar , and able to project at integer steps between $\pm l$. However, unlike spin, angular momentum is not fixed for each particle, and can be increased by the addition of energy to the system, which, through vector addition, can affect the ultimate value of j .

Spin plays a large role in experimental hadron physics due to it being a conserved property, being transferred or induced through particle interactions. As such, the spin of an unknown product particle can be inferred if the spin of all other particles in a reaction are known or measured. Additionally, because all modelled hadrons have an established/theoretical value of spin, this can assist in

identification of the unknown particle. Being able to measure spin through the macroscopic effect of polarisation is therefore a powerful analysis technique in hadron physics, and is conventionally achieved through dedicated equipment such as a polarimeter. However, as will be shown in this thesis, polarisation can also be measured by analysing the scattering angles of product particles of a well-understood reaction in which transferred/induced polarisation is known to correlate with product particle angular distribution.

1.4 Isospin

Long before the discovery of quarks, it was observed that the proton (p) and neutron (n) are much alike. They have near identical mass, and the strong force acts identically for pp , nn , and pn combinations (coupling). It was proposed by Heisenberg in 1932 that they may each be different states (or projections) of the same particle, the nucleon [9], sharing the same value of a conserved vector property, isospin (I), originally short for isotopic spin [10], but now preferred to mean isobaric spin.

Much like spin, isospin was proposed as a vector quantum number that gives rise to discrete states by virtue of its orientation. We use the Z-component, more commonly referred to as the third component of isospin, I_3 , to tell us where these discrete states lie, which, like projections of spin (m_s), varies in increments of 1. To put this into practise: as it was observed that the nucleon has two states, proton and neutron, their common isospin, I , must be $\frac{1}{2}$, allowing for the third component, I_3 , to project as $\pm\frac{1}{2}$, giving two possible states. The proton and neutron correspond to a I_3 of $+\frac{1}{2}$ and $-\frac{1}{2}$ respectively.

Isospin helped early hadron physicists collect like-particles into common groups that viewed them as projections of the same particle. Pions (π), for example, seem to exist as triplets of $Q = -1, 0$ and 1 . The Kaons (K) appear as isobaric pairs, possessing a then-unknown conserved vector property, strangeness. With the discovery of this new property, it was found that hadrons can be arranged into multiplets, with the first proposal of this being named "the eightfold way" in 1961 [10] (a nod to the "Eightfold Path" of Buddhism), arranging the 8 then-known baryons into the baryon octet, and similarly with a meson octet, by virtue of their charge, Q , strangeness, S , and third component of isospin, I_3 . This baryon octet is shown in Fig. 1.3, as well as the baryon decuplet - to be explained shortly. These multiplets, which consider only the first 3 quark flavours (up, down and strange), are

sometimes referred to as SU(3), (special unitary group in 3 dimensions), as they are derived from mathematical matrix group theory [11]. For example, to consider in addition, charm quarks, would require SU(4), for which associated multiplets become 3-dimensional.

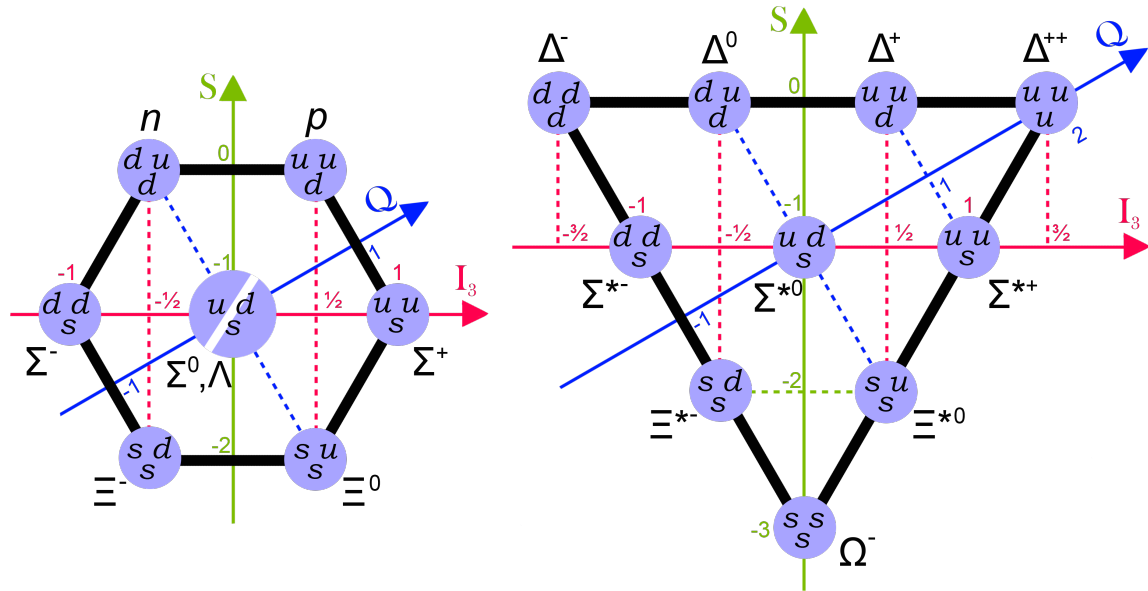


Fig. 1.3 Diagrams showing how hadrons of common spin (J) can be grouped into SU(3) multiplets that arrange them according to their quark content, which dictates their charge, Q , strangeness, S , and third component of isospin, I_3 . **Left:** The $J = \frac{1}{2}$ baryon octet. **Right:** The $J = \frac{3}{2}$ baryon decuplet.

With our modern understanding of quarks, we can see why the proton (uud) and neutron (udd) are so similar, differing only by a single quark. We can therefore say that the up quark contributes $+\frac{1}{2}$ and the down quark contributes $-\frac{1}{2}$ to the overall value of I_3 . As discussed previously, we also now understand the origin of strangeness, being another quark flavour like up or down. Therefore, because quark flavours are conserved within the strong force (referred to a flavour symmetry), isospin symmetry (conservation) is simply the larger effect of flavour symmetry.

In the centre of the baryon octet are two overlapping particles, Σ^0 and Λ . Despite having the same quark composition, these are fundamentally different particles, having different masses ($\Lambda:1116\text{ MeV}/c^2$, $\Sigma^0:1197\text{ MeV}/c^2$) and decay modes [3]. The difference is in their isospin. The Σ s have $I = 1$, and therefore can project in 3 possible I_3 states, whereas the Λ has $I = 0$, meaning only a single projection. Fundamentally, this behaviour is caused by a difference in the particle wavefunctions, as described by QCD, however this is beyond the scope of this thesis. Even though

the origin of isospin is mathematically understood in QCD, it remains useful to explain things more generally in terms of isospin.

All baryons in the ground-state baryon octet have a total angular momentum of $J = \frac{1}{2}$. This is because each has their spin- $\frac{1}{2}$ quarks orientated to be two in parallel and one anti-parallel (eg. $\uparrow\uparrow\downarrow$). It's possible to form other hadron multiplets of a different common J value, for example the baryon $J = \frac{3}{2}$ decuplet, containing 10 baryons with their quarks all in parallel ($\uparrow\uparrow\uparrow$). As seen in Fig. 1.3, hadrons of the same quark composition appear in both the baryon octet and the baryon decuplet, for example, the neutron (n) and delta 0 (Δ^0) (both udd). Again, these are fundamentally different particles. The Δ s can be thought of as the excited states of the nucleons, due to a requirement of energy to turn one into the less stable other (and subsequently decays back), through the increase of total spin, S , and hence total angular momentum, J . This extra freedom gives the Δ an increased isospin of $\frac{3}{2}$, allowing the I_3 to project in 4 different orientations, corresponding to the 4 possible configurations of the Δ particle.

As discussed in the previous section on spin, the J of a particle can also be changed by virtue of its orbital angular momentum, L . Because of this, it's possible to have even higher energy configurations of particles (excited states). One definition of "ground-state particle" is that it has $L = 0$. In this definition, the $J = \frac{3}{2}$ Δ s are still ground-state particles, despite them being considered excited nucleons in a strictly isospin sense. Excited state particles are commonly discovered as "resonances", a certain energy at which they tend to form in scattering reactions. Resonances are often written as their ground-state symbol alongside their resonance energy/mass (in MeV). For example, the $N(1440)$ (or $P_{11}(1440)$) is a nucleon resonance discovered in 1964 [12], having a mass of $1440 \text{ MeV}/c^2$. Resonances can therefore be thought of as their own unique particles, each having a characteristic mass, average lifetime, and decay modes.

1.5 Cross Section

In the every day world, "cross section" implies a 2D slice of some volume or 3D setup. In particle physics, this term is instead used to denote the probability of interaction [13]. This is yet another case of an early-conceptualised term sticking, with the original proposed meaning now only useful as analogy. In this sense, cross section (σ) can be thought of as the effective area that one particle presents to another during interaction [2, 4]. There can be a specific cross section associated with any interaction (e.g. a neutron-nucleus absorption cross section).

An intuitive analogy often used is that of an arrow aimed at a target [2, 13], where the larger the cross-sectional area of the target, the more likely the arrow (or stream of arrows) will hit. With this we can understand how "cross section", as it's conventionally understood as an area, therefore has correlation with the likelihood that interaction will take place. In the world of particle physics, matter is mostly empty space, and so the effective area of "targets" is extremely small, and as such, cross section is often given in units of barns, b, where $1 \text{ b} = 10^{-28} \text{ m}^2$. The term "barn" has its origin associated with the Manhattan Project, and nuclear bomb research, during which physicists preferred a more secretive word for the cross section of a uranium nucleus, which they discussed as being "as big as a barn" in the context of nuclear physics [14].

The "hit or miss" analogy of arrows and targets is an oversimplification, as particles are not solid spheres as first imagined in the days of Rutherford. What we find in reality is that particles have "soft" edges due to their quantum nature, acting like clouds of probability, where the proximity of particles (among other things) determines the chance or strength of the interaction.

Consider a Rutherford scattering scenario, where a stream of protons is fired at a hydrogen target (in essence, a proton target). We can expect the like-charges to repel, and the path of the incident proton to be deflected. As seen in Fig. 1.4, a particle with impact parameter, b , is deflected by a scattering angle, θ . The impact parameter tells us the distance that the incident particle would have missed the point-like target had it not been scattered. A rotational symmetry is assumed, and so the azimuthal angle, ϕ , is neglected.

Next, consider this same scenario, but with the impact parameter of the incident proton further increased by Δb . Because the particle is now further away from the influence of the target, its scattering angle is reduced by $\Delta\theta$. Hence, a change in b coincides with a change in θ . Consider the two previous trajectories simultaneously, and we can observe a spread between the two exiting

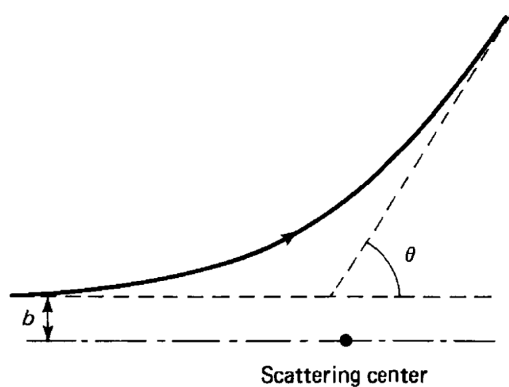


Fig. 1.4 Diagram taken from [2], showing the trajectory of a scattered particle passing by a fixed potential. θ is the scattering angle, and b , named the impact parameter, is the perpendicular offset.

scattering angles. If we take some radius, R , from the scattering centre, a solid angle, Ω , has been created between these two exiting trajectories. Ω can be thought of as the "field of view" from the target, projecting out to a radius between two angles. Here, the exact radius used does not matter; the scattering centre is point-like and b is very small, and so exiting particle trajectories can be considered to be diverging radially out from the target, such that Ω does not change with increased distance. In this simple example, it is shown how the "soft" area of influence of the target (which is quantified by cross section, σ) has produced an angular spread of scattering angles, and hence a solid angle, Ω .

More generally, and now including ϕ , a plane region created by infinitesimal variation of b and ϕ , corresponds to an infinitesimal area of cross section, $d\sigma$, where $d\sigma = b db d\phi$ (shown below in Fig. 1.5). The range of possible paths that intersect this area creates a spread of scattering angles and hence produces an infinitesimal solid angle $d\Omega$ between the extremes, as given by $d\Omega = \sin \theta d\theta d\phi$. Taking the ratio between these two defines the differential cross section, $\frac{d\sigma}{d\Omega}$.

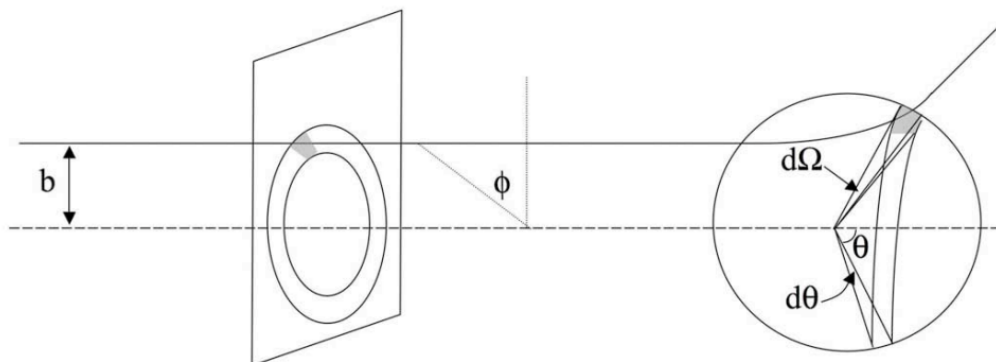


Fig. 1.5 Diagram taken from [4], showing how the solid angle, $d\Omega$, is created by possible parallel trajectories that intersect the shaded area in the tangential plane, as defined by varying b and ϕ .

If we consider a beam of incident particles with some luminosity, L , there is a flux of particles intersecting the previously defined cross section, $d\sigma$, per unit time, the number of which can be defined by $dN = Ld\sigma$. This can be rearranged to define differential cross section in the following way:

$$\frac{d\sigma}{d\Omega} = \frac{1}{L} \frac{dN}{d\Omega} \quad (1.1)$$

Integrating this over all angles yields the total cross section for a given interaction. This shows that cross section is a ratio between the total number of scattered particles and the total number of incident particles, making it analogous to the probability of the interaction taking place. As previously mentioned, there can be a specific cross section associated with any interaction. For example, a measurement of proton-proton to top-antitop cross section is simply counting how many top-antitop pairs were created when a given number of protons were fired at each other [13].

Another peculiarity of particle cross section that separates it from our macroscopic understanding of arrows and targets is the fact that it can vary with many other parameters, such as velocity, v (often preferred to be given as an energy, E). Differential cross sections are therefore often taken with respect to other parameters, not just Ω . For example, $\frac{d\sigma}{dE}$ (or combined into a double differential cross section, such as $\frac{d\sigma^2}{d\Omega dE}$). This is counter-intuitive, as in classical physics we would not expect the speed of a projectile to cause a change in target size. In particle physics however, the general rule of thumb is that cross section decreases with particle velocity, due to the passing particle spending less time in the vicinity of the interactable target "cloud". This general rule is not followed, however, when the velocity of the particle corresponds to an energy close to that of a "resonance", a topic touched on in the previous section. It can be found that for some scattering reactions, at certain energies, the particles involved tend to interact, forming a short-lived, semi-bound state before breaking apart [2]. This would be visible in data as a peak in $\frac{d\sigma}{dE}$, and is typically how resonances or exotic particles are found experimentally.

Cross section is what is known as an *observable*, a theoretical (yet experimentally measurable) characteristic of a specific reaction, or reaction component. They are derived from considerations of reaction probabilities. Observables are useful parameters, as they are independent of the experimental set-up used, such as the specific beam intensity, or target density. It is dependent only on the physics of the specific interaction. This means associated measurements can be easily compared across laboratories globally. Experimentalists aim to measure experimental observables such as cross sections, while theoreticians attempt to model them, in a symbiotic relationship where each field

informs and advances the other. However, experimental measurements will always be limited by technology (e.g. detector resolution, efficiency, cost, etc.), which is why particle/hadron physics continues to grow and refine. The next section will discuss polarisation observables, which further divide reaction probabilities by considering possible spin states. This further constrains reactions and can help provide more sensitivity to particles of interest, such as resonances.

1.6 Polarisation Analysis

In atomic and subatomic physics, polarisation refers to the orientation or alignment of a specific vector property (spin, dipole, oscillation, etc.), which is often influenced by external forces or fields. For example, applying a magnetic field causes magnetic dipole particles to align their poles either with or against the field (more accurately, their spin vector precesses around the magnetic dipole). In this sense, polarisation can be thought of as the macroscopic effect of spin. However, in polarisation analysis, it's often preferred to discuss spin in terms of helicity, defined as the component of spin in the direction of a particle's velocity. This leads to positive helicity (spin vector aligned with motion), and negative helicity (spin vector anti-aligned with motion). As covered already in this chapter, spin plays a major role in hadron physics, giving a characteristic value to each hadron, and being conserved throughout reactions. In a polarisation analysis, we study and measure this effect.

Polarisation analysis usually involves an experiment with an initially polarised beam incident on a target sample, with the polarisation of scattered products measured [15]. The polarisation analysis presented in this thesis will feature a polarised photon beam, and will involve the indirect measurement of neutron polarisation. Therefore, before going into more detail, it is necessary to understand these two components of polarisation.

1.6.1 Photon Polarisation

A photon is a quantum of light, and can be thought of as a transverse wave, oscillating in an electromagnetic field which is perpendicular to the direction of the photon's motion. When two photons are colinear (moving and oscillating together in the same field), they create interference, resulting in a single wave function made from the sum of their individual electric field vectors.

Consider two colinear photons of the same frequency and amplitude with their respective electric fields, \vec{E}_x and \vec{E}_y , orthogonal to each other. As a result of interference, there are two types of polarisation that can occur. If both photons are in phase*, they create linear polarisation (Fig. 1.6a) resulting in a photon that oscillates in a diagonal plane. If they are $1/4$ out of phase†, they create circular polarisation (Fig. 1.6b), resulting in a photon with a rotating electric field as it travels.

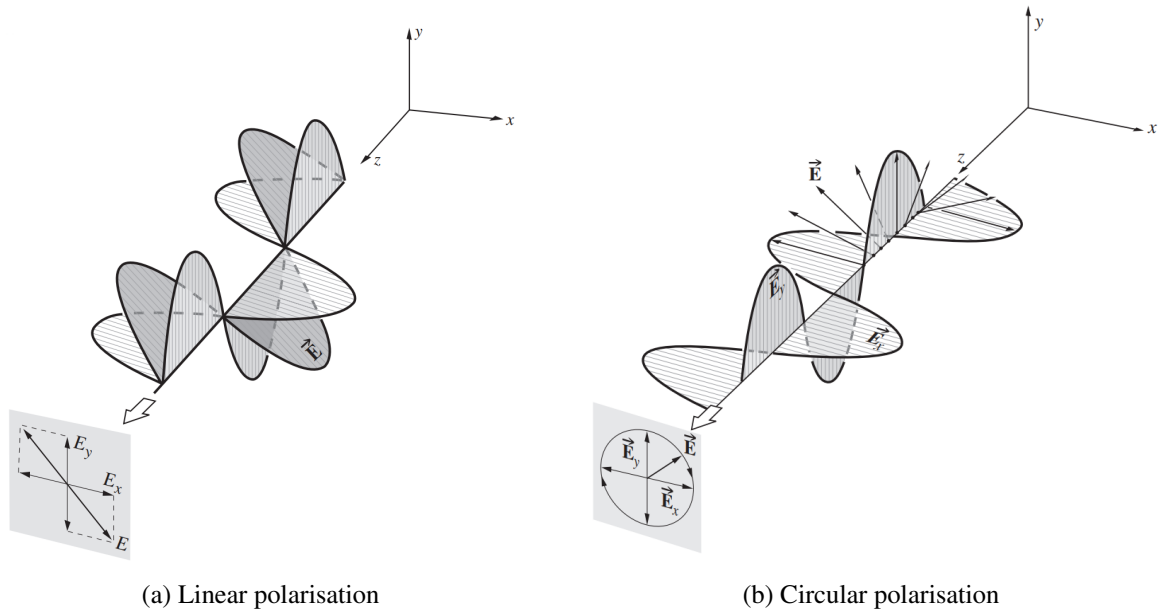


Fig. 1.6 Diagrams of the two types of polarisation that can occur between colinear, orthogonal and monochromatic photons, taken from [16]. The components of each photon's electric field (\vec{E}_y and \vec{E}_x) sum to create an overall vector \vec{E} . The orientation of \vec{E} over time depends on the phase between \vec{E}_y and \vec{E}_x .

In polarisation analysis, a polarised photon beam involves one of these two types of polarisations. Different polarisation observables can be accessed depending on which is used. A photon is a spin-1 boson, and the helicity of a photon is always +1 or -1. With a circularly polarised photon beam, helicity is +1 for right-hand polarisation (clockwise rotating field vector when facing in direction of motion) and -1 for left-hand polarisation. For linear polarisation, the helicity is not well defined, being a superposition of +1 and -1 helicities.

*For linear polarisation to occur, the peak of both waves (positive or negative) must occur at the same time, and so $1/2$ out of phase would also be linear polarisation, just in the other diagonal direction.

†Similarly, circular polarisation only requires the peaks of each wave to be perfectly anti-phase with each other, and so a phase difference of $3/4$ (or $-1/4$) would also meet this criteria, but result in a \vec{E} which rotates in the opposite direction (opposite helicity).

1.6.2 Neutron Polarisation

One might naively expect that the neutron, which has no charge, to therefore have no magnetic dipole. However, as proven experimentally in 1940 [17], it does in fact have a magnetic dipole, with a magnitude around 70% that of the proton [15]. This is a result of the component quarks, which have their own intrinsic spin and charge distribution. To measure neutron polarisation in a polarisation analysis experiment, dedicated equipment is typically required. Such a set up may require components such as [18]:

- Magnetic guide-fields, to maintain the direction of polarisation as neutrons are travelling.
- Spin-flippers, to reverse the polarisation and to detect whether the sample causes spin-flip scattering.
- Directional coils, to select specific orientations of polarisation for detection.

Large scale particle physics experiments typically use multi-purpose detectors (e.g. the "CLAS" detector at Jefferson Lab, to be discussed in a later chapter), which consist of tightly packed spectrometers and subsystems, and carefully calibrated magnetic fields. As such, there may not be sufficient space for such a dedicated polarimeter set-up. An additional complication is that neutral particles are less efficiently detected by detector systems due to their relative non-interactivity (no ionising-trail, and trajectory unchanged in a magnetic field). For example, the CLAS detector at Jefferson Lab, on which the work in this thesis is based on, had only a 10-20% neutral particle detection efficiency*. High statistics are therefore required to have any final-state neutron data at all.

Because of these complications, neutron polarisation tends to be a missing measurement in scattering experiments and associated data. Therefore, associated polarisation analyses tend to be neglected, with the focus more commonly being on unpolarised cross sections, or more accessible particles. This means there is a wealth of available data on polarised beam experiments featuring product neutrons, which is under-utilised in obtaining information on their polarisation. If polarisation information could be somehow extracted from such data, it would make possible an abundance of valuable, high-impact analyses. Herein lies one of the main motivations of this thesis; providing a method to measure neutron polarisation without a dedicated neutron polarimeter.

*Neutron detection efficiency depends on momentum. Typical neutron momentum in this analysis is 200-400 MeV/c. Based on CLAS data from [19], this gives a rough estimate of efficiency.

1.6.3 Polarisation Observables

For any given reaction in hadron physics, each component has a characteristic spin, and therefore each non-zero spin component can take on different helicities. Within conservation laws, there may be several possible helicity combinations for a particular reaction. Each combination can be expressed as an amplitude, representing its contribution to the full reaction. These amplitudes cannot be resolved individually due to complex components, and so we take bilinear combinations. This allows them to be expressed as probabilistic contributions to the full cross section of a reaction. The weight that each bilinear combination carries towards the full polarised cross section is parameterised, and known as a polarisation observable [20].

An unpolarised reaction component is a statistical mixture of all possible helicities. When a basic cross-sectional analysis is performed with no polarised components, what we are really seeing is the linear combination of all helicity amplitudes. However, if we use polarised components, we eliminate some amplitudes and begin to focus on specific observables, as will be demonstrated in Sec. 2.1. With well-chosen axes and high statistics, a robust polarisation analysis is possible, the goal of which is to extract measurements of the observables of interest. This process is essential for a full understanding of a reaction, including any resonances that may form within. While a peak in an unpolarised cross section may evidence a resonance, a polarisation analysis can identify its spin properties, as each amplitude represents a specific spin-parity, J^P . We typically expect that when a resonance manifests in a specific helicity amplitude combination, the real component disappears, and the imaginary component hits a maximum [21]. However, this may not be the case when there are other nearby resonances, or if the resonance also couples to other channels.

There are many different polarisation observables that can be measured for a given reaction. For example, beam asymmetry, Σ , an observable denoting how the orientation of a linearly polarised photon beam affects the cross section of a reaction, thus inducing an asymmetry in outgoing scattering angles (azimuthal dependence). Σ is what is known as a *single* polarisation observable, as it requires only one component of polarisation in order to be measured - in this case, the beam. Σ can then be measured by studying a differential cross section with respect to the azimuthal angle. There are also *double* polarisation observables, which require the simultaneous measurements of two polarisations, correlating them both. For example, polarisation transfer C_x (the focus of the analysis presented in

this thesis), requires measuring the polarisation of the photon beam and recoil particle, and indicates how much polarisation is transferred through the reaction.

Double polarisation observables tend to come in sets for each combination of reaction components they measure. Typically, beam-target (BT), beam-recoil (BR) and target-recoil (TR). To avoid complication, it is often preferred to focus on reactions with spin-0 particles, or otherwise simple kinematics. In this thesis, a polarisation analysis of deuteron photo-disintegration ($\gamma d \rightarrow np$) is performed using an unpolarised target, resulting in a manageable cross-section formula. The specifics of this reaction will be detailed in the next chapter.

Partial Wave Analysis

Partial wave analysis (PWA) is another method of analysing particle reactions. Whereas polarisation analysis decomposes a reaction into separate helicity combinations, assigning an amplitude to each, PWA decomposes a reaction into each component of angular momentum, l , (partial waves), which are each assigned as an amplitude. Therefore, in PWA, observables are combinations of partial waves. Just like with helicity amplitudes, these partial waves each contain real and imaginary components which are typically affected by resonances in the same way; with the real component suppressed, and the imaginary component peaking.

PWA models are fitted to cross-sectional data in order to extract their observables. A polarisation analysis is not necessary for this process, but simplifies it greatly, providing more constraints on the fitting procedure. This is an example of how robust polarisation analyses directly benefit the wider field, and lead to fully understanding reactions.

The focus of this thesis is by no means a partial wave analysis, however a PWA model for a well-understood reaction ($np \rightarrow pn$) will be utilised in the analytical method (Sec. 5.3.1). From this will be invoked an observable known as analysing power, A_γ , which denotes the degree to which incoming polarisation creates an asymmetry in the outgoing angular distribution of a recoil particle. Such a value therefore enables the incoming polarisation to be inferred through the analysis of this recoil angle.

Chapter 2

Motivation

With a foundational understanding of hadronic physics established by the preceding chapter, the following chapter will begin to focus on the work presented in this thesis, identifying the main motivations behind the project, with an overview of each. There are two primary motivators behind this project. One is a desire to understand exotic phenomena (mainly hexaquarks), that sit on the frontier of hadron physics. As such, this will involve more complex concepts that will require further explanation, building upon previous introductory material. The second motivation is a desire to have a more accessible method of measuring neutron polarisation at Jefferson Lab, with the main intention being that it would enable a polarisation analysis of the aforementioned phenomena. However, such an analytical method would no doubt benefit analyses beyond ones related to the subjects of interest to be detailed in this section.

2.1 Deuteron Photo-disintegration

The deuteron (d) is a particle comprised of a proton and neutron, bound by the strong force. It forms the nucleus of deuterium (D or ${}^2\text{H}$), a stable isotope of hydrogen. The deuteron is the only atomic nucleus with exactly two nucleons ($A = 2$) and as such presents the simplest case in which nuclear theories and models can be tested [22]. Cross section and decay formulae simplify greatly when there are only two particles detected in the final state (2-body formulae) [4], as is the case when deuteron disintegrates into its component proton and neutron, which can be caused by an addition of energy, such as via an incident photon. This is known as photo-disintegration.

Deuteron photo-disintegration ($\gamma d \rightarrow pn$), depicted in Fig. 2.1, was first investigated in the early 1930s to better understand the neutron [22], but continues to be utilised as an investigation of nuclear and hadron theory. For example, the Δ resonance/particle is visible as a peak in the differential cross section of deuteron photo-disintegration at around 300 MeV photon beam energy.

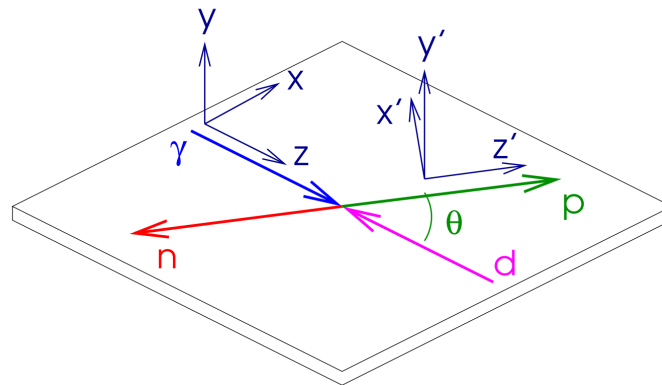


Fig. 2.1 Diagram of deuteron photo-disintegration in the centre-of-mass frame, and the co-ordinate system used. Taken from [22].

Deuteron photo-disintegration also represents the simplest case in which neutron polarisation can be measured. No free neutron targets exist, and so deuteron is the next best thing. Despite this reaction being so fundamental, there are significant gaps in the world dataset of associated polarisation analyses of product nucleons (especially for n) in terms of the energy range and angular coverage (past measurements to be detailed in Chap. 3). A more in-depth polarisation analysis of deuteron photo-disintegration that covers these unstudied kinematic regimes is essential for us to fully understand the nucleon-nucleon interaction.

In their extensive review on deuteron structure, Gilman and Gross [22] derive the full spin-dependent cross-section equation for the reaction of deuteron photo-disintegration, shown below in Eq. (2.1), which uses the centre-of-mass co-ordinate system established in Fig. 2.1.

$$\frac{d\sigma}{d\Omega} = \left(\frac{d\sigma}{d\Omega}\right)_0 \left[1 + p_y^N P_y + p_y^d T - p_\gamma (\Sigma + P_y T_1) \cos 2\phi \right. \\ \left. + P_\gamma^\odot (C_{x'} p_{x'} + C_{z'} p_{z'}) + p_\gamma (O_{x'} p_{x'} + O_{z'} p_{z'}) \sin 2\phi \right] \quad (2.1)$$

Where $(\frac{d\sigma}{d\Omega})_0$ is the spin-independent cross-section formula (or the unpolarised cross section), ϕ is the azimuthal angle of the outgoing nucleon. p_y^N , p_y^d , p_γ and P_γ^\odot are polarisations of the recoil nucleon, the target deuteron, and the incident photon (linear and circular), respectively. $p_{x'}$ and $p_{z'}$ are additional components of recoil nucleon polarisation with respect to the (primed) recoil frame, where z' is the direction of the recoil nucleon. The other variables are polarisation observables, defined below in Table 2.1:

Table 2.1 Meaning of polarisation observables seen in Eq. (2.1) [22]

Symbol	Meaning
P_y	induced polarisation of recoil nucleon (along y')*
T	vector polarised target asymmetry (along y)
Σ	linearly polarised photon asymmetry
T_1	tensor target asymmetry (quadrupole spin distribution)
$C_{x'}$	circular polarisation transferred from photon to recoil nucleon (along x')
$C_{z'}$	circular polarisation transferred from photon to recoil nucleon (along z')
$O_{x'}$	linear polarisation transferred from photon to recoil nucleon (along x')
$O_{z'}$	linear polarisation transferred from photon to recoil nucleon (along z')

If we consider a scenario where we use a circularly polarised photon beam, and an unpolarised deuteron target, then many observables disappear, leaving a simplified equation:

$$\frac{d\sigma}{d\Omega} = \left(\frac{d\sigma}{d\Omega}\right)_0 [1 + p_y^N P_y + P_\gamma^\odot (C_{x'} p_{x'} + C_{z'} p_{z'})] \quad (2.2)$$

Gilman and Gross note that $C_{x'}$ and P_y are the real and imaginary parts of the same combination of helicity amplitudes which together fully describe the complex representation of spin transition

*Considering the full reaction diagram, it would be more intuitive if P_y was instead denoted as P_γ , as is the case in other papers. Some sources simply denote it as P [20]. P_y is simply a common convention that this thesis maintains, likely stemming from the fact that this single polarisation observable needs to only consider one set of axes (no primed axes needed) which are clear in context.

probabilities of deuteron photo-disintegration. Therefore, an experimental measurement of both simultaneous observables is highly valuable, and Eq. (2.2) will therefore be important for the analysis goals.

2.1.1 Probing Higher Energies

In scattering experiments, as energy, E , or momentum transfer, Q^2 , increases, we begin to probe smaller structures of particles (larger scattering angles also correspond to a larger Q^2). Conventional nuclear physics is well-described when considering only meson–baryon interactions. However, as we increase energy and begin to probe the hard scattering regime ($E_\gamma \sim 1 - 2 \text{ GeV}$), quark-gluon interactions become relevant. Beyond $\sim 2 \text{ GeV}$, it is expected that quark-gluon degrees of freedom dominate entirely. One model of how this manifests in differential cross sections is given by the simplified quark counting rule. For deuteron photo-disintegration, this says that the cross section should have a s^{-11} dependence [23], where s is the Mandelstam variable, representing centre-of-mass energy squared [9]. However, experimental data shows deviation from this rule as we enter the hard scattering regime. Cross sections have instead been shown to scale according to counting rules re-derived from QCD and quark-gluon string models [24] (seen in Fig. 2.2).

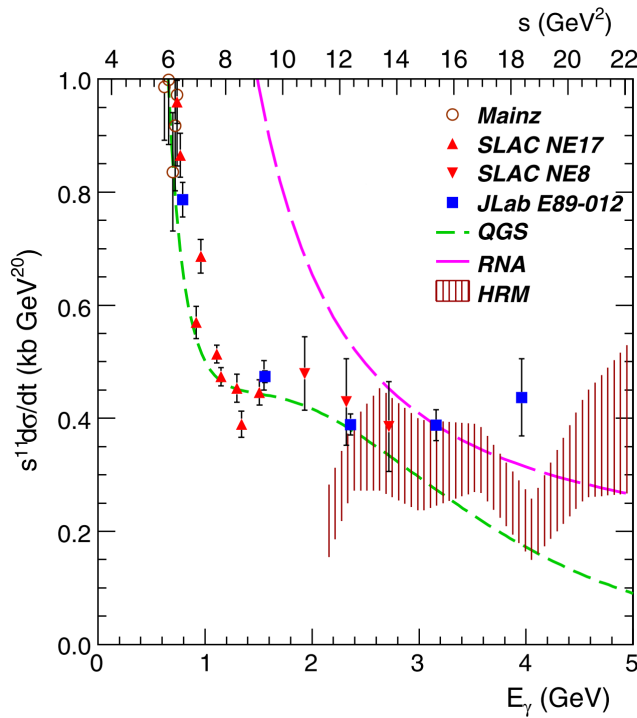


Fig. 2.2 Figure taken from [24], showing invariant cross section of $d(\gamma, p)n$ against photon energy, E_γ and Mandelstam variable, s . Data taken from previous work [23, 25–31] is compared with a quark-gluon string (QGS) model, a reduced nuclear amplitude (RNA) model and a QCD hard re-scattering model (HRM).

Since there is little available data on pn helicity amplitudes in the hard-scattering regime and beyond, associated models must be estimated based on theoretical frameworks [32]. There is therefore a large motivation for constructing a detailed analysis of deuteron photo-disintegration at higher energies, especially within the quark-gluon dominated regime. Additionally, a polarisation analysis could lead to further constraints on associated models by considering spin and angular dependence.

2.2 Dibaryons and Hexaquarks

As mentioned in the introduction to this chapter, a main motivator of this project is understanding and searching for so-called hexaquarks, which will be the focus of this section. The hadron physics working group at the University of York has a particular expertise in hexaquarks, with members playing major roles in recent hexaquark-related developments [1, 33]. Naturally, this project is also highly motivated by that interest.

Dibaryons and hexaquarks are closely related concepts. A dibaryon is defined as any particle with a baryon number of 2 ($B = 2$). As covered in the introductory chapter, quarks contribute $1/3$ to this quantum number, and anti-quarks contribute $-1/3$. This means for a particle to have $B = 2$, the number of quarks minus the number of anti-quarks has to be six [34]. The simplest and most precisely measured dibaryon is the deuteron (d), discussed in the previous section. As for "hexaquark", there are two definitions. The more general definition is any particle containing a total of any six quarks or anti-quarks*. This includes both 6 quark structures (q^6) and half quark, half anti-quark structures ($q^3\bar{q}^3$) [36]. Therefore, not all hexaquarks are dibaryons. $q^3\bar{q}^3$ structures are instead known as baryonium [35].

While the deuteron may be considered a single particle, and therefore a hexaquark under this broader definition, its structure is formed of two well-separated, yet interacting "bags" of quarks which exchange mesons, making it a *molecular* dibaryon. Far more interesting, however, is a structure with all six quarks contained in one body. This is what we consider a *genuine* (or "non-trivial") hexaquark (see Fig. 2.3 for a visual representation of this difference). Such a bound state presents a non-conventional, exotic state of matter that reshapes our understanding of QCD, going beyond the standard quark configurations of mesons and baryons.

*This all-encompassing definition for multi-quark states (hexaquark, pentaquark and tetraquark) that does not distinguish between di-molecules and singular multi-quark objects was adopted by CERN, due to internal structures of multi-quark families not yet being established [35].

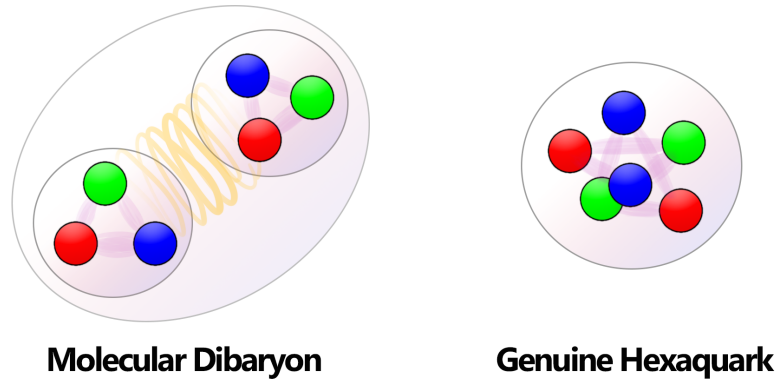


Fig. 2.3 Diagram to visualise the difference in quark arrangement between two profoundly different particles that could each be considered both a dibaryon ($B=2$) and a hexaquark ($6 \times q$).

2.2.1 $d^*(2380)$

Genuine hexaquark particles were first theorised by Dyson and Xuong in 1964 [37], but decades of searching did not yield experimental evidence [34]. Recently, however, there has been a renewed interest due to the discovery of the $d^*(2380)$ resonance [38–40]. This resonance decays into a conventional Δ - Δ system, but cross-sectional analysis finds that its mass ($2380 \text{ MeV}/c^2$) is $\sim 90 \text{ MeV}/c^2$ smaller than simply the mass of two Δ s, and the width of the resonance is noted to be much narrower than expected from conventional meson exchange as with a molecular dibaryon [41]. This indicates that a novel particle is formed at this resonance, with all six quarks contained together – the first non-trivial hexaquark. Initially, more exploration and data was needed for this to be more convincing, however the small cross section and high background channels make $d^*(2380)$ analysis difficult.

The quark arrangement of $d^*(2380)$ ($\uparrow\uparrow\uparrow\uparrow\uparrow\uparrow$) gives it a spin of 3. Polarisation analysis therefore enables a higher sensitivity to the particle by observing changes in polarisation (and associated observables) in the resonance region of the $d^*(2380)$, and isolating spin-3 particles. This also allows an exploration of its electro-magnetic properties. Such an analysis was done by M. Bashkanov *et al.* [42] in an experiment that ran at the MAMI experimental facility [43, 44] in Mainz, Germany. This analysis led to the most convincing proof yet of the $d^*(2380)$'s existence and non-trivial hexaquark nature. Naturally, more analysis of this resonance is desired, which is a large motivator behind the work described in this thesis.

2.2.2 Dibaryon Multiplets

In a similar fashion to the SU(3) hadron multiplets from Sec. 1.4, a dibaryon multiplet can be made from the possible pairings of SU(3) ground-state baryons. Deuteron (pairing of pn) is a spin-1 particle, and so it belongs to the $J = 1$ antidecuplet (Fig. 2.4), often simply called the deuteron multiplet.

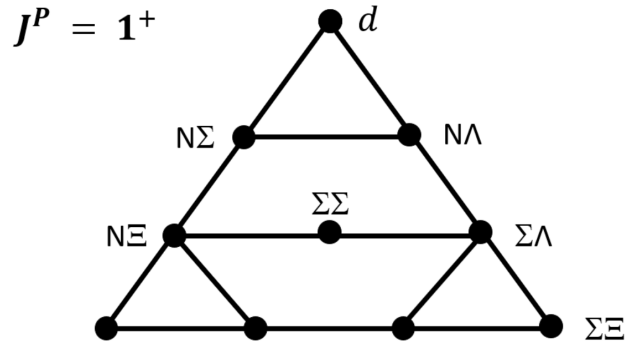


Fig. 2.4 The deuteron antidecuplet (SU(3) $J = 1$) [35].

In this well studied dibaryon group, only the deuteron can form a bound state. The rest are only "virtually bound", existing only briefly in scattering reactions before decaying. Again, like before, these particles can be excited to a resonance, through an increase in angular momentum. The $J = 3$ antidecuplet (Fig. 2.5) represents the possible dibaryons that can be made from the pairings of $J = 3/2$ baryons. The $d^*(2380)$ sits at the top, however this group theory predicts further resonances with increased strangeness. Given that the $d^*(2380)$ has been shown to be dominantly a genuine hexaquark state, these higher resonances could follow suit, making it a logical avenue of investigation for further hexaquark studies. Fellow researchers within the University of York's hadron physics group have worked towards experimentally proving these stranger d^* resonances, which also utilise polarisation analysis [45, 46].

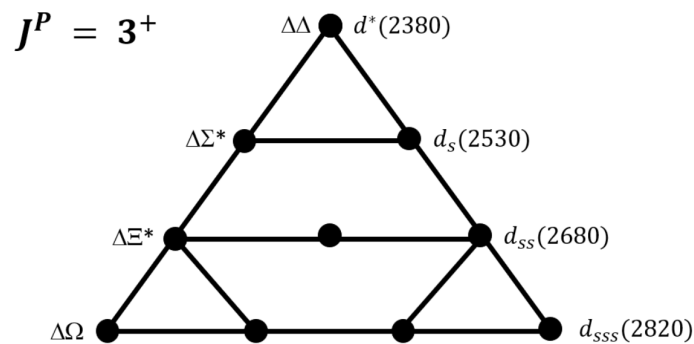


Fig. 2.5 The $d^*(2380)$ antidecuplet (SU(3) $J = 3$) [35].

2.3 Short Range Correlations

A short-range correlation (SRC), is a temporary structure that forms inside atomic nuclei via the interaction between nucleons. Inside a nucleus, nucleons are turbulent due to competing forces. Electrostatic forces work to repel nucleons, while the strong force is repulsive at short range, but attractive at larger ranges. Occasionally, due to this turbulence, a pair of nucleons may effectively overlap. During this very short-lived state, the nucleons involved have high momenta. If one nucleon in an SRC is knocked out by a scattering reaction, both nucleons in the pair are knocked out, and emitted diametrically opposite to each other, suggesting they were bound in some way. Studies have shown that almost all high momentum nucleons form SRCs [47], with the most common pair configuration being pn .

SRC pairs are a possible explanation for the EMC effect, so named after the European Muonic Collaboration who first discovered the phenomenon at CERN [48]. This revelation (shown in Fig. 2.6) showed that the structure of a nucleon in a heavy nucleus is different to the same nucleon in a lighter nucleus (or an equivalent free nucleon). This difference changes across values of the Bjorken scaling variable, x_B , a dimensionless parameter that denotes the longitudinal fraction of the nucleon's momentum carried by the struck parton (quark or gluon) in a scattering reaction. The EMC effect showed physicists that there is a flaw in our current understanding of the structure of baryons, and their interaction.

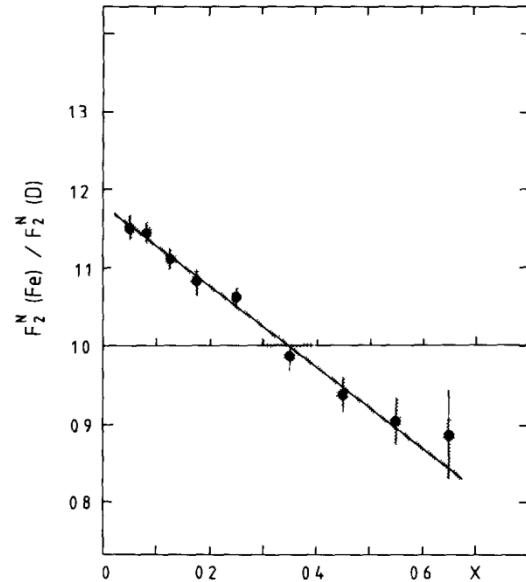


Fig. 2.6 The famous figure from [48], through which the EMC was termed. Showing the ratio of structure functions between iron and deuterium vs Bjorken x .

While not the primary goal of the thesis, it was recognised that providing a more available method of measuring neutron polarisation opens the door to many other analyses, including more detailed studies on SRCs which can explore their spin structure.

Chapter 3

Past Measurements

From the previous chapter, the goal of this thesis is now understood as providing an original, neutron-focussed polarisation analysis of deuteron photo-disintegration, by developing a unique method of doing so that does not require dedicated polarimetry equipment. It is hoped that the developed technique herein is utilised beyond this analysis. This chapter will review previous work that has already provided measurements of neutron polarisation observables, so that gaps or weaknesses can be identified and hopefully addressed. The recent work of M. Bashkanov *et al.*, the motivations of which align closely with those of this thesis, will also be discussed and focused on, as many of the techniques are later used in Chap. 5. From here onwards, P_y and $C_{x'}$ will specifically refer to neutron polarisation observables in deuteron photo-disintegration, unless otherwise stated.

3.1 Historic Experimental Status

As touched on in the previous chapter, a 2002 article on deuteron structure by Ron Gilman and Franz Gross [22] of Jefferson Lab provides a detailed section on deuteron photo-disintegration. Within this, a detailed list of past measurements of associated polarisation observables is provided. This extensive list shows that polarisation analysis of deuteron photo-disintegration is well studied, and goes back many decades. However, the vast majority are focused on the recoil proton rather than the neutron, due to the relative difficulty in extracting neutron polarisation, as discussed in previous chapters. As such, there are no listed measurements of $C_{x'}$, and only eight for P_y , which are given below in Table 3.1, along with the beam energy (E_γ) used, and the angle at which the recoiling neutron was measured using the centre-of-mass frame, ($\theta_{c.m.}$).

Table 3.1 Past measurements of induced neutron polarisation P_y , as listed in [22].

Laboratory	E_γ (MeV)	$\theta_{c.m.}$ (°)	Number of points	Year published
Livermore	2.75	50-136	5	1961
Zürich	2.75	44, 94	2	1963
Illinois	12-23	148	4	1963
RPI	12-30	90	3	1963
Livermore	2.75	32-152	7	1965
Yale	7-30	48-94	20	1972
Yale	7-13	90	3	1976
Argonne	6-14	90	6	1983

From this, we can see a lacking world dataset, with a complete absence of $C_{x'}$, and P_y having few measurements which are restricted to very low energy ranges, and many gaps in $\theta_{c.m.}$. This gives urgency to providing published results of higher energies, and more complete angular coverage. It also gives more importance to $C_{x'}$ measurements than P_y , though it is preferable to extract both simultaneously, as $C_{x'}$ and P_y together fully describe a bilinear amplitude combination, as explained in Sec. 2.1. This therefore represents a valuable constraint for models of the full reaction of deuteron photo-disintegration.

3.1.1 Regarding Energy Ranges

As discussed in Sec. 2.1.1, the energy chosen for a scattering reaction determines how finely a structure is probed. Predictions of higher energy ranges are largely uncertain, but represent a transition from the more understood conventional nuclear structure to quark-gluon degrees of freedom, which is expected to be seen in both protons and neutrons. The P_y energy ranges shown in Table 3.1 are all very low, making them irrelevant to hadron physics, and were instead explorations of nuclear structure/binding. For P_y^p and $C_{x'}^p$, the highest recorded energy range comes from JLab [49], which reached a photon energy of 2.4 GeV (data shown on Fig. 3.1). The scarcity of high-energy polarisation measurements puts emphasis on the need for more such analyses. It is expected that many such analyses will become feasible through the novel technique described in this thesis.

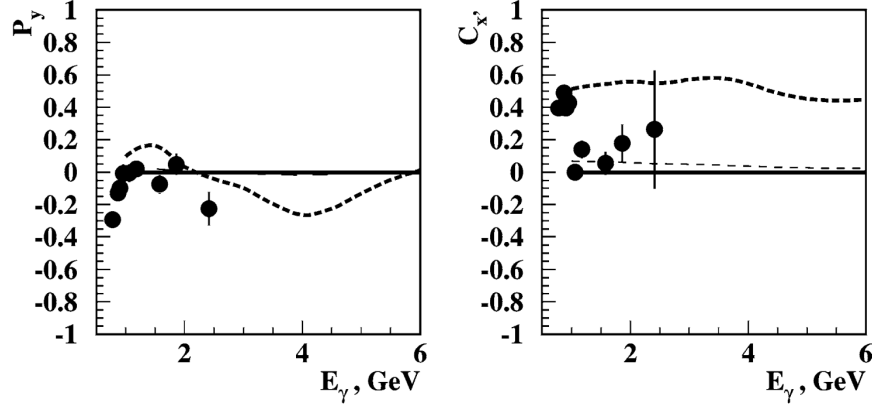


Fig. 3.1 Figure taken from [32]. Dashed lines show "off-shell" predictions of proton P_y^p and C_x^p at $\theta_{sc} = 90^\circ$. Measurements from [49] also presented.

3.2 MAMI Analysis (2023)

M. Bashkanov *et al.* published the first measurements of neutron $C_{x'}$ in deuteron photo-disintegration in 2023 [1]. This measurement (shown in Fig. 3.2) gives $C_{x'}$ as a function of neutron scattering angle, θ_N and photon energy, E_γ , which includes a wide angular coverage and an energy range of 300-700 MeV. As with M. Bashkanov *et al.*'s previously discussed analysis [42], a particular interest was given to the region of the $d^*(2380)$ resonance.

The Mainzer Microtron (MAMI) facility [43, 44], on which this analysis is based, benefits from dedicated polarimetry equipment. A new large acceptance neutron polarimeter [50] was utilised in the experiment, which relies on a $^{12}\text{C}(n,p)$ charge exchange reaction occurring inside a graphite cylinder which surrounds the target. The well-understood scattering reaction, $np \rightarrow pn$, allows for the neutron polarisation to be analysed through the angular distribution of rescattered protons. This two step reaction allows Eq. (2.2) to be further simplified to an equation of the form:

$$\frac{d\sigma}{d\Omega} = \left(\frac{d\sigma}{d\Omega} \right)_0 [1 + C_{x'} \cdot P_y^\odot \cdot A_y \sin \phi_{sc} + P_y A_y \cos \phi_{sc}] \quad (3.1)$$

Where A_y is the analysing power of the charge exchange scattering reaction, and ϕ_{sc} is the azimuthal scattering angle of the rescattered proton, with respect to the recoil neutron (the full reaction is visualised later in Fig. 5.1). Note that $C_{z'}$ has zero contribution, and is therefore neglected (to be explained in Sec. 5.3). This avoids an additional dimensional parameter.

In order to extract $C_{x'}$, it was parameterised as a continuous function depending on θ_N and E_γ . P_y was left as a single free parameter (shown to have negligible effect), further simplifying the analysis. This ultimately allows $C_{x'}$ to be described as a surface of values. The techniques used to acquire these results will be explained in more detail in Chap. 5, as the analysis within this thesis follows a similar procedure.

As seen in Fig. 3.2, this published measurement of $C_{x'}$ covers a good range of photon energies, including the region of the $d^*(2380)$ resonance. However the result is subject to large statistical and systematic uncertainties. This incentivises a higher statistics analysis that follows the same procedure. It is also desirable to extend the energy range to cover the hard scattering regime. M. Bashkanov *et al.* also provides a visualisation of $C_{x'}$ values at fixed angles, providing functions of $C_{x'}$ with respect to E_γ , shown in Fig. 3.3. This allows a direct comparison to previous theoretical and experiment values of both $C_{x'}^n$ and $C_{x'}^p$. Visualising $C_{x'}^p$ alongside $C_{x'}^n$ is important in the context of $d^*(2380)$, as both recoiling product particle spins must be measured to infer the spin-3 $d^*(2380)$ particle.

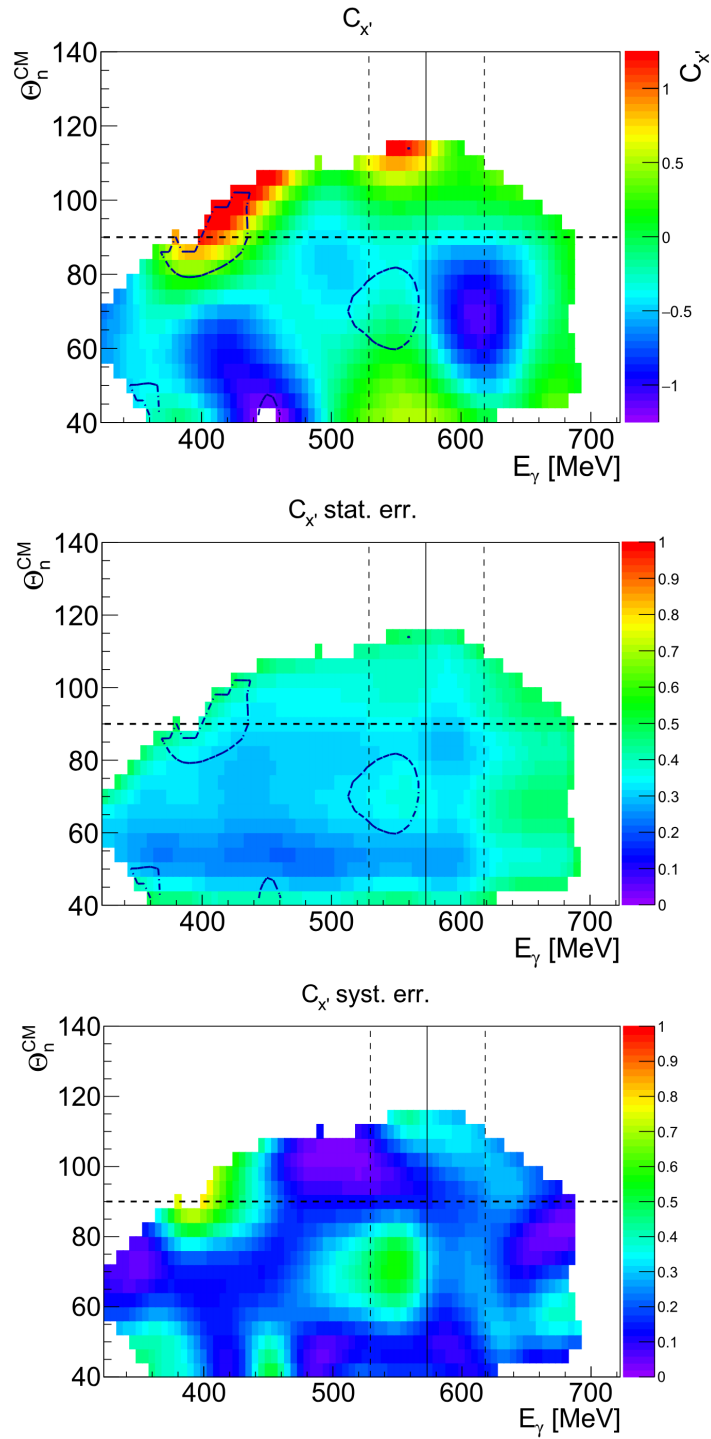


Fig. 3.2 Published measurements of neutron C_x' in deuteron photo-disintegration from [1]. Showing (top) two-dimensional C_x' dependence as a function of neutron centre-of-mass angle, Θ_n^{CM} and photon energy, E_γ . The middle (bottom) plot shows the corresponding statistical (systematic) uncertainties. Contour lines of the systematic uncertainties around 0.4 and 0.8 are also shown on the top and middle plots as dash-dotted lines. The vertical lines show the nominal $d^*(2380)$ pole position (solid) and width (dashed) as given by [51, 52].

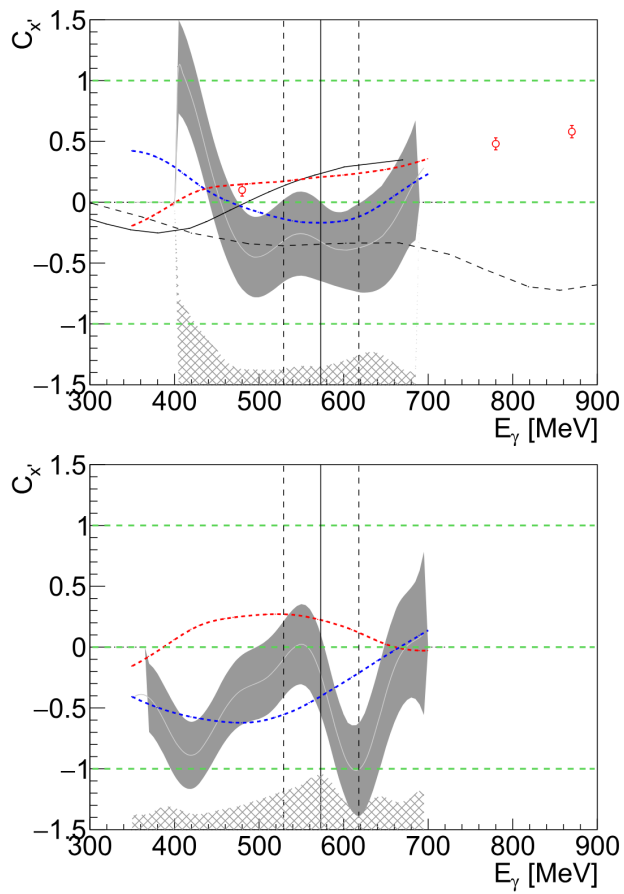


Fig. 3.3 Taken from [1]. $C_{x'}$ for $\Theta_n^{CM} = 90^\circ$ (top) and $\Theta_n^{CM} = 60^\circ$ (bottom) are shown as a light grey line with statistical errors as a grey band and systematic errors as the hatched area on the bottom axis of each plot. Previous $C_{x'}^p$ from [53] are shown as red markers. Calculations for $C_{x'}^p$ from [54] and [55] are shown as solid and dashed lines respectively. Calculations for C_x^p (red) and C_x^n (blue) from A. Fix are shown as dotted lines. Vertical lines show nominal d^* pole position (solid) and width (dashed).

Chapter 4

Experimental Facility - Jefferson Lab



Fig. 4.1 An eastward-facing aerial photograph of Jefferson Lab's CEBAF during the 6 GeV era, predating the construction of Hall D.

Thomas Jefferson International Laboratory, often shorted to Jefferson Lab, or simply JLab, is a US Department of Energy facility located in Newport News, Virginia, USA. Established in 1984 [56], JLab is a world leading laboratory in hadronic and particle physics, housing a unique superconducting radio-frequency accelerator named CEBAF (Continuous Electron Beam Accelerator Facility) which accelerates electrons around a racetrack-shaped beam-line. Once accelerated to a desired energy, electrons are delivered as required to up to four experimental halls lettered A through D, positioned at beam exit points. This allows simultaneous experiments to be done on nuclear targets using high energy electron beams, or alternatively, photon beams via the bremsstrahlung mechanism. CEBAF

and its experimental halls are entirely underground, though the layout of the above-ground service buildings makes the footprint of the facility visible in aerial photographs such as Fig. 4.1.

The maximum electron beam energy that JLab is currently designed to achieve is 12 GeV, however the analysis in this thesis predates the 12 GeV upgrade and construction of experimental hall D (2012-2015), before which, 6 GeV was the maximum. There are plans for another upgrade in the future to raise the energy limit even higher to 22 GeV [57], however, such an upgrade has not yet been officially approved at the time of writing this thesis. The data to be analysed in a later chapter is taken from an experiment known internally as g13, which was performed with CLAS, a detector system that existed during the 6 GeV era. CLAS presents the ideal setup to address the goals of this thesis, providing a large angular acceptance, and world-leading beam energy ranges, with a wealth of already existing data, including deuteron photo-disintegration. In this chapter, the physical setup of JLab will be explained, including the main components of CEBAF, the CLAS detector and its subsystems, and also an overview of experiment g13.

4.1 CEBAF

As shown in Fig. 4.2, the main loop of CEBAF is formed of two anti-parallel linear accelerators, and two connecting electromagnetic arcs. Electrons begin their journey at the injector, and end at an experimental hall. This section will detail each of the major components of this process.

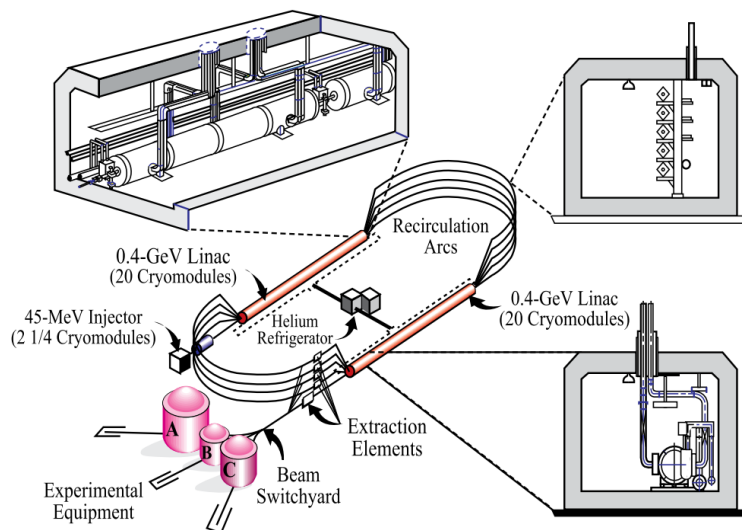


Fig. 4.2 General overview of CEBAF during the 6 GeV era, taken from [58]

4.1.1 The Injector

The role of the injector is to provide electrons to the CEBAF accelerator track. It is capable of producing multiple simultaneous beams, each operating at a rate of 499 MHz [59] (radio frequency) resulting in bursts of electrons released every 2.004 ns per beam, injecting them into CEBAF with an energy of 10 MeV. A phase separation between each beam means that each experimental hall can simultaneously receive a 499 MHz beam by each tuning to accept one phase. Fig. 4.3 shows a layout of the injector.

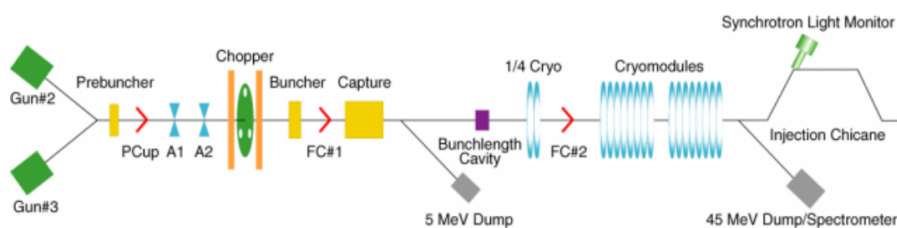


Fig. 4.3 Layout of the CEBAF injector, taken from [59].

The injector begins with a DC photocathode gun, which functions by directing an infrared laser onto a photocathode material made of gallium arsenide (GaAs) [60]. The gun then emits a stream of electrons which travels 6.5 m to a beam chopper, where the beam is "bunched" into pulses of predefined length [61]. The helicity of this beam is determined by the preceding IR laser, which is fine-tuned on a laser table and given polarisation via a Pockels cell, an electro-optic crystal [62]. This results in a longitudinally polarised electron beam, which can be orientated as needed via a spin manipulator. A helicity board, which directly controls the Pockels cell, can be set to give pseudo-random helicity states [63], which is crucial for beam symmetry in polarisation analysis.

4.1.2 Linear Accelerators

As opposed to circular accelerators (or storage rings) as used by facilities such as CERN, CEBAF uses linear accelerators (linacs). This has an advantage over circular accelerators in being a simpler setup, not requiring complex magnetic fields to continuously direct particles on a circular path. There is also no unwanted synchrotron radiation, a source of energy loss that would have to be accounted for in the form of more inserted energy [64]. While the linac presents a simpler and more cost-efficient design, the main disadvantage is the inefficient use of the accelerator, with only one pass from injection to dump. This problem is addressed with recirculating linacs, where particles are re-fed into the linac

multiple times between beam injection and beam dump. Jefferson Lab, which uses two anti-parallel linacs in the same loop, was the first laboratory to implement this recirculating linac technology on such a large scale, though the concept had been well established by labs such as Stanford's High Energy Physics Laboratory (HEPL) and MIT's Bates Laboratory [65].

At the heart of the linac's design are niobium cavities (Fig. 4.4). Niobium (Nb) becomes superconductive at temperatures close to absolute zero, and the cavities are shaped in such a way as to create a standing electromagnetic wave when supplied with radio frequency voltage, which provides acceleration to charged particles travelling through the hollow centre. The elliptical cavity shape also yields low peak surface electric fields, and good mechanical rigidity [67].

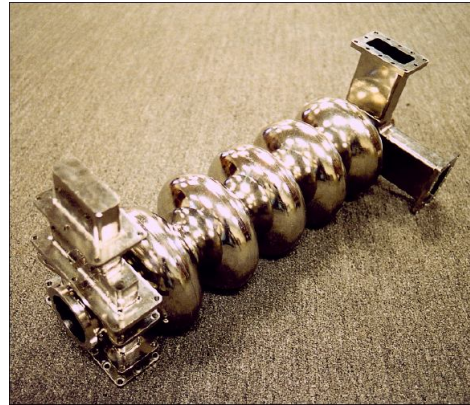


Fig. 4.4 Photograph of a single 5-cell niobium cavity as used in CEBAF's linacs [66].

The linacs are made with arrays of cryogenic modules/units (Fig. 4.5), each consisting of a pair of these 5-cell niobium cavities supplied with radio frequency voltage. This is kept at a temperature of 2 K by a liquid helium bath supplied to the unit.

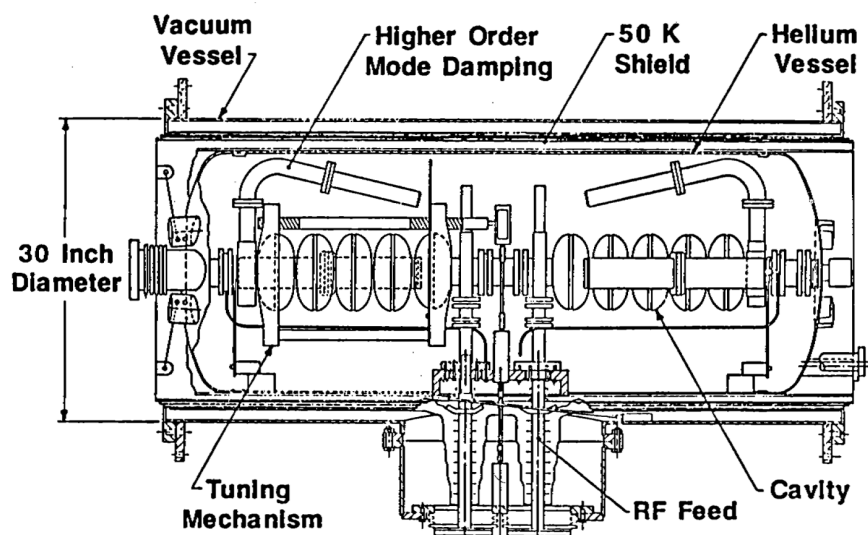


Fig. 4.5 Diagram of a single linac cryo-unit [67].

4.1.3 Recirculation Arcs

In order to complete the full-track circulation, electrons leaving one linac must be redirected to the other. This is the role of the recirculating arcs, which use electromagnets to both direct the electron beam, as well as maintain its focus. However, electrons on different "laps" occupy the same space inside the linacs, and so there is a mix of electron energies in a single beamline which each require different strength magnetic fields in order to be redirected equally [64, 66]. For this reason, each "lap" of CEBAF requires an individual transport mechanism to accommodate the momentum of a specific beam energy.



Fig. 4.6 Photograph of the western recirculation arcs of CEBAF [66].

To achieve this, electrons leaving a linac first come to a spreader, which separates out the beam via differential vertical bending, according to energy, into separate recirculation arcs [65], which are stacked vertically as seen in Fig. 4.6. An advantage of having unique transport systems for each possible electron energy is that each transport design can be separately evolved to manage each energy-specific synchrotron-radiation-induced degradation of the beam. After being redirected by an arc, the beam passes through a recombiner, the mirror image of the spreader, before entering the next linac.

4.1.4 Beam Delivery

After electrons have reached the required energy, they are finally extracted from CEBAF by means of transverse separator cavities, which give a sideways kick to the electrons [68]. Electrons to be extracted are moved one way, while electrons to be recirculated are moved the other. This transversely separates the beam enough for each path to be differentiated by electromagnets, which further separates them. The radio-frequency separators are tuned to the phase of each of the three phase-separated beams that were introduced by the injector. Each component beam can therefore be manipulated independently, making it possible to serve different halls simultaneously with beams of different but correlated energies [65].

4.2 Hall B

Hall B is one of the three original experimental halls that existed during the 6 GeV era of CEBAF. As shown in Fig. 4.7, this was mostly occupied by the CLAS detector, to be given its own section with individual components discussed. Hall B also houses the tagging facility which enabled real photo-production experiments, to be detailed subsequently in this section. Today, Hall B operates in much the same way, but with CLAS12 [69] taking the place of CLAS. Some more detail on CLAS12 is given in Appendix A, which details a CLAS12 calibration side-project.

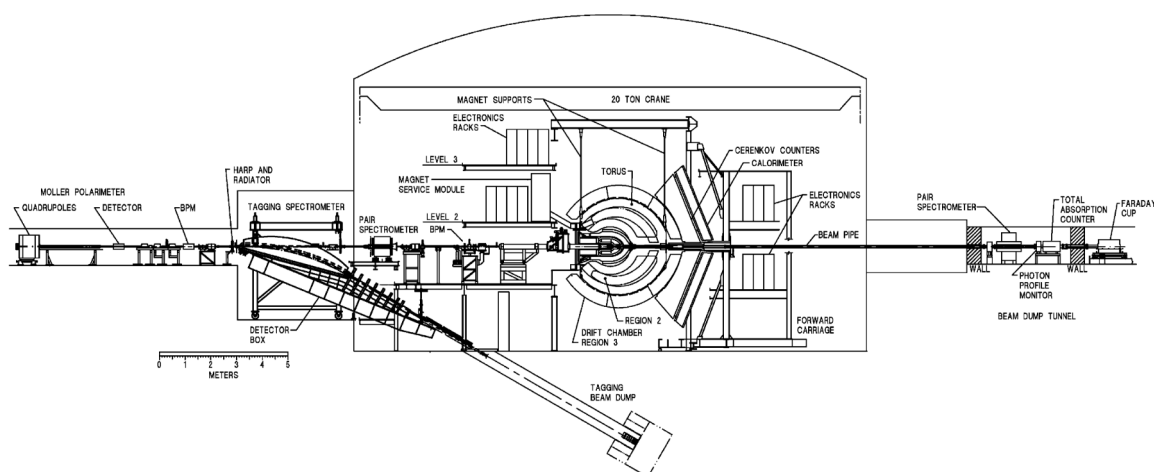


Fig. 4.7 Labelled side-on cross section of Hall B, featuring CLAS, during the 6 GeV era [19].

4.2.1 The Bremsstrahlung Tagging Facility

Unique to Hall B is the photon-tagging system, which made it possible to use photon beams instead of CEBAF's standard electron beam. This is achieved through the bremsstrahlung photon tagging system, which was first implemented in 1998 [70]. This system is based on the bremsstrahlung mechanism (taken from German, meaning "breaking radiation"), in which an electron of incident energy, E_0 is decelerated (scattered) by the electromagnetic field of an atomic nucleus, and in the process emits an energetic photon (gamma ray). In this process, the energy transferred to the nucleus is negligible, and so through energy conservation, the energy of the emitted photon, E_γ , is equal to the difference between the initial and final energy of the electron, $E_\gamma = E_0 - E_e$.

A photon beam is first generated in Hall B by directing the electron beam from CEBAF through a thin target known as the radiator. Electrons have a probability of interacting with the radiator material, each interaction resulting in a bremsstrahlung photon and a decelerated electron. A gold film is used as the radiator material for its high atomic number, which encourages the bremsstrahlung mechanism. Several radiators of different thicknesses were created in the order of micro/nano meters to limit multiple scattering (see [70] for material specifications). A carbon backing is necessary to support the thinner foils. Note that for a fixed incident electron beam energy of E_0 , a continuous range of E_γ values between 0 and E_0 is generated due to the statistical nature of involved particles, which create a range of possible impact parameters. This E_γ distribution follows approximately a $1/E_\gamma$ dependence, meaning lower-energy photons are more common than higher-energy ones. Meanwhile, the angular distribution of both the outgoing photons and electrons is given by:

$$\theta_\gamma = m_e c^2 / E_0 \qquad \theta_e = \theta_\gamma E_\gamma / E_e \qquad (4.1)$$

Where m_e is electron rest mass. At Jefferson Lab energies (>800 MeV), both of these angles are of order 1 mrad or smaller, which approximates to both the electron and photon continuing in the original beam direction immediately after the bremsstrahlung process. Photons continue onward to a collimator system to further define the beam before it is finally delivered to the desired target in Hall B. The electrons, however, are redirected downward via a magnet, with field strength tuned to the incident beam energy, E_0 , such that any electrons that were not decelerated by the radiator follow a predetermined circular path, arriving at a beam dump under Hall B. Energy-degraded electrons in this same magnetic field will have their path deflected downward even moreso. Instead of making it to

the beam dump, these electrons are intercepted by a hodoscope - an array of scintillators, known as counters, that detect the electrons. A diagram of this set up is shown in Fig. 4.8.

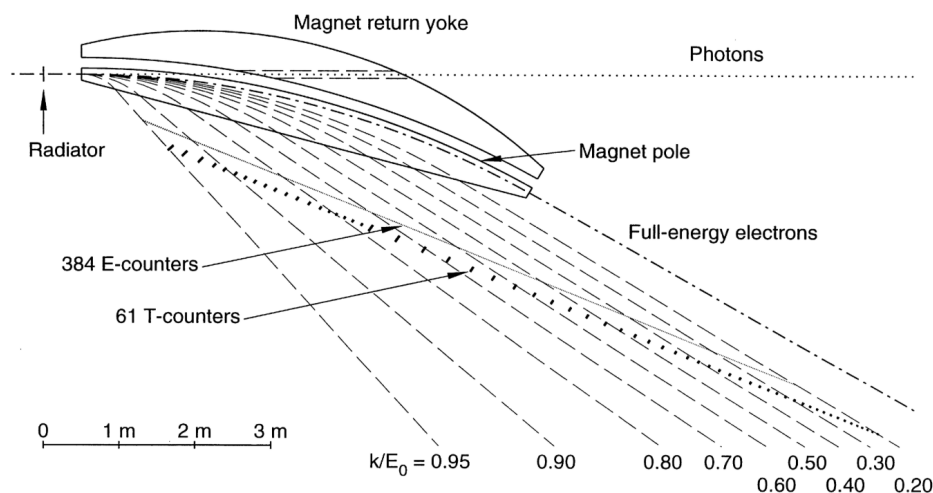


Fig. 4.8 Overall geometry of the bremsstrahlung photon tagging system. Typical electron trajectories are labeled according to the fraction of the incident energy that was transferred to the photon [70].

Because the trajectory of the electrons depends on their energy, there is a direct relationship between E_e and the horizontal position at which electrons exit the magnet. Each detector element in the scintillator plane therefore corresponds to a specific value of E_e . This ultimately allows a calculation of E_γ , which can be assigned, or "tagged" to a downstream photon, assuming the coincident photon is identified. The plane in which this relationship between energy and position is linear is termed the "focal plane" of the magnet. As much of the system as practically possible is kept in vacuum to avoid multiple scattering. While the hodoscope was considered too large for this, much of the electron's path is kept in vacuum until an exit window near the scintillators.

In order for precise tagging, the hodoscope requires both a high spatial resolution for precise momentum measurements, and adequate timing data. Scintillators must therefore be small and numerous, to create high spatial resolution, but also a large enough volume to ensure reliable scintillation. In order to specialise in these two requirements, two different planes of scintillator arrays are used, the E-plane and T-plane. The E-plane (energy) is used only for energy/momentum definition, consisting of 384 thin scintillators, known as E-counters, giving an optimal spatial resolution. The spacing of E-counters in the focal plane translates to approximate steps of $0.3\% E_0$. The T-plane (timing) is 20 cm further downstream, and has fewer (61), but considerably thicker "T-counters", for better timing precision via their light output.

Each detector element in both planes is oriented with its working surface normal to the local electron trajectory, creating a Venetian blinds-like arrangement, as shown in Fig. 4.9. This geometry has the advantage of low angular acceptance of secondary particles, but more importantly, allows for detector elements to overlap from the perspective of incoming electrons. This creates additional energy bins in the E-plane by considering each unique overlap area as its own bin, recorded as being hit when both associated E-counters fire in coincidence, due to a passing electron intercepting both. Each of the 384 equally sized E-counters overlaps its adjacent neighbours by one third, thus creating 767 possible energy bins in steps of $\sim 0.1\% E_0$.

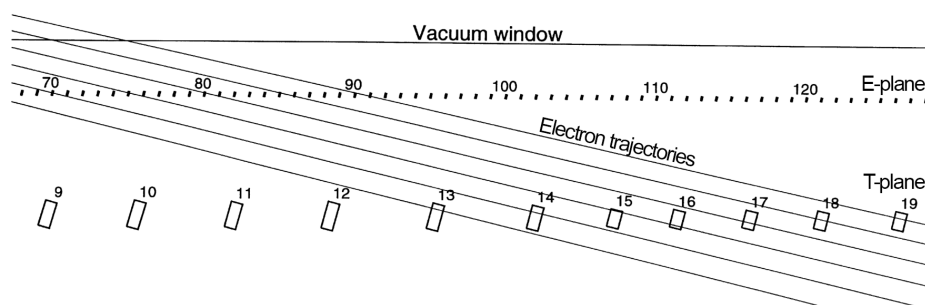


Fig. 4.9 A scale drawing of a short section of hodoscope with a few typical electron trajectories superposed. Shows the "Venetian blinds" geometry and indicates the general relationship between the E- and T-planes of scintillators [70].

As stated, precise timing measurements are also necessary to assign the correct value of E_γ to a downstream photon. When an electron creates light in a T-counter scintillator, the signal is read from photo-multipliers (PMTs) at both the left and right side, with light travel time already considered. As mentioned earlier in this chapter, electron beams in CEBAF are generated in bunches that occur every 2 ns. The electron beam current is tuned such that no more than one photon per electron bunch can be associated with a subsequent particle event. However, beam bunches must still be differentiated. This necessitates a timing resolution that is significantly less than the bunch period of 2 ns. To this end, the design goal for the T-counters was to have a standard deviation of 300 ps in measurements of photon coincidence time. Testing showed that the standard deviation is approximately 110 ps, far exceeding this goal. This timing resolution is seen in Fig. 4.10.

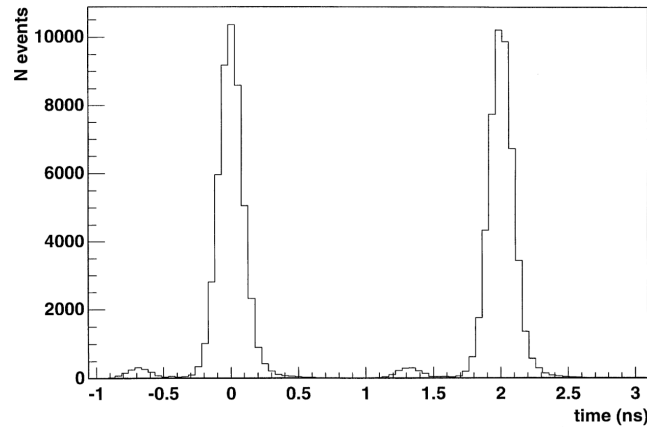


Fig. 4.10 Tagger timing spectrum taken from [70], showing the timing resolution of the tagger T-plane. The 2 ns interval between beam pulses into Hall B is apparent. Also visible are smaller bumps corresponding to spilled over pulses intended for an adjacent hall.

Regarding Polarisation

When using longitudinally polarised electrons, as is the case at CEBAF, the bremsstrahlung process will produce photons that possess circular polarisation [71], with resulting photon polarisation proportional to longitudinal electron polarisation [72]. The carried polarisation is also proportional to the amount of energy transferred from the electron to the photon in the bremsstrahlung process, which is expressed by the Olsen-Maximon formula [73], shown below:

$$P_{\odot} = P_e \frac{4x - x^2}{4 - 4x + 3x^2}, \quad x = \frac{E_{\gamma}}{E_0} \quad (4.2)$$

Where P_{\odot} is photon polarisation, P_e is electron polarisation, and x is the ratio of photon energy, E_{γ} to initial electron energy, E_0 . To create longitudinally polarised photons, however, requires a crystal lattice radiator, which was first implemented at JLab for experimental run period "g8" in 2001 [74] in the form of diamond. Coherent bremsstrahlung photons are created in the lattice due to the interaction of electrons with lattice molecules. Produced photons continue through the lattice in a single direction, but are reflected by the regular separation of lattice molecules. This creates both constructive and destructive interference depending on photon wavelength. Therefore, emerging linearly polarised photons will dominate at a particular photon energy, known as the coherent peak, as shown in Fig. 4.11.

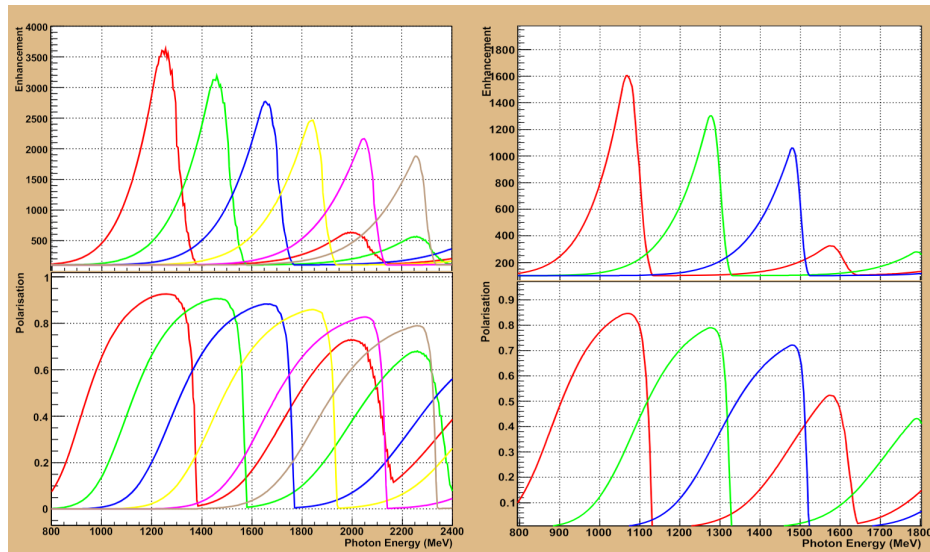


Fig. 4.11 Calculated linear polarisation and enhancement (arbitrary units related to photon flux) as a function of E_γ , for 5 GeV (left) and 3 GeV (right) electron beams. Each colour corresponds to a different goniometer setting, used to shift the edge of the coherent photon peak. Taken from [72].

This means that unlike the case of circularly polarised photons, which have a more continuous energy spectrum, linearly polarised beams are restricted to coherent peaks. The higher-energy limit that the coherent peak allows is called the coherent edge, a value often used in reference to the linear photon beam energy. In order to shift this coherent peak, the distance of regular spacing in the crystal lattice (in the beam-direction) must be changed. This can be achieved by simply rotating the lattice, which can be controlled with a goniometer.

4.3 CLAS

The CEBAF Large Acceptance Spectrometer (CLAS), seen in Figs. 4.12 and 4.13, was a many component detector system housed in experimental Hall B of Jefferson Lab, until it was retired in 2012 [56]. CLAS was designed to detect/track product particles emerging from a target material subjected to an incident beam. The target varied between experiments. The target cell specific to g13 is described in Sec. 4.4.1.



Fig. 4.12 A photo taken of CLAS in its final stages of construction [75]. The TOF counters stand apart from the structure.

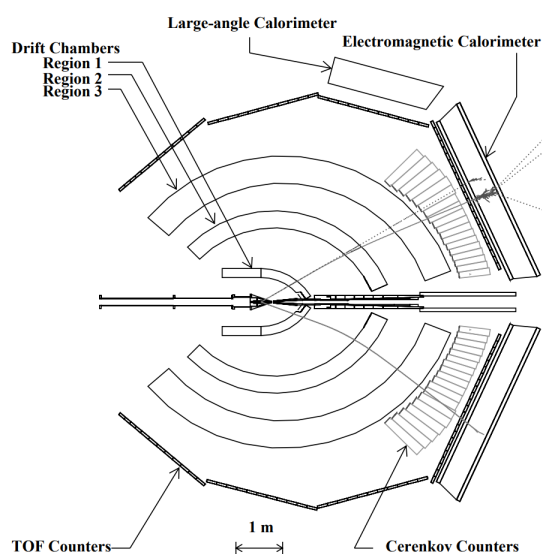


Fig. 4.13 A side-on cross section of CLAS showing the layout of each component, taken from [19]. The incident beam arrives from the left.

CLAS was capable of detecting product particles with momenta greater than 200 MeV/c over polar angles (θ) of 8° to 142° , while covering up to 80% of the azimuth (ϕ) [76]. As well as this wide angular coverage, it accepted electron beam energies up to 6 GeV from CEBAF. Hence, it is sometimes referred to as CLAS6 to further distinguish it from the now upgraded version, CLAS12 (completed in 2017). Such high reaching energy ranges allow for previously inaccessible kinematic regimes in nuclear target scattering experiments, allowing for the investigation of higher energy structures and resonances, furthering our understanding of QCD. The following subsections will each detail the major components of CLAS.

4.3.1 The Start Counter (SC)

The Start Counter was a component of the CLAS detector, utilised in the determination of the start time of events in photo-production experiments. It consisted of 24 plastic* scintillator paddles, each 2.15 mm-thick, and arranged into 6 sectors surrounding the target cell in a hexagonal formation [78], as shown in Fig. 4.14.

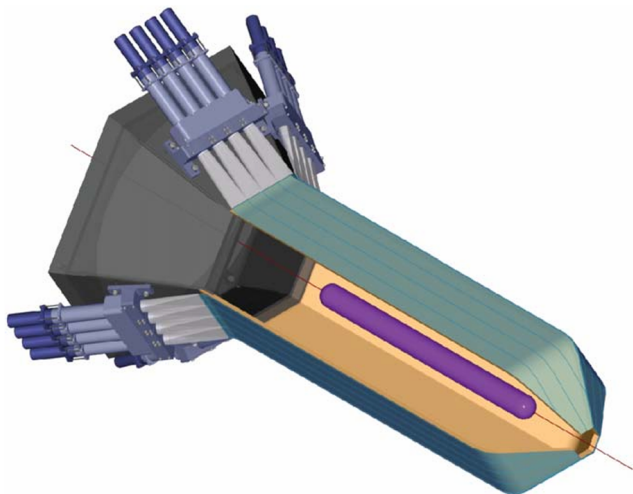


Fig. 4.14 A 3D rendering of the start counter, taken from [78]. A sector is removed to view the interior. The encased scintillator paddles are in green. Photo-multipliers are shown in blue. A general target region is shown in purple. The photon beam (red) travels top-left to bottom-right.

CLAS identifies particles by measuring the time taken to move from the interaction vertex in the target to the outer detectors (to be detailed later in this section). The start counter's role is to measure the time of interaction (i.e. the start time), by detecting particles immediately after (within 2 ns) they are emitted from the target. For this reason, the start counter is the component positioned the closest to the target. When a particle passes through a SC paddle, a light pulse is created in the active material, which is then received by the PMT, and establishes a start time. Due to the segmented scintillator design, some limited azimuthal information is also provided, however, reconstructing the position of the particle is left to other detector components. The start counter is of special importance within this project, as it is utilised for more than the intended purpose. By exploiting its proximity to the target, we can consider re-scattering of outgoing particles, using the active region as a source of secondary reaction vertices.

Before experimental period g13, a different start counter model was used, possessing a 3-paddle structure, with each large scintillator shaped to have a 32.2° bend along its length [79]. The succeeding start counter was instead described as "highly segmented", with its 24 paddles offering more azimuthal

*EJ-200 scintillators were used, which uses polyvinyltoluene (PVT) as a base [77].

information, which the analysis of this thesis utilises. Another improvement from the previous model involved having thinner scintillators (from 3 mm to 2.15 mm), which minimises re-scattering. However, note that this normally undesired possibility is exactly what the unique method of this analysis depends on.

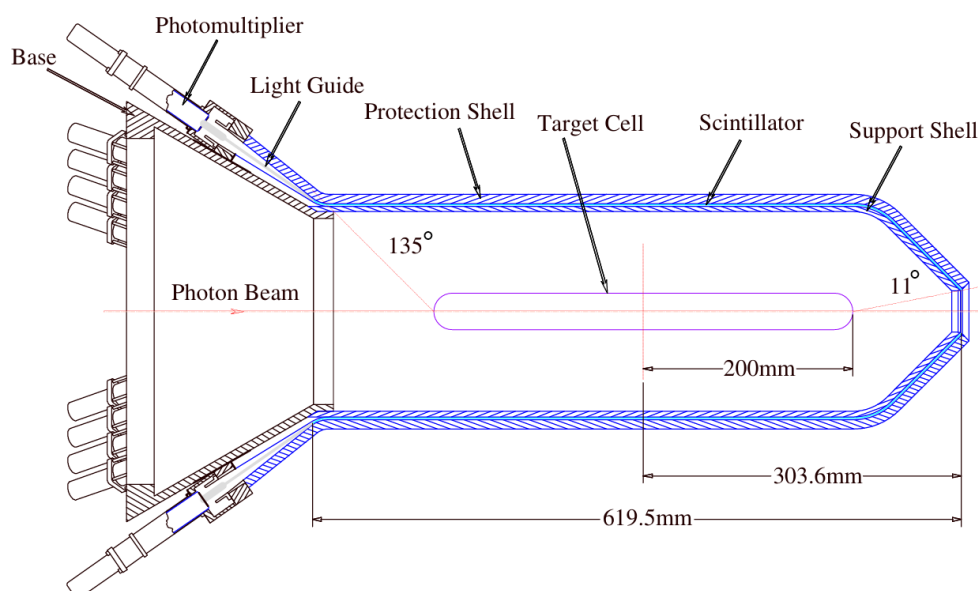


Fig. 4.15 A labelled cross section of the highly segmented start counter used in g13 [78].

This improved SC was also designed to be used in experiments with much longer targets, from 17 cm-length targets in the previous model to 40 cm-length targets. Each SC paddle consists of a single scintillator with a main straight of 502 mm, between a bend at either end, as shown in Fig. 4.15. Upstream, the paddle bends outward towards and light guide and PMT for light pulses to be read. Downstream, the paddle bends inward, converging on the beam line and forming the "nose" of the SC. Each scintillator was individually wrapped in reflective film to ensure internal photon reflection. To further prevent light leaking to neighbouring scintillators, every other scintillator was additionally wrapped in light insulation film. All scintillators are then layered between more light insulation film, and mounted on a support shell. A protective shell is then placed on top. This arrangement is shown in the paddle cross section shown in Fig. 4.16. Introducing this extra material increases the risk of impeding particles, however the tapes used have sub-millimetre thickness, and the shells have a much lower density material when compared with the scintillator, which minimises the chance of rescattering.

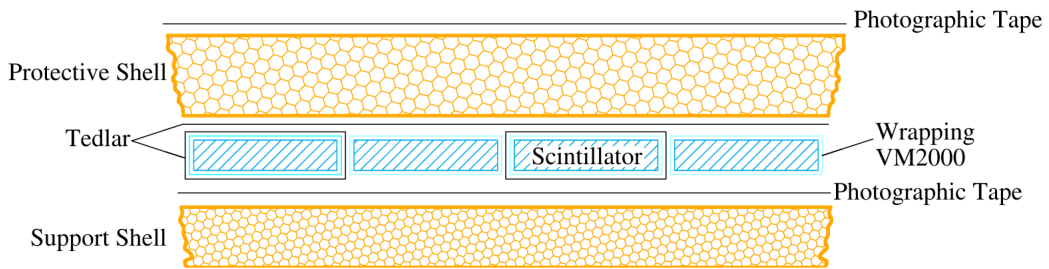


Fig. 4.16 A cross section of one sector of paddles in the start counter, with materials labelled [78].

4.3.2 Torus Magnet

As described by electrodynamics, a particle of charge q and velocity \vec{v} passing through a magnetic field \vec{B} experiences a Lorentz force, $\vec{F} = q(\vec{v} \times \vec{B})$. In particle spectrometers like CLAS, magnetic fields are used to deflect charged particles, which allows them to be differentiated by their momentum. The magnetic field of CLAS is generated by six superconducting coils arranged in a toroidal geometry around the beamline [19]. Its function is to bend charged particles toward or away from the beam axis. The reniform configuration (shown in Fig. 4.17), ensures that forward-going particles, which are typically of higher momentum, experience a greater Lorentz force than particles emitted at wider angles, meaning a better spatial resolution in subsequent detection.

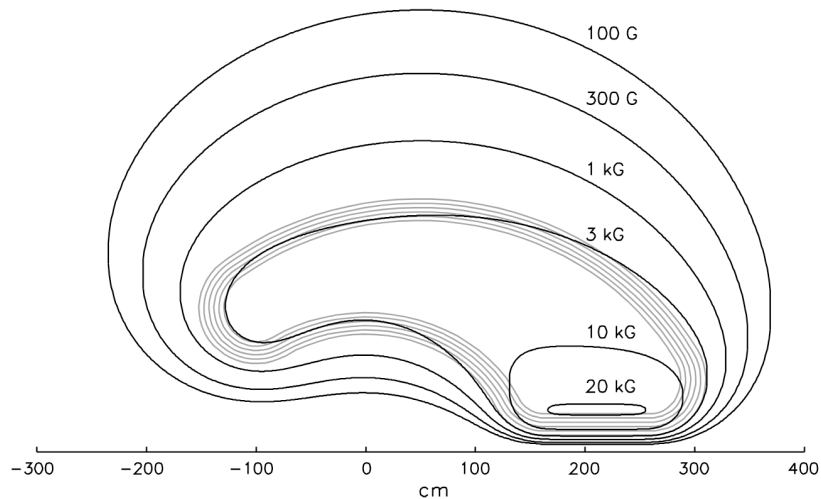


Fig. 4.17 Contours of constant absolute magnetic field for the CLAS toroid in the midplane between two coils, with field strength labelled in units of Gauss. The projection of the coils onto the midplane is shown for reference [19].

Each of the six coils has four layers of 54 turns of aluminum-stabilized NbTi/Cu conductor, which is kept at the super-conducting temperature of 4.5 K by liquid helium fed through cooling tubes located at the edge of the windings. This temperature is further preserved by a liquid-nitrogen-cooled heat shield.

4.3.3 Drift Chambers (DC)

As the torus magnet works to curve the paths of charged particles, the drift chambers (DC) trace the path they take by detecting the ionisation trail they leave behind, obtaining an accurate measure of its curvature, and therefore its momentum. The torus magnet coils divide CLAS into 6 sectors. Within each of these sectors, the DC has three regions, R1, R2 and R3, as shown in Fig. 4.18. R1 is its own self-supporting structure, sitting undivided in the middle of the torus coils. However other regions are segmented by sector, each shaped like orange segments to wedge into the space between coils (Fig. 4.19).

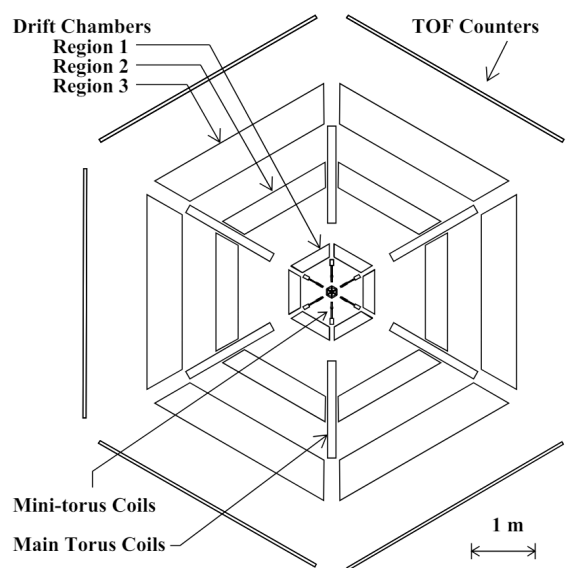


Fig. 4.18 Cross section of CLAS perpendicular to the beamline, showing the layout of the drift chamber's three regions. Note that the mini-torus coils are only present in electron beam runs. [19].



Fig. 4.19 Photograph of a sector of DC-R3, taken during construction [75].

The drift chambers are filled with a gas consisting of argon (Ar) and CO₂ at a ratio of 88% to 12%. This mixture is a compromise between safety (non-flammable) and efficiency, resolution and collection time [76]. The gas is delivered to the drift chambers in parallel by means of a gas-handling system built by a collaboration between Jefferson Laboratory and the nearby University of Richmond.

Threaded through the chambers are nearly 130,000 wires, which run between the two end plates of any given sector. These wires are of two main types: sense wires, responsible for detecting ionisations; and field wires, responsible for creating an electric field to direct ions to the sense wire. The sense wires consist of 20 µm diameter gold-plated tungsten. Tungsten was chosen because of its durability, and the 0.127 µm gold-plating ensures chemical inertness. The field wires are 140 µm-diameter gold-plated aluminium 5056 alloy. Chosen because aluminium has the longest radiation length of any practical wire material and thus minimises multiple scattering. Additionally, the low density allows lower wire tension, and hence minimises forces on the endplates.

Equally spaced sense wires form layers across each region. These are approximately perpendicular to incoming particles to ensure maximum sensitivity to their momenta. Six sense wire layers form a so called "superlayer", and are arranged such that each individual sense layer is azimuthally half a space along, creating a brick-like arrangement. Wire spacing increases radially from the beam line centre. Between each sense wire layer are two layers of field wires, which alternate in a similar way such that they define the vertices of a hexagon-like pattern, with a sense wire at each hexagon centre. This is visualised in Fig. 4.20. This arrangement of wires effectively defines hexagonal detection cells for each sense wire. Each sector consists of two "superlayers", one axial to the magnetic field, and the other tilted at a 6° stereo angle around the radius of each layer to provide azimuthal information. Due to spatial constraints, R1's stereo superlayer contains only four sense wire layers instead of six. A third type of wire, "guard wires", surrounds the perimeter of each superlayer with a high-voltage potential.

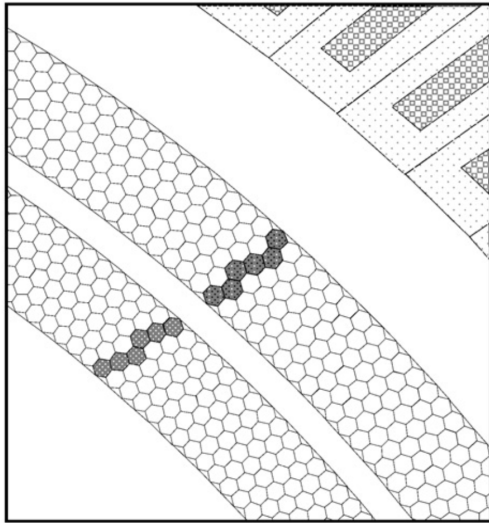


Fig. 4.20 Representation of a portion of an R3 chamber, showing the layout of its two superlayers. The sense wires are at the center of each hexagon and the field wires are at the vertices. The hexagonal cell walls do not represent physical boundaries, but highlight the regular repeated pattern of the wires, and define the cell regions. Also demonstrated is a passing charged particle which causes drift cells to fire (highlighted cells) [19]. Top right shows the cherenkov counters, to be discussed next.

4.3.4 Cherenkov counters (CC)

The Cherenkov counters [80] sit behind the third and final DC region, and span out to a forward polar angle of $\theta = 45^\circ$. They are responsible for detecting electrons, and separating them from pions, which are hard to differentiate using only curvature information from the DC, or energy information from the calorimeters (to be covered in Sec. 4.3.6). This system was only required for electron beam experiments, and was instead turned off for photoproduction experiments such as g13, and is only detailed here for interest. The CC system utilizes the cherenkov (or cerenkov) effect, which occurs when a charged particle moves through a dielectric medium at a speed greater than the speed of light within said medium, creating a forward conical wavefront of photons in the "wake" of the particle. The effect is named after the Russian physicist Cerenkov, who conducted a thorough investigation of the phenomenon in the 1930s [81].

The refractive index, n , is a characteristic property of a material, defined as the ratio of the speed of light in vacuum, c , to the speed of light in the medium, v ($n = c/v$). CLAS uses a gas, perfluorobutane (C_4F_{10}), as the medium to create cherenkov radiation. Each of the six sectors contains about 6 m^3 of this gas. Perfluorobutane has a relatively high refractive index of $n = 1.00153$, which means light travels through it at a speed of $0.998c$. A particle must therefore exceed this speed in order to create cherenkov radiation. Charged pions have a rest mass ~ 272 times greater than an electron [3], and therefore have a much higher cherenkov threshold momentum ($\sim 2.5 \text{ GeV}/c$) in perfluorobutane. This difference means that electrons passing through the medium will produce cherenkov radiation while pions will not, making a clear distinction between the two particles.

In order to preserve CLAS's 80% ϕ coverage, the cherenkov detector elements (photo-multiplier tubes or PMTs) are positioned behind the torus magnet coils, making efficient use of detector space. In order to reach these PMTs, cherenkov radiation from a passing electron is redirected by parabolic aluminum mirrors. There are three mirrors per PMT, and two PMTs per bilateral module, a symmetrical arrangement that covers both halves of a given sector as shown in Fig. 4.21. Because of the magnetic field created by the torus field, magnetic shielding is necessary around the PMTs.

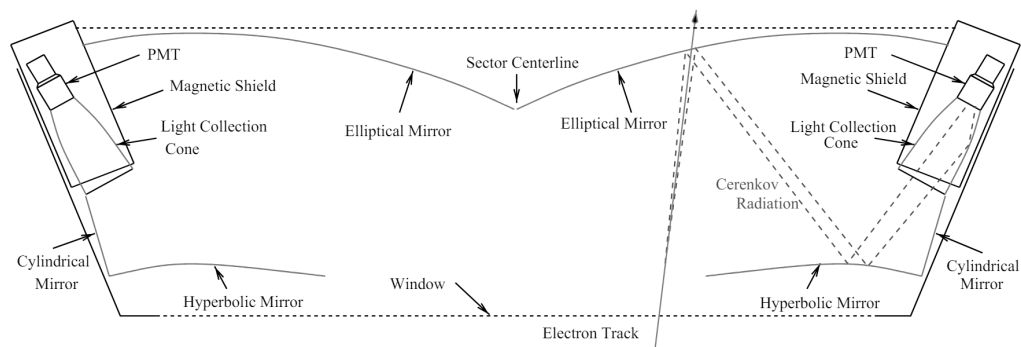


Fig. 4.21 Diagram showing the bilateral arrangement of a cherenkov counter module [19]. A typical electron path is also shown, demonstrating how the generated cherenkov radiation is redirected to a PMT by three mirrors.

Each sector contains an array of 18 bilateral modules, arranged as shown in Fig. 4.22, totalling 216 PMTs altogether. The width of each module increases with θ as the sector diverges away from the beamline.

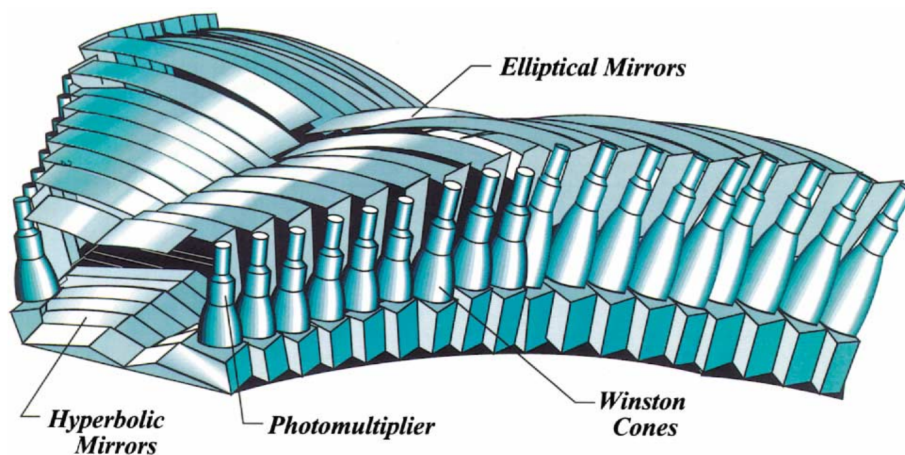


Fig. 4.22 A schematic diagram of the array of optical modules in one of the six identical sectors of the Cherenkov counters.

4.3.5 Time-of-Flight Counters (TOF)

The time of flight counters (TOF) [82] are an array of large plastic scintillators that sit ahead of the CC, covering a large polar range of $8^\circ - 142^\circ$. The TOF counters are used in coincidence with the SC to establish a time taken for a particle to travel between each, providing useful information which assists particle identification. As with all CLAS detector components, each of the six sectors of the TOF contains an identical setup. A single sector is depicted in Fig. 4.23.

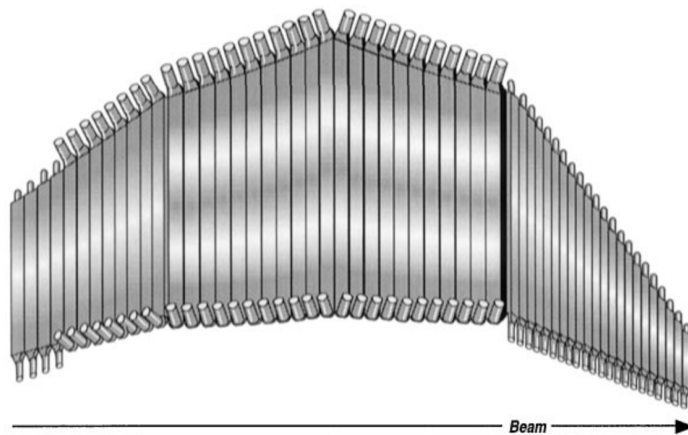


Fig. 4.23 Arrangement of the scintillators in one TOF sector showing all four panels.

The system uses 2-inch-thick BC-408 scintillators. The length and width of each varies, both due to the geometry of CLAS and also considerations for required resolution and cost-efficiency. There are 4 panel regions in each TOF sector, formed of scintillator planes which are perpendicular to incoming particles. Panel 1 is considered the forward angle region, covering a polar range of $8^\circ - 45^\circ$. The 24 scintillators in this region are 15 cm in width. Panels 2-4 are considered the large angle region, covering $45^\circ - 142^\circ$, and mainly consisting of 22 cm-width scintillators.

As with the Cherenkov counters, the inactive region created by the shadow of the torus magnet coils is utilised for the PMTs and their light collection cones, which are mirrored at opposite ends of each scintillator, and receive light generated in the scintillator by a passing particle. The small angle region uses 2-inch-diameter PMTs orientated in line with its adjacent scintillator, however the large-angle region uses 3-inch PMTs orientated at a right angle to scintillator ends, requiring a bending light guide design.

4.3.6 Electromagnetic Calorimeters (EC and LAC)

The final regions, sitting the furthest out from the target in the centre of CLAS, are the calorimeters, responsible for measuring particle energy. This measurement is a destructive process that attenuates particles, which is why it must be the final detector component. There are two distinct calorimeter types covering different angular ranges, each to be discussed in separate subsections which follow.

Forward Electromagnetic Calorimeter (EC)

Covering angles $\theta < 45^\circ$ are the "small angle calorimeters" or EC (electromagnetic calorimeters). The role of the EC is to detect forward-going particles, which includes higher energy electrons, photons, and neutrons. It is made of alternating triangular layers of 10 mm-thick scintillators and 2.2 mm-thick lead sheets. There are 39 scintillator layers in total. Each scintillator layer is made of 36 parallel strips, with each layer orientated 120° to the previous, creating three possible scintillator orientations, referred to as U, V and W, as shown in Fig. 4.24.

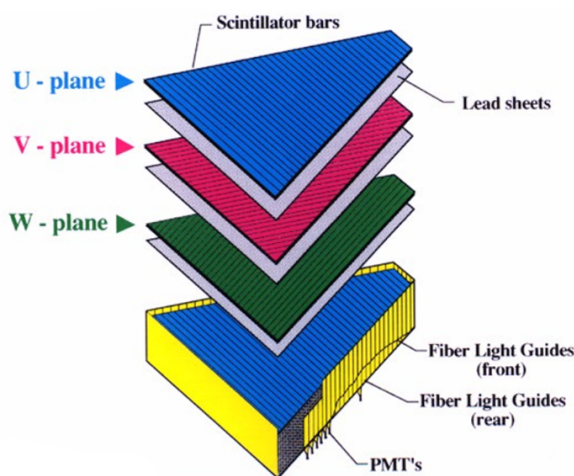


Fig. 4.24 Exploded view of one of the six electromagnetic calorimeter modules [83].

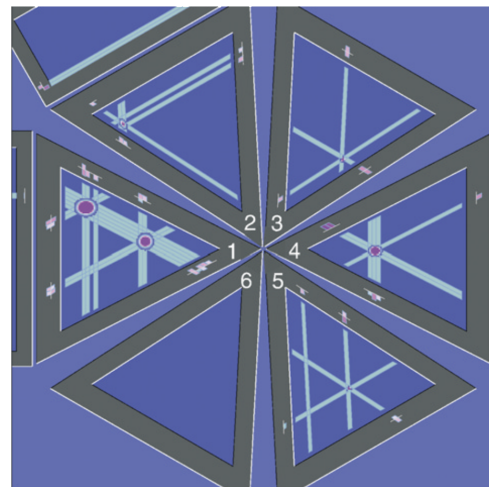


Fig. 4.25 Event reconstruction in the EC. In sectors 2, 3, 4, and 5, a single intersection of peaks on each view (U, V, W) is found, while in sector 1, two hits are reconstructed. The size of the oval at each intersection depicts the transverse energy spread in the shower [19].

Electromagnetic showers originate in the lead sheets from attenuated particles, which propagates through the layers. The energy absorbed in the active material produces a light pulse that is collected at both ends of a scintillator strip, and if over a certain threshold, the scintillator is considered fired by

electronic readout. By using three orientations, the position of the shower can be triangulated and the particle can be reconstructed, as shown in Fig. 4.24. The energy and the time of the hit are calculated by taking into account the path lengths from the hit position to the readout edge.

Large-angle electromagnetic calorimeter (LAC)

The large-angle calorimeter (LAC) provides some detection of scattered electrons and neutral particles, as well as photons originating from radiative processes or π^0/η -meson decay. The LAC covers a polar angular range of $45^\circ - 75^\circ$, however, unlike every other CLAS component, the LAC covers only two of the six azimuthal sectors, providing a sample measurement of particle energies.

In a similar fashion to the EC, the LAC is made of alternating layers of 15 mm-thick scintillators strips and 2 mm thick lead foil, 33 layers in total. There are two alternating arrangements for the strips, each perpendicular to the previous layer, as shown in Fig. 4.26.

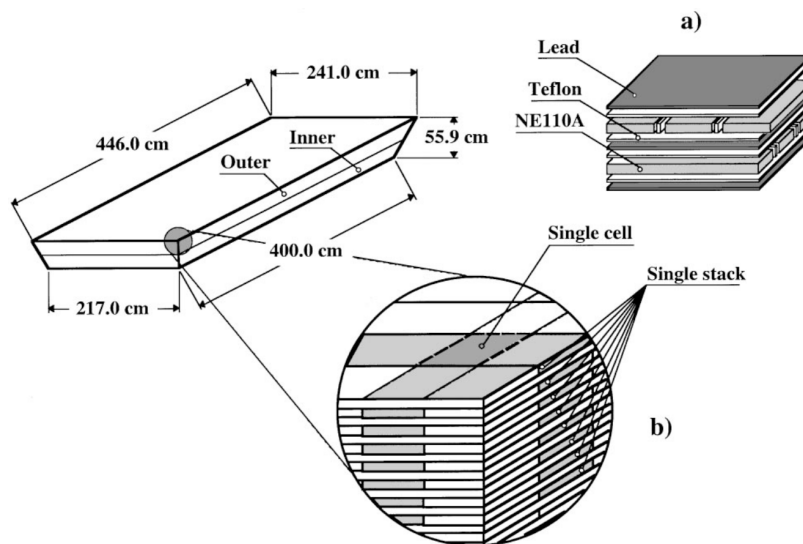


Fig. 4.26 Conceptual drawing of a LAC module showing in detail: (a) the composite internal structure and (b) the plastic scintillators stack structure (light-gray area) with the crossing of two orthogonal stacks that defines a cell (dark-gray area) [84].

4.3.7 Triggers and Data Acquisition (DAQ)

So far in this chapter, it has been discussed how each detector component of CLAS gathers information from product particles emerging from reactions occurring in the target. In order to record this information collectively as "events", a two-level trigger system was designed [19]. The first level

receives the output of PMTs and turns it into a digital signal within 90 ns and no dead-time between readings. This digital information includes the general location of TOF hits, Cherenkov detector signals, and energy deposited in the calorimeter. The level 2 trigger logic can then reject this information if no particle tracks are found in the drift chamber. This is to remove signals that likely came from cosmic background. Likely tracks are identified through a "segment finder", which continuously searches for track segments in the overlapping regions based on template matching.

The trigger supervisor, a custom electronics board, can be set to be more or less restrictive as required by a given experiment. For example, it may be programmed to require only a level 1 input to constitute an event. Upon meeting the requirements for a trigger, events are subsequently queued for readout in CLAS's data acquisition system (DAQ), which takes the digital signal and stores it to disks at a maximum event rate of 2 kHz.

4.4 The E-06-103 experiment (g13)

g13 (or E-06-103*) is the internal name given to one of the many experimental run periods that utilized the CLAS detector. g13 ran over a half-year period between 2006-2007 and was initially proposed to study meson photo-production on deuteron using polarised photons [72], largely motivated by the hunt for nucleon resonances (N^*) as predicted by SU(3). With the utilization of polarised photons, many polarisation observables could be measured in Kaon production of γN , overall creating a high-power analysis.

In order to measure a large set of polarisation observables, g13 consisted of two parts, g13a and g13b, which used a circularly[†] and linearly polarised photon beam respectively, using the mechanisms described in Sec. 4.2.1. For g13a, the circularly polarised photon beam was created with relatively lower electron beam energies (E_e), predominantly E_e of 1.99 GeV and 2.65 GeV [85], which created a range of photon energies (E_γ) below E_e . For g13b, a higher E_e was required. Across all g13b runs, E_e energies in the range of 3.3 - 5.2 GeV were used in conjunction with six unique goniometer configurations. This resulted in six coherent edges for the linearly polarised photon beam, giving an E_γ range of 1.1 GeV to 2.3 GeV. In total, $\sim 3 \times 10^{10}$ events worth of data were collected.

*After approval, Jefferson Lab's Program Advisory Committee (PAC) assigns serial numbers to experiments in the form E-XX-XXX, where XX denotes the year of proposal, and XXX is the sequential number for that year. In some years, 100 is added to distinguish proposals made to a different panel. Hall B uses the form gXX (photo-production) or eXX (electro-production) to group its approved experiments to define run periods. As g13 contained only E-06-103, both numbers refer to the same experiment.

[†]The circularly polarised photon beam helicity was frequently flipped to ensure a balance across all data.

4.4.1 The Cryo-target

Unlike previous analyses that have focused on γp (i.e. with a hydrogen target), this experiment would analyse, in addition, γn . To this end, the experiment used an unpolarised liquid deuterium (LD_2) target, requiring a cryogenic target cell. This cryo-target cell (seen in Fig. 4.27) consisted of a slightly tapered plastic tube, capped at either end, and orientated to point downstream of the beam. Cap-to-cap, this was 40 cm in length, and the cross-sectional area was 51.9 mm^2 at the thicker end, and 40.0 mm^2 at the thinner end [86]. The caps included an electron-beam window to allow the incident beam to have minimal impedance before reaching the target material inside the cell, and any remaining photons to exit the cell. The cryogenic material was supplied to the cell through three gas manifold distribution tubes, equally spaced around the upstream end of the cell. These are supported by a ring. The LD_2 can then be supplied to the cell by JLab's on-site cryogenic storage facility.



Fig. 4.27 A rendering of the cryo-target used in g13. Taken from [86].

4.4.2 Data Corrections

Before the data obtained from g13 can be used for analysis, some corrections are implemented, which are listed here.

Photon energy correction

As discussed in Sec. 4.2.1, the energy of an incident photon, E_γ , is established by the energy of the coincident decelerated electron, E_e , as measured by the E-counters in the focal plane of the tagging system. However due to the weight and length of these counters, a mechanical sag was present in the set-up, which caused an incorrectly measured E_e and hence an incorrect E_γ . This was addressed by

CLAS collaborator, Mike Williams, using kinematic fitting to correct E_e [87]. The correction was implemented directly to the g13 dataset during "cooking" (the process of turning raw data containing detector information to reconstructed events for analysis).

Energy loss correction

As charged particles travel through a medium, energy is lost in the form of ionisations, which can be mathematically quantified as a mean energy loss per unit distance [88]. This means that when charged particles reach the DC, their measured momentum will be less than it was at their starting vertex, causing a discrepancy between the real and calculated associated 4-vector. Hall B collaborator Eugene Pasyuk developed the "eloss" package which applied a correction factor (in the order of MeV) to account for this energy loss, based on path length and stopping power, which is unique for each particle.

Momentum correction

Finally, momentum corrections are applied to account for drift chamber misalignments, as well as differences between the actual toroidal magnetic field and the calculated one used for track reconstruction [89, 90]. These corrections were also determined by kinematic fitting.

Chapter 5

Analysis

This chapter presents the procedure through which a new independent measurement of $C_{x'}$ is acquired from Jefferson Lab's CLAS g13a data (g13b is planned as a later addition, see Sec. 7.1). The analysis is divided into two major halves: Event selection (Sec. 5.2), in which the reaction of interest is isolated from all other events in the dataset; and the $C_{x'}$ extraction (Sec. 5.3). The analysis of statistical uncertainty, and some systematic effects, is also detailed.

The presented method by which $C_{x'}$ is extracted follows closely to Bashkanov *et al.* [1], an analysis which, as discussed in Sec. 3.2, benefited from a dedicated neutron polarimeter in its data acquisition. In order to apply this same method with CLAS, the Start Counter (described in Sec. 4.3.1) plays an equivalent role, relying on a neutron-proton charge exchange collision occurring inside the detector element. The angular distribution of the rescattered proton allows the polarisation of the neutron to be analysed. This is a novel technique which has not yet been formally utilised at Jefferson Lab. It opens up a plethora of many other potential analyses to be carried out with the CLAS detector (and CLAS12, as discussed later, in Chap. 7), which access higher photon energies than before, and enable a larger kinematic range than accessible using dedicated polarimeters.

5.1 The Reaction of Interest

The reaction of interest to be isolated and analysed is a two-step reaction. First, there is deuteron photo-disintegration ($\gamma d \rightarrow p_1 n$). From this, the product neutron undergoes a charge exchange collision, causing a scattered secondary proton ($np_2 \rightarrow p_2 n$). Fig. 5.1 shows this as a single diagram with important angles and vectors labelled, which will be defined mathematically in this section.

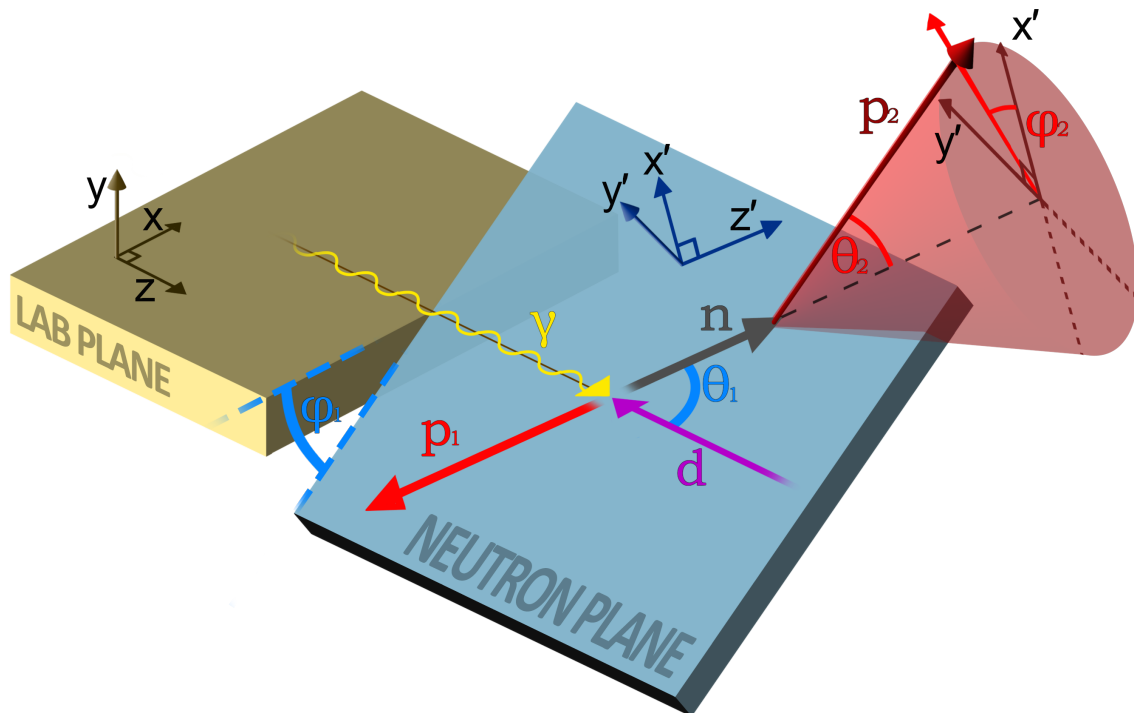


Fig. 5.1 A diagram depicting the two-step reaction of interest, $\gamma d p_2 \rightarrow n p_1 p_2$, in the centre of mass frame, and defining the angles between each plane. The third reaction plane is instead depicted as a cone to emphasize ϕ_2 , the statistical distribution of which allows a calculation of neutron polarisation.

5.1.1 Angle Definitions

There are three planes to consider in total; the lab plane and two reaction planes, with angles between each. The lab plane, xz , is defined as being parallel with the hall B floor, with \vec{z} aligned with the photon beam (γ). \vec{y} is then the normal to the lab plane. This gives unit vectors of $\hat{x} = [1,0,0]$, $\hat{y} = [0,1,0]$, and $\hat{z} = [0,0,1]$. The photon beam is incident on a target deuteron (d). Upon deuteron photo-disintegration, a neutron (n) and proton (p_1) are emitted diametrically opposite to each other in the centre-of-mass

frame. The neutron is the particle of interest, and so the polar angle, θ_1 , is defined as:

$$\theta_1 = \hat{z} \angle \vec{p}_n \quad \text{where} \quad \vec{A} \angle \vec{B} = \cos^{-1} \left(\frac{\vec{A} \cdot \vec{B}}{|\vec{A}| |\vec{B}|} \right) \quad (5.1)$$

Where \vec{p}_n is the momentum component of n . The angle swept out by θ_1 establishes a reaction plane, $x'z'$, where \vec{z}' is parallel with \vec{p}_n . Hence, the normal to this plane is given by $\vec{y}' = \hat{z} \times \vec{p}_n$. Therefore, the azimuthal angle between the lab plane and neutron plane can be defined as follows:

$$\phi_1 = \hat{y} \angle \vec{y}' = \hat{y} \angle (\hat{z} \times \vec{p}_n) \quad (5.2)$$

In the next step of the reaction, the neutron rescatters a secondary proton, p_2 , with the associated momentum vector given by \vec{p}_{p_2} . This polar scattering angle is given by:

$$\theta_2 = \vec{p}_n \angle \vec{p}_{p_2} \quad (5.3)$$

Similar to before, this angle being swept out establishes another reaction plane, $x''z''$, with a normal defined by $\vec{y}'' = \vec{p}_n \times \vec{p}_{p_2}$. Therefore the azimuthal angle between the neutron plane and the rescattered proton plane is given by:

$$\phi_2 = \vec{y}' \angle \vec{y}'' = (\hat{z} \times \vec{p}_n) \angle (\vec{p}_n \times \vec{p}_{p_2}) \quad (5.4)$$

With this, we have a method of obtaining ϕ_2 for each event, which requires a reconstruction of the vectors for γ , n and p_2 . It should be ensured that the angular range of azimuthal angles is -180° to 180° , and not simply the unsigned magnitude, which does not respect asymmetry. In general, one method to ensure this, given arbitrary plane normals, \vec{A} and \vec{B} , is to evaluate the z-component of their cross product, as shown below:

$$\phi_{AB} = \begin{cases} A \angle B & \text{if } (\vec{A} \times \vec{B})_z < 0 \\ -(A \angle B) & \text{if } (\vec{A} \times \vec{B})_z > 0 \end{cases} \quad (5.5)$$

5.2 Event Selection

In order to isolate events containing the reaction of interest from all events in g13a data-set, an algorithm must be created that omits/vetoes events from the analysis based on expected properties of the reaction. There are several steps to this data-reducing process, which are detailed and explained in this section. Each "cut" made to the data during this process is an attempt to minimise "background" (events not containing the reaction of interest) while preserving the "signal" (events containing the reaction of interest) of the data-set. However, no perfect cut exists, and so there is often a compromise between these two objectives. The order in which these cuts are implemented does not change the final selection. However, when investigating the effects of individual cuts, such as for step-wise signal/background ratio analysis (presented at the end of this section) or error propagation (not fully implemented in this analysis), it should be noted that one cut may overlap with or overshadow the next, making a subsequent data reduction appear to be less impactful.

5.2.1 Preliminary Skim

When the reaction of interest occurs in g13, we expect to detect two protons, and anything else can be filtered out. A preliminary algorithm was written and ran by Dr. Nicholas Zachariou [91] to filter through the entirety of g13a's data banks, apply the corrections described in Sec. 4.4.2, and store only relevant information into a new data tree, a process known as skimming. Only events with exactly two positive particles (no negative or neutrals) detected in the final state were kept when creating this data tree. This results in a little over 28 million events being stored for analysis. For the purposes of the next step, we can assume that these selected two positive particles per event are protons, however this will be further ensured in subsequent filter conditions.

5.2.2 Defining p_1 and p_2 Using DOCA

Once events with exactly two detected protons are selected, it's important to establish which proton is which between the proton emitted from deuteron photo-disintegration, p_1 , and the proton that was re-scattered by the neutron at the start counter paddle, p_2 . This distinction can be estimated by, for each event, comparing the distance of closest approach (DOCA) of each of the two protons with the photon.

In general, DOCA is a characteristic value of a pair of vectors in 3D space that pass by one another (i.e. they do not intersect or run parallel). The distance of closest approach is the shortest distance possible between these two vectors, and is defined by the separation of a pair of points/vertices, one on each vector, such that a line connecting these points would be perpendicular to both vectors. This can be expressed mathematically as follows:

$$\vec{v}_1 = \vec{u}_1 + t_1 \hat{u}_1 \quad \vec{v}_2 = \vec{u}_2 + t_2 \hat{u}_2 \quad \Delta\vec{v} = \vec{v}_1 - \vec{v}_2 \quad \Delta\vec{v} \cdot \hat{u}_1, \Delta\vec{v} \cdot \hat{u}_2 = 0 \quad (5.6)$$

These equations state that for any two points on a pair of respective lines in 3D space, each defined by a unit vector \hat{u} , scaled by a respective value of t , and displaced by a respective vector \vec{u} , the closest possible pair of points, \vec{v}_1 and \vec{v}_2 , is defined when the vector between them, $\Delta\vec{v}$, is perpendicular to both unit vectors \hat{u}_1 and \hat{u}_2 (i.e. the dot product between either of them is 0).

In the specific case of this analysis, the DOCAs between the photon (γ) vector, and either of the two protons (p_1 or p_2) are compared. From CLAS, we already know the direction (\hat{u}) and start vertex (\vec{u}) of each of these associated vectors, and so to calculate DOCA, we have to solve for t_1 or t_2 (solution provided in Appendix Sec. C.1). Because the incident photon that causes deuteron photo-disintegration was initially absorbed by the target deuteron, and the resulting proton vector originates from this deuteron, it should be expected that the DOCA between p_1 and γ is virtually 0 (meaning they intersect). However, due to uncertainties in CLAS particle track reconstruction, this DOCA will have a calculated value in the order of mm. On the other hand, p_2 is part of a different reaction vertex, originating in the start counter, which is separated from the target cell by ~ 10 cm. We can therefore expect the average DOCA between γ and p_2 to be larger than the average DOCA between γ and p_1 . This is visualised in Fig. 5.2.

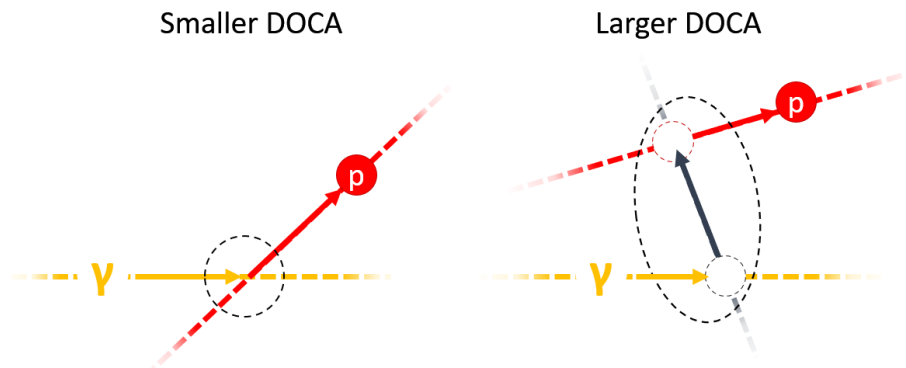


Fig. 5.2 A diagram to visualise the comparison between p_1 - γ DOCA (left) and p_2 - γ DOCA (right). The DOCA of p_2 - γ is on average larger due to the vertices being separated by an additional reaction step.

By default, CLAS particle banks will order protons by momentum, which has no preference or correlation with the reaction step. The identities of p_1 and p_2 are therefore initially mixed and unknown for each event. However, by comparing the DOCA to γ for each of the two protons on an event-wise basis, it can be estimated that p_1 is the smaller DOCA value proton, and p_2 is the larger. This is how p_1 and p_2 are defined in this analysis. By going over all events and comparing the DOCA distributions of what is now defined as p_1 and p_2 , it can be clearly seen that there are two separate distributions (shown in Fig. 5.3), whereas previously, the first and second proton (as ordered by momentum) had identical distributions.

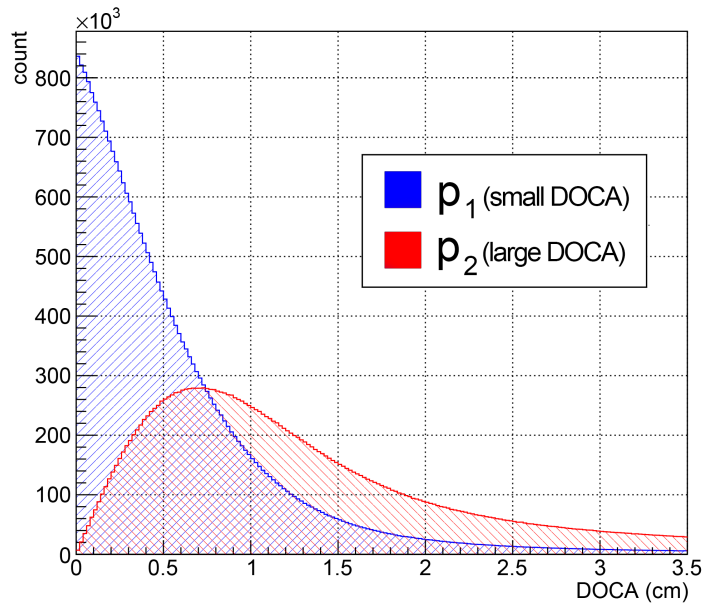


Fig. 5.3 A histogram of event-wise γp DOCA values for both p_1 (blue) and p_2 (red). There are two distinct distributions with expected characteristics, indicating the two types of protons are established well.

These distributions show the expected properties of p_1 and p_2 . The DOCA of p_1 peaks at 0 cm, with a spread caused by detector uncertainty. On the other hand, the mean value of p_2 DOCA is higher due to the physical separation of the reaction vertices. Also, the distribution of p_2 DOCA is much broader due to the additional variation introduced by an additional scattering angle, and less correlation with the photon.

Considering Δ DOCA

While this definition of p_1 and p_2 may be subject to some uncertainty, note that the overlapping region between these DOCA distributions does not necessarily indicate events where the assignment of p_1 and p_2 was uncertain. For example, a value of $p_1 = 0.5$ in this overlapping region could be paired with a value of $p_2 = 5$ in its respective event, in which case the distinction is clear. However, if $p_2 = 0.51$ in this hypothetical event, then there is much less certainty in which proton is which, as this is within the margin of error for detector reconstruction. Therefore, to better estimate uncertainty, it's more important to consider the difference between p_1 and p_2 DOCA values (or Δ DOCA) per event. This is visualised in Fig. 5.4, which shows a distribution of Δ DOCA values over all data.

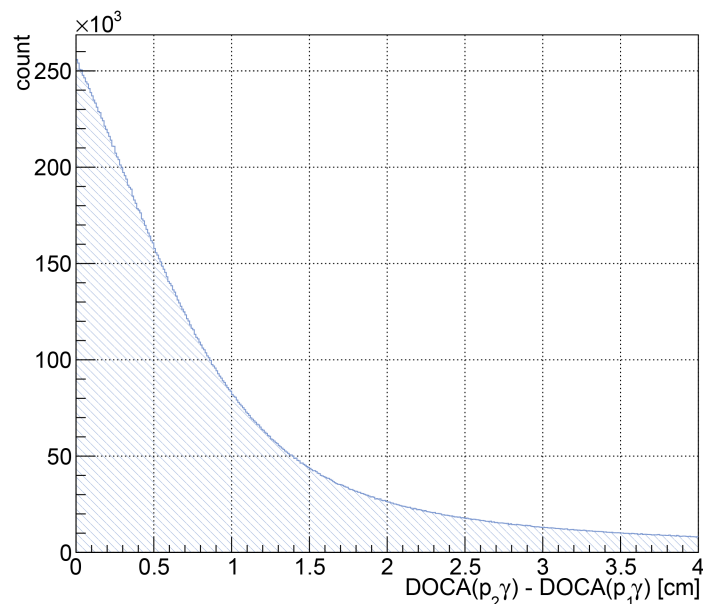


Fig. 5.4 A histogram of the difference between $p_1\gamma$ and $p_2\gamma$ DOCA values per event. The distribution shows a large amount of events have similar DOCA values, which increases the risk of p_1 and p_2 being incorrectly defined due to DOCA having limited precision.

Ideally, a Δ DOCA threshold would be a good cut to make to the data, as it would remove events with large uncertainty. However, as Fig. 5.4 shows, the data seems to peak at Δ DOCA = 0, and therefore any cut here would result in a large loss of data which statistically contains more good events than bad. Such a cut was trialled during analysis, and it was found that the loss of data was not worth the signal-to-noise ratio gained. It was ultimately decided to persist with a relatively less confident definition of p_1 and p_2 . Incorrectly defined protons will simply contribute to the background to be analysed and accounted for later.

p_1 vs p_2 in missing neutron mass

Uncertainties aside, the success of using DOCA to distinguish each proton is apparent if the missing mass of the neutron in deuteron photo-disintegration is considered for both p_1 and p_2 cases. Missing mass is a consideration of 4-momentum conservation (the concept of 4-momentum is derived in Appendix B). Because momentum is conserved, we can expect that the vector sum of reactant momenta minus the vector sum of product momenta is equal to a net momentum of 0. This relationship can be deliberately imbalanced by removing a product particle, replacing it with a placeholder "X", meaning the remaining net momentum will then equal the missing X momentum vector. The magnitude of X's momentum vector therefore captures the "missing mass" in this assumed reaction. This technique is useful for identifying undetected or "missing" particles based on an expected reaction in the dataset.

In this specific case, the reaction to consider is deuteron photo-disintegration, with an undetected product neutron. Hence, the missing neutron can be reconstructed by vector summing γ and d , then subtracting p ($\gamma d \rightarrow pX$) for each event. Assuming this reaction is present in the data sample, and the correct particle vectors are being used, then it should be expected that a histogram of the mass component of X peaks at the mass of a neutron. This neutron mass peak should only be visible when the proton resulting from deuteron photo-disintegration (p_1) is selected for the missing vector arithmetic. If instead, the rescattered SC proton (p_2) is selected, there would be an additional (and inconsistent) momentum imbalance, meaning no histogram peak associated with $\gamma d \rightarrow pn$. This provides a useful way to visualise the success of defining p_1 and p_2 . A histogram of both $MM^2(\gamma d \rightarrow p_1 X)$ and $MM^2(\gamma d \rightarrow p_2 X)$ are shown together in Fig. 5.5. As the figure shows, when using p_1 in place of p in $\gamma d \rightarrow pX$, there is a visible neutron mass peak corresponding to this reaction. Whereas the equivalent histogram for p_2 has no clear peak, only containing the background distribution, which indicates that p_2 did not come from this reaction. From this it can be seen that the current method of defining p_1 and p_2 is robust, and a good distinction has been made.

The histogram of $MM^2(\gamma d \rightarrow p_1 X)$ in Fig. 5.5 is also a visualisation of how much background compared to data of interest is present in the sample, as seen from the comparatively small peak of interest sitting on a "sea" of background. This same histogram is what is used to estimate signal to background ratio between data reduction steps, and will be revisited in Sec. 5.2.9.

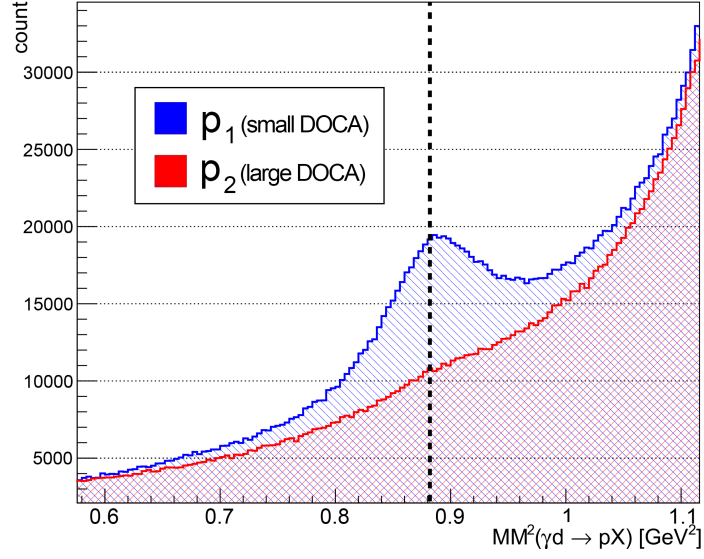


Fig. 5.5 Histograms of squared missing mass of $\gamma d \rightarrow pX$ over all events in the sample. Blue (red) shows the result when using p_1 (p_2) in place of the proton vector. The dashed line corresponds to neutron mass squared.

5.2.3 $\Delta\beta$ Selection

To further ensure that the selected positive particles are protons, a $\Delta\beta$ cut was implemented. β is a particle's speed expressed as a fraction of the speed of light, c . $\Delta\beta$ is the difference between a particle's β as measured by time of flight in the detector, and a β that can be calculated by assuming the particle's mass, using the following formula:

$$\beta_{calc} = \frac{p}{\sqrt{m^2 + p^2}} \quad (5.7)$$

Where p is momentum (established by drift chambers), and m is assumed mass, both using natural ($c = 1$) units of GeV. Assuming correctly identified particles, $\Delta\beta$ would idealistically be 0, however inaccuracies in the detector will cause a distribution of values centred on 0. In order to select this, a filter condition was implemented to only keep data within $\Delta\beta = \pm 0.015$, as shown in Fig. 5.6.

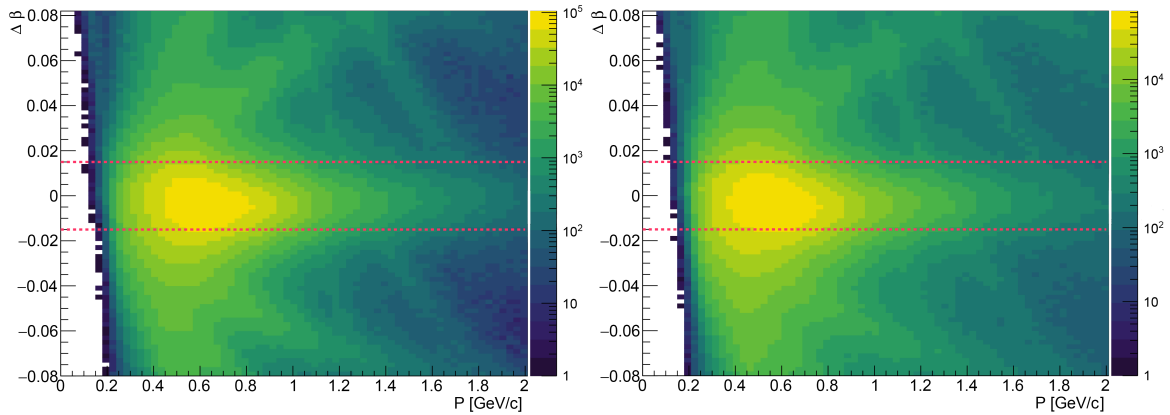


Fig. 5.6 Colour plots of $\Delta\beta$ vs momentum (p) for p_1 (left) and p_2 (right), with the colour Z-axis corresponding to the number of counts in a given bin. Dashed lines show the boundaries at ± 0.015 for selecting the proton region. Other particle species are visible as adjacent streaks.

5.2.4 Photon Coincidence Time

As covered in Chap. 4, the electron beam from CEBAF arrives in bursts every 2.004 ns. The current of the beam is tuned so that only one photon per bunch can be associated with any subsequent event. However, some events may contain multiple candidate photons due to the short time between bursts. This can be visualised with a histogram of time differences (Δt) or *coincidence times*, between p_1 and any candidate photons across all events. This is shown in Fig. 5.7. The high timing resolution allows us to see that, while most candidate photons belong to the correct beam pulse, there are sometimes candidate photons belonging to preceding or proceeding bunches. The correct photon is easily assigned by selecting the one with the smallest coincidence time with p_1 for each event, which again, is possible thanks to the precise timing resolution. As a further filter condition, only events with photon coincidence times under 1 ns with both p_1 and p_2 were selected before continuing. This selection is shown in Fig. 5.8.

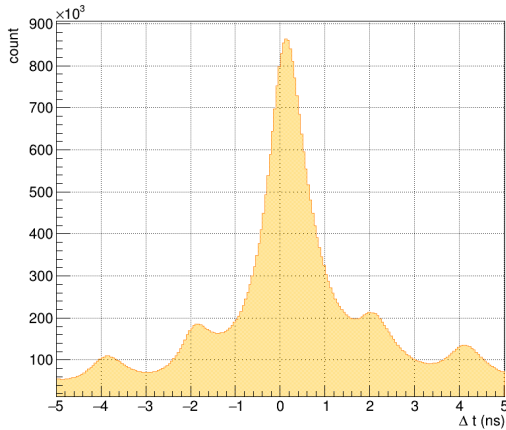


Fig. 5.7 Histogram showing the time difference in nanoseconds between p_1 's start time, and the start time of every photon in an event, over all events. Additional smaller peaks at 2 ns intervals indicate photons belonging to a different beam bunch.

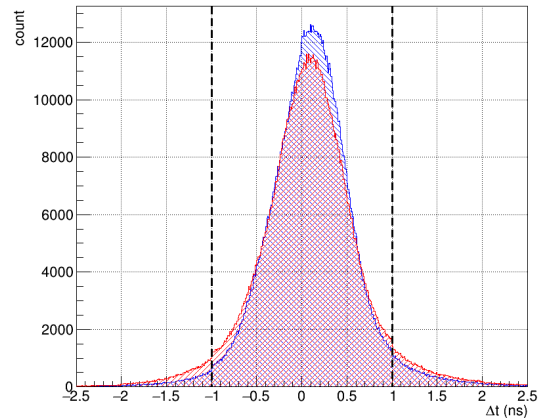


Fig. 5.8 Coincidence time between the associated photon and both p_1 (blue) and p_2 (red) per event. Dashed lines at ± 1 ns show the data selection region.

5.2.5 POCA Z-vertex Selection

Similar to the DOCA (*distance* of closest approach) as previously discussed in Sec. 5.2.2, the POCA (*position* of closest approach) is the 3D coordinate (or vertex) at the midpoint between where two vectors come their closest, and therefore the midpoint of the associated DOCA vector. The POCA is useful in estimating the reaction vertex, i.e. the exact location of an interaction/decay. If we consider the POCA between γ and p_1 , we should expect to see POCAs that are inside the region of the target LD_2 . However, due to the presence of other materials which make up the target cell (see Sec. 4.4.1), we find that there is, in addition, an abundance of POCAs indicating that reactions originated in surrounding locations, such as the plastic walls of the target cell container, and the window of the target apparatus. This is visible in a histogram of the Z-component of $p_1\gamma$ POCA values (Fig. 5.9). To remove these events, a selection is made on the POCA Z-component to only include events occurring inside the target length.

No cuts were applied with respect to the X and Y components of POCA, as the track reconstruction isn't accurate enough to get a clear picture of the target in the XY-plane, therefore any cuts made would greatly risk losing signal. However, the target walls are thin enough that their effect should be negligible.

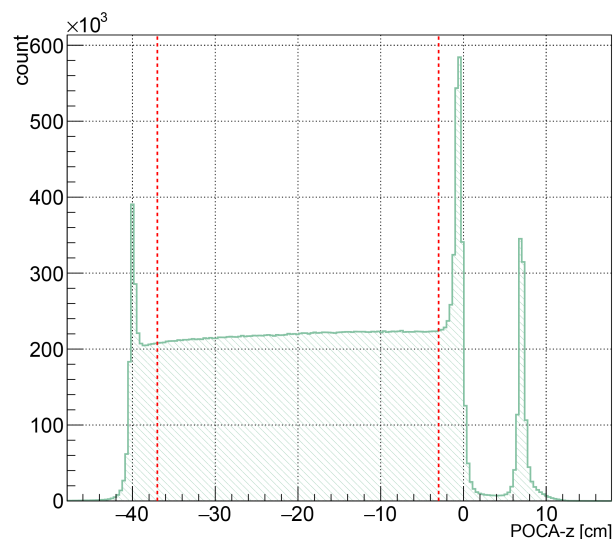


Fig. 5.9 A histogram of values for the Z component of the POCA between p_1 and γ , which indicates where reactions took place along the Z-axis of the 40 cm length target. A selection is made to only keep values at 3 cm to 37 cm, which removes peaks corresponding to the target windows.

5.2.6 Diametric SC Paddle Restriction

In deuteron photo-disintegration, the produced proton and neutron are emitted diametrically opposite to each other in the centre-of-mass frame. It should therefore be expected that in our reaction, these nucleons are detected at opposite sides of the start counter. As detailed in Sec. 4.3.1, there are 24 start counter paddles encircling the target which are numbered as such in a clockwise order (when facing downstream of the beam line). Note that the paddle hit by the neutron can be inferred from the start vertex of p_2 . Therefore, for every event, there is an associated paddle for each p_1 and p_2 . It should of course be expected that this same diametric geometry is also visible in the ϕ angles of associated nucleon vectors. However, particle tracks are calculated in CLAS reconstruction using information from the drift chamber (track curvature due to torus field), which is absent for the neutron, and will provide an incorrect ϕ for p_2 , due to the displaced vertex origin. We instead rely on the SC paddle hits. To specify pairs of opposing paddles, the absolute value of difference between both paddle numbers in an event pair should be 12, and this can be used as another restriction on the data. This restriction is relaxed further upon implementation by also allowing values of 11 and 13 as shown in Fig. 5.10.

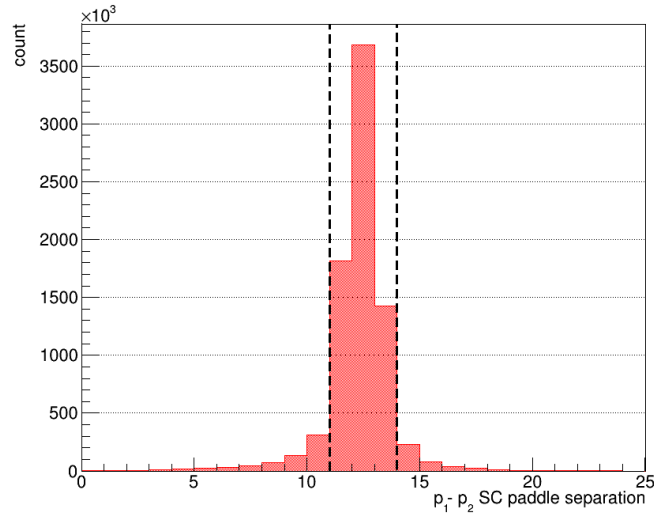


Fig. 5.10 Histogram of the absolute value of the difference between paddle numbers corresponding to detections of p_1 and p_2 . The peak at 12 indicates the majority of events contain diametrically opposite paddles. Dashed lines show data selection boundaries, containing only paddle separations of 11 to 13.

5.2.7 Missing Pion Mass Cut

Pion production events commonly occur in g13, and have a significant contribution to background in the data sample, due to undetected reaction components leading to an apparent exclusive 2-proton event. To address this, a missing mass cut is applied. Earlier in this section, missing mass was considered in terms of the reaction of interest. However in data reduction, it is often useful to consider missing mass in the context of other (background) reactions that may be taking place.

Consider the reaction, $\gamma + d \rightarrow p + p + \pi^-$. It's possible (and common) for this reaction to occur with the π^- going undetected by CLAS. This causes it to be incorrectly selected as an event of interest, given the current filter conditions. The high likelihood of pion events results in a strong peak in a histogram of $MM^2(\gamma d \rightarrow ppX)$, centred on the mass of π , shown in Fig. 5.11. To remove this background, a cut is made to discard any event where $MM^2(\gamma d \rightarrow ppX) > 0 \text{ GeV}^2$, effectively removing the large peak. Before this cut, the vast majority of events sit in this peak region. Therefore this step represents a very large data reduction. Despite this, the effect of this cut is not visible in the upcoming data reduction overview of Sec. 5.2.9, due to this pion mass peak occurring largely outside the region of interest defined in the next subsection.

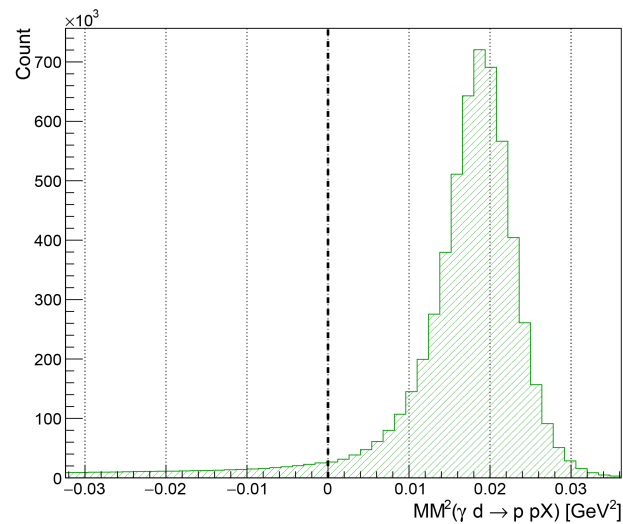


Fig. 5.11 A histogram of $MM^2(\gamma d \rightarrow p_1 p_2 X)$, which captures pion production events occurring in the selected data. The dashed line at 0 GeV represents the cut-off used to remove these events.

5.2.8 Final 2D missing mass selection

The reaction of interest within the remaining dataset can be visualised using a 2D histogram, which shows where two independent measurements of missing neutron mass agree with each other (Fig. 5.12).

The first missing mass equation, $\gamma d \rightarrow p_1 X$, has already been discussed earlier in this section - it simply considers the initial deuteron photo-disintegration reaction. The second missing mass equation to be utilised is $\gamma d p \rightarrow p_1 p_2 X$. This considers, in addition, the re-scattered proton, p_2 , as part of the reaction, with the inclusion of an at-rest proton as a reactant, and the detected p_2 as a product.

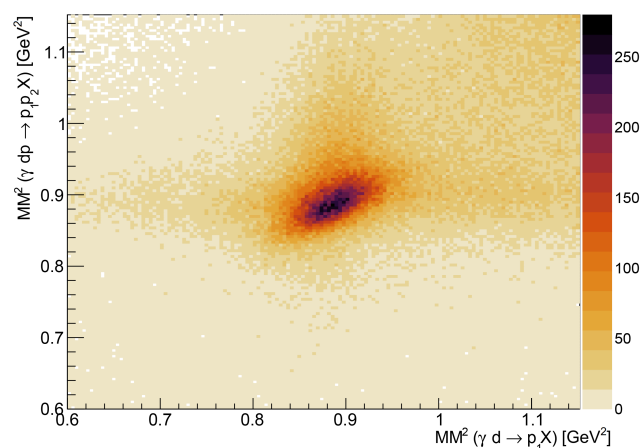


Fig. 5.12 A 2D colour histogram showing where two different measurements of missing neutron mass agree with each other through all events in the reduced sample, creating a clear spot corresponding to the reaction of interest.

In order to select the region of interest, the peak region is defined with a box selection on this 2D missing mass histogram. This is done in two steps. First, a projection of the Y-axis is taken to create a 1D histogram of $MM^2(\gamma dp \rightarrow p_1 p_2 X)$. This is fitted with a two-part function: a Gaussian function (to capture the peak) summed with a third-order polynomial function (to capture the background). The fit is achieved with a χ^2 minimisation algorithm. Using the standard deviation (σ) of the Gaussian component of this summed function, a region of $\pm 2\sigma$ is defined, centred on the Gaussian mean (μ). Events outside this region are omitted. This effectively defines the "height" of the 2D box being created on the region of interest.

Next, a projection of the X-axis is created using the remaining data, resulting in a background-reduced histogram of $MM^2(\gamma d \rightarrow p_1 X)$, which is once again fitted using the same technique, defining a selection region of $\pm 2\sigma$ based on a new function's Gaussian component. This is now the "width" of the 2D box. Both these missing mass fits are shown in Fig. 5.13.

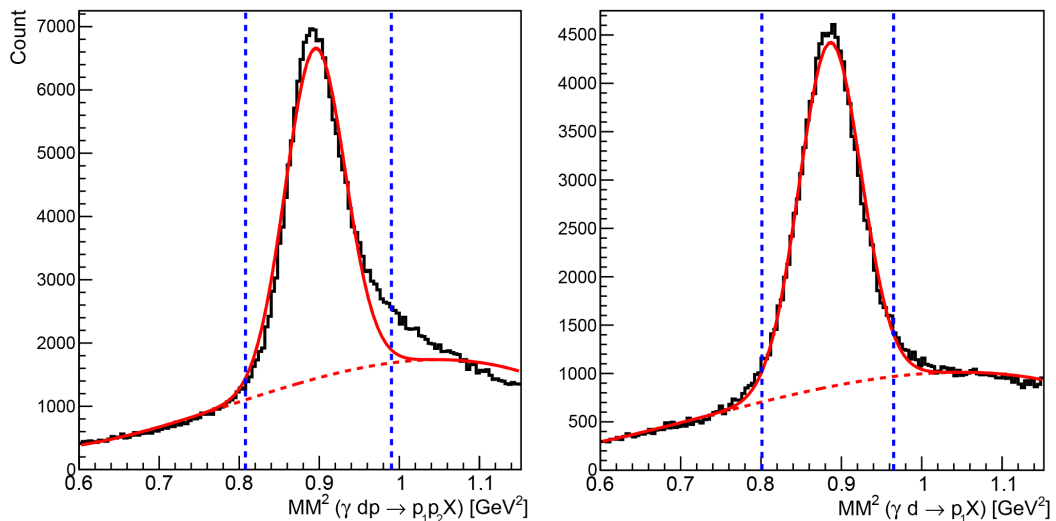


Fig. 5.13 The final two steps of data selection, involving fitting a summed Gaussian and third-order polynomial functions (red) to missing mass histograms (black). A function is first fit to $MM^2(\gamma dp \rightarrow p_1 p_2 X)$ (left). The selected data is then passed into a histogram of $MM^2(\gamma d \rightarrow p_1 X)$ (right) which is once again fitted with the same function. Blue dashed lines show the selection region, defined by $\pm 2\sigma$ of the Gaussian.

With this final cut, the event selection and background reduction process is complete, yielding around 10^5 events. However there are a couple of final steps required to be fully prepared for analysis:

Signal to background ratio

First, the relative areas under the component fit functions are important; they give the fraction of data belonging to either signal or background, parameters that will be later used when considering the background's contribution to the result. In order to measure this, the $\pm 2\sigma$ region of interest is used as limits to find the integral of both the histogram and the polynomial component of the $MM^2(\gamma d \rightarrow p_1 X)$ fit. The area of background is given by the definite integral of the polynomial, as shown below in Eq. (5.8):

$$\text{Area}_{pol} = \int_{\mu-2\sigma}^{\mu+2\sigma} P(MM^2) d(MM^2) \quad (5.8)$$

Where $P(MM^2)$ represents the third-order polynomial component of the summed function fitted to the $MM^2(\gamma d \rightarrow p_1 X)$ histogram. The integral limits are defined by the Gaussian component, as previously discussed in this subsection. The area of signal is this value subtracted from the total area of the histogram ($\text{Area}_{hist} - \text{Area}_{pol}$), the method of calculating which is shown below in Eq. (5.9):

$$\text{Area}_{hist} = \sum_{i=(\mu-2\sigma)}^{(\mu+2\sigma)} N_i \times \Delta x \quad (5.9)$$

This is the total number of events, N , in each bin within the same limits as before, multiplied by the bin width, Δx . Calculating the signal area in this way is more accurate than simply taking an integral of the Gaussian, as the polynomial achieves a better fit within the region of interest, and the histogram area does not require any fitting. Following this method, the region of interest is measured to be 71.4% signal and 28.6% background. The statistical error in each of these areas will be later considered in Sec. 5.3.10, and detailed in Appendix Sec. C.2.2.

Background selection

Another necessary piece of information to later consider in contributions from background is a sample of pure background. To this end, all data at more than 3σ from either side of the mean of the Gaussian fit to $MM^2(\gamma d \rightarrow p_1 X)$ is selected as the background sample, which is a safe distance from the influence of the signal. This is known as the sideband region. Ideally, samples from either side of the peak would be taken in case of variation. However, this method is a compromise for low statistics.

Other 2D selection processes

Because the region of interest seen in Fig. 5.12 seems to be an angled oval, other methods of extracting its shape were trialled before settling on the method described in this section. One alternative method included defining a rotated ellipsoid with adjustable parameters, including the semi-minor and semi-major axes, XY displacement, and rotation. These parameters could be manually adjusted to acquire a good looking fit over the region of interest, however, it was preferred to have a reliable and repeatable minimisation algorithm, rather than a manual process. Another method used multiple 2D Gaussian functions to capture the shape of the region using χ^2 minimisation, however this quickly became too complicated, as the number of Gaussian functions (including rotated Gaussians) required to capture both the peak and background was much higher than first thought, and ultimately, no neat fit could be established.

5.2.9 Data reduction summary

This section gives an overview of each step in the data reduction process and gives an idea of their effect by analysing the remaining data between each cut. Using the same 2D missing mass selection procedure as before, a region of interest (ROI) is fitted to the data between each cut (see Fig. 5.14). Like before, the ROI is defined as being within $\pm 2\sigma$ of the Gaussian component of the fit, while the third order polynomial captures the background. The integral of the histograms within their respective ROI gives an estimate of the number of events remaining in the sample, while the relative integrals of the component functions allow for an estimate of the signal ratio – the ratio of events which contain the reaction of interest against all events in the sample. Table 5.1 shows these calculations made after each cut. This analysis makes it easy to see if cuts are having a good effect at increasing the signal ratio, and which cause the largest losses of data. It was through this procedure that a potential Δ DOCA cut, discussed at the end of Sec. 5.2.2, was seen fit to be omitted, as the small increase in signal ratio was not worth the substantial loss of data.

Table 5.1 A summary of each data reduction step, with an overview of impact on data by each.

Step number	Summary	Subsequent event count in ROI	Signal ratio
1 ●	Preliminary skim	6.21×10^5	0.421
2 ●	$\Delta\beta$ within ± 0.15	2.33×10^5	0.541
3	Δt within 1 ns	2.33×10^5	0.541
4 ●	γ - p_1 POCA $_z$ within -37 to -3 cm	1.74×10^5	0.657
5 ●	Δ SC paddle within 11 to 13	1.12×10^5	0.715
6	$MM^2(\gamma d \rightarrow ppX) < 0$ GeV	1.15×10^5	0.712

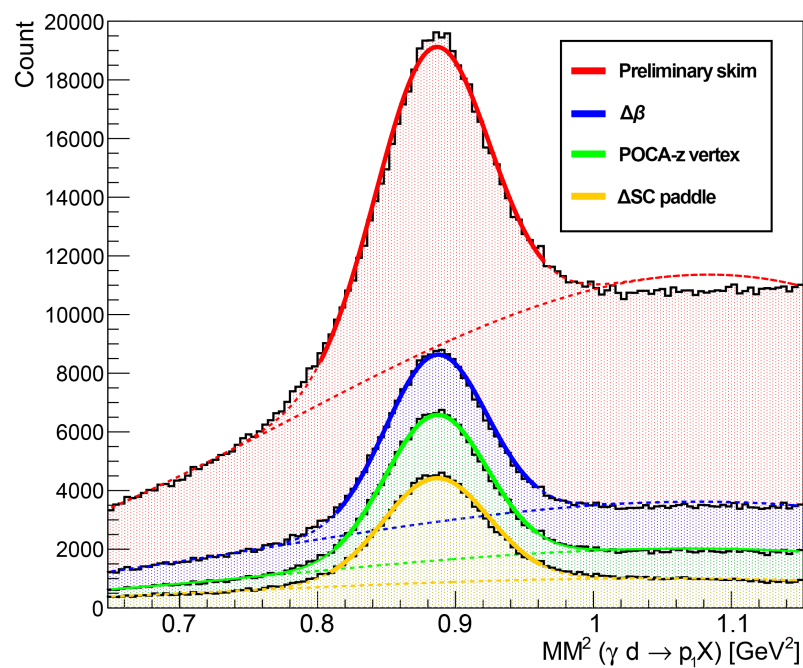


Fig. 5.14 Multiple histograms (black) showing the remaining data between each reduction step, as well as compound functions (each a summed Gaussian and third order polynomial) fitted to each histogram. Solid coloured lines depict the $\pm 2\sigma$ region of interest (ROI) defined by each fit. Dashed lines show polynomial components of each fit, which estimates background. Cuts which make a negligible effect in the ROI are not shown.

5.3 $C_{x'}$ extraction

To briefly recap, in order to acquire an original measurement of neutron $C_{x'}$ from JLab's g13 data, a method that follows closely to Ref. [1] (discussed in Sec. 3.2) is used. This is a maximum likelihood estimate (MLE) of a parameterised $C_{x'}$, as it appears in the spin-dependent cross-section equation, Eq. (2.2), from Ref. [22], which is now further simplified by considering a secondary reaction vertex, which substitutes neutron polarisation, p_y^N , circumventing the need to measure it directly. This is possible because the recoil neutron polarisation from deuteron photo-disintegration ($\gamma d \rightarrow p_1 n$) can be analysed through a charge exchange scattering reaction ($np_2 \rightarrow p_2 n$). From this, the angular distribution of the rescattered proton determines the neutron polarisation, as well-modelled by partial wave analysis. This leads to the following spin-dependent differential cross-section equation:

$$\frac{d\sigma}{d\Omega} = \left(\frac{d\sigma}{d\Omega} \right)_0 [1 + A_y(\theta_{sc})(P_y \cos \phi_{sc} + C_{x'} P_\gamma^\odot \sin \phi_{sc})] \quad (5.10)$$

Where $\left(\frac{d\sigma}{d\Omega} \right)_0$ is the unpolarised cross section, $A_y(\theta_{sc})$ is the analysing power of the charge exchange reaction as a function of θ_{sc} (to be shown in the next subsection). θ_{sc} and ϕ_{sc} are the equivalent of θ_2 and ϕ_2 from Sec. 5.1.1. They are the respective polar and azimuthal scattering angles of the recoil proton (p_2). P_γ^\odot is the circular polarisation of the photon beam, which is calculated using the Olsen-Maximon formula (Eq. (4.2)). Finally, P_y and $C_{x'}$ are the polarisation observables of the neutron, representing induced recoil polarisation (along y'), and transferred beam-recoil polarisation (along x'), respectively.

Regarding $C_{z'}$

Just like in the analysis of M. Bashkanov *et al.*, discussed in Sec. 3.2, the observable, $C_{z'}$, which was present in Eq. (2.2), has not been carried into the final cross section equation, Eq. (5.10). As introduced in Sec. 2.1, $C_{x'}$ quantifies the transferred polarisation along x' (*transverse* polarisation), whereas $C_{z'}$ quantifies the transferred polarisation along z' (*longitudinal* polarisation). Refer to Fig. 5.1 for the visualisation of these axes. Analysing neutron polarisation via the angular distribution of p in $np \rightarrow pn$ is only able to reveal transverse polarisation. Longitudinal polarisation does not produce any left-right asymmetry, and therefore this analysis has no sensitivity to it. $C_{z'}$ is therefore always equal to 0 in this analysis, and is neglected from the final cross-section equation.

Regarding P_y

While the observable P_y is part of Eq. (5.10), it is ultimately not the focus of this analysis and will instead be fixed at zero. It will be later demonstrated that this does not greatly influence the result. As covered in Chap. 3, $C_{x'}$ has only had one experimentally-acquired published measurement to date, and so its measurement is more crucial for the motivations described in Chap. 2. But more importantly, measuring P_y in this analysis is less feasible due to unquantified systematic uncertainties created by detector acceptance effects. To explain this, it should first be understood that the detector system described in Chap. 4 is not homogenous. Its sensitivity varies across its angular range, and therefore will vary across θ_{sc} . This variance would affect the apparent value of P_y , which, as seen in Eq. (5.10), is an amplitude of the term $A_y(\theta_{sc}) \cdot \cos \phi_{sc}$. On the other hand, $C_{x'}$ is not changed by these acceptance effects because it is an amplitude of the term $A_y(\theta_{sc}) \cdot P_\gamma^\odot \cdot \sin \phi_{sc}$. This contains the circular photon polarisation term, P_γ^\odot . As mentioned in Sec. 4.4, the photon beam's helicity was frequently flipped during g13a, and hence the sign of P_γ^\odot frequently changes in the data. This means that, for the $C_{x'}$ term, any variation in ϕ acceptance averages out to a flat ϕ distribution after being summed over all events. In order to acquire an unbiased P_y measurement, the systematic effects of the detector must be quantified using dedicated studies that measure the detector acceptance with high certainty. This is a very involved process that includes realistic event simulation. This is possible, and a necessity for differential cross sections, however this was ultimately not the focus of this analysis.

5.3.1 Analysing Power A_y

Because the charge exchange reaction ($np \rightarrow pn$) is well understood and known to a high precision [92], values of analysing power (A_y) are assigned on an event-by-event basis using a partial wave analysis model from the SAID (Scattering Analysis Interactive Dial-in facility) repository [93]. This model, shown in Fig. 5.15, relates a value of analysing power to the incident neutron's kinetic energy (KE_N), and the polar scattering angle of the recoil proton (θ_{sc}).

As Fig. 5.15 shows, both positive and negative values of A_y are possible. This presents a potential problem to the analysis. A_y 's role in Eq. (5.10) is one that scales the influence of the polarisation observable on the cross section of the reaction. Eq. (5.10) will be summed over all events to gradually build up a picture of the cross section. However, if both positive and negative values of A_y are included, destructive interference will occur, and the overall effect of the polarisation observables will

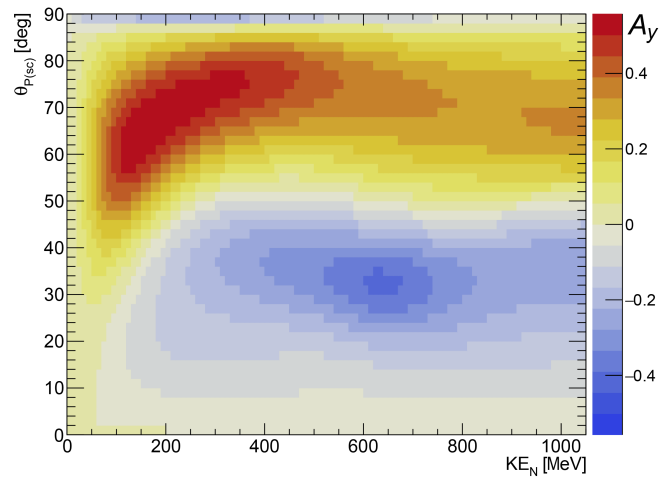


Fig. 5.15 A 2D surface of analysing power (A_y) values, taken from a well-established SAID partial wave analysis model of the $p(n, p)n$ reaction. This maps a measurement of proton scattering angle (θ_{Psc}) and Neutron kinetic energy (KE_N) to a value of analysing power.

be lessened, making it more difficult for an algorithm to extract the features of their influence. For better $C_{x'}$ definition, only positive or only negative values of A_y should be used for analysis. But first, it should be considered how this would reduce the data. Fig. 5.16 shows how the current dataset is distributed between positive and negative values of A_y . Overwhelmingly, the data sits on the negative side. Therefore, all events which yield a positive A_y are discarded. This can therefore be thought of as another data reduction step, which further reduces the dataset from 1.15×10^5 to 9.91×10^4 (73.2% signal). Ideally, both positive and negative A_y datasets would be analysed separately, however, the $+A_y$ dataset is currently too small for a precise analysis, and is left as future work.

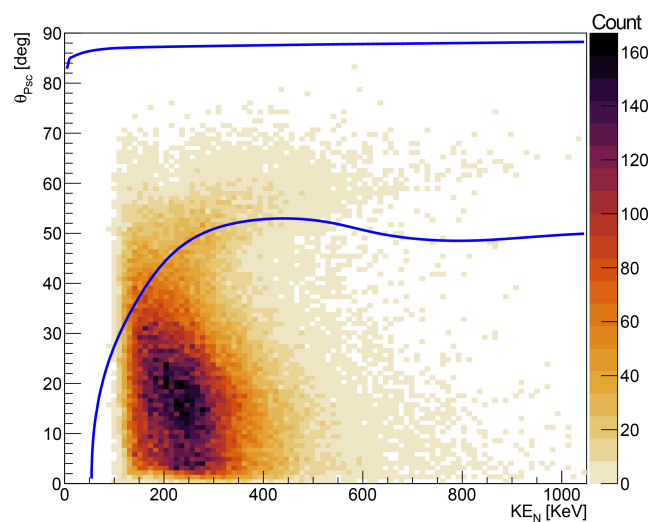


Fig. 5.16 A histogram showing how the current dataset is distributed among proton scattering angles, θ_{Psc} , and Neutron kinetic energy, KE_N . The blue line shows the contour corresponding to $A_y = 0$.

5.3.2 Maximum Likelihood Introduction

The chosen method of observable extraction is from a consideration of statistics, which is a major limit of this analysis. While maximum likelihood estimation (MLE) still requires high numbers of events for the results to be robust, there is no averaging as with conventional binning methods, which results in biasing when statistics are low [20]. In general, MLE is a technique used to find the value of unknown parameters in a statistical model which best fits given data. Suppose we have a probability distribution function, $f(x)$, with an unknown, parameterised variable, θ . Values of x which are expected to fit this distribution are collected, building up a histogram of n entries. For a given trialled value of θ , a calculation of likelihood, L , is given by taking the product of all solutions to $f(x_i)$, over all i values of x . This is represented mathematically below:

$$L(\theta) = \prod_{i=1}^n f(x_i | \theta) \quad (5.11)$$

For a range of θ values, this defines a likelihood function, $L(\theta)$, the maximum value of which indicates the most likely value of θ . Maximum likelihood is therefore found at a local maxima where the gradient of $L(\theta)$ is 0. It is usually more mathematically convenient to take the logarithm of Eq. (5.11) in order for likelihood to be calculated as a sum, as shown in Eq. (5.12). This is commonly referred to as maximum log-likelihood.

$$\log L(\theta) = \sum_{i=1}^n \log f(x_i | \theta) \quad (5.12)$$

The maxima of a likelihood and its equivalent log-likelihood functions are identical, because $dL/d\theta$ and $d\log L/d\theta$ both equal 0 at the same value of θ .

5.3.3 Minimum Log-likelihood Formula

Returning now to the analysis, we have a probability distribution function in the form of a cross-section equation (Eq. (5.10)), with unknown parameters P_y and C_x , that we want to fit to the data. The first step is to create the log-likelihood formula. This is given below:

$$\log[L] = \sum_{i=1}^n -2 \log[1 + A_y(\theta_{sci})(P_y \cos \phi_{sci} - C_x P_y^\ominus \sin \phi_{sci})] \quad (5.13)$$

To complete this sum, all events in the sample must be iterated through. The i subscripts represent variables which are unique for each event. A negative sign is added to invert the log-likelihood function. This means the optimal value of likelihood is found at the minimum instead of the maximum, which allows the value to be extracted by a χ^2 minimising algorithm. Finally, a factor of 2 is added so that the uncertainty measurement in the likelihood estimate is kept consistent with the uncertainty measurement in χ^2 minimisation.

5.3.4 Parameterisation

Polarisation observables vary with the kinematics of their associated reaction. Extracting a single value for $C_{x'}$ from the data by leaving it as a single parameter would therefore be an almost meaningless result, with large uncertainty. The extraction of $C_{x'}$ should instead respect photon energy, E_γ , and neutron polar scattering angle, θ_N . One method of achieving this is to extract a unique $C_{x'}$ value for data in bins of E_γ and θ_N . This method was investigated first, however, dividing the already heavily reduced dataset into a grid of bins creates large uncertainties. Instead, $C_{x'}$ is parameterised as a many-parameter function that depends on E_γ and θ_N . This will ultimately result in the final extraction of $C_{x'}$ values being in the form of a 2D surface of values on a map of E_γ vs θ_N . The chosen $C_{x'}$ function must offer full, continuous freedom for $C_{x'}$ values in the full optimal range of E_γ and θ_N . The chosen range to focus on is 0.4 to 1.1 GeV in E_γ and the full range of θ_N . This was chosen to encapsulate the current data, shown in Fig. 5.17. Based on this distribution a diminishing confidence should be expected as E_γ increases in this range, and also at forward/backward θ_N angles.

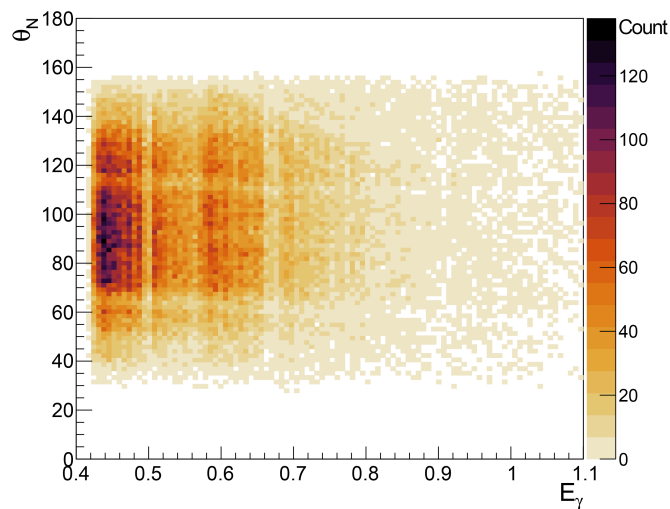


Fig. 5.17 A 2D histogram of E_γ vs θ_N over all 9.91×10^4 selected events.

The full parameterisation of $C_{x'}$ per event is given below:

$$C_{x'} = L_0(-\sin \theta_N) + L_1(-3 \cos \theta_N \sin \theta_N) + L_2(-1.5(5 \cos \theta_N^2 - 1)) \\ + L_3(-2.5(7 \cos \theta_N^3)) - 3 \cos \theta_N \sin \theta_N \quad (5.14)$$

$$\text{Where } L_j = -2 + \sum_{i=1}^{G_n} P_{(i+jG_n)} e^{-\frac{(E_\gamma-b)^2}{2\sigma^2}} \quad (5.15)$$

The equation's variation across θ_N (Eq. (5.14)) is based on the energy dependencies of the first 3 associated Legendre functions of the first order [94], acquired from [95]. For the variation across E_γ (Eq. (5.15)), each L_j amplitude parameter is further parameterised as a sum of G_n Gaussian functions with means at regular intervals of E_γ . The amplitude of each Gaussian is determined by a unique parameter, P . Consequently, $C_{x'}$ is parameterised by a total of $4 \times G_n$ parameters. Setting a value for G_n allows a control of the number of parameters across E_γ . For the analysis presented within this thesis, G_n is always equal to 8. This was chosen as a balance between giving $C_{x'}$ enough freedom while also ensuring the function can converge in the subsequent minimisation. For each Gaussian function, the standard deviation, σ , is fixed relative to G_n such that each Gaussian is spaced by 2σ , and covers the full 0.4-1.1 GeV range. b , the displacement, can be thought of as 0 for now, but will be discussed more in Sec. 5.3.9. Finally, each Gaussian sum is offset by -2 to ensure that each extracted parameter is a positive value. As mentioned, this analysis does not focus on P_y . Instead of parameterising P_y , it is fixed at zero, and considered a systematic uncertainty. It will be later shown in Sec. 5.3.8 that the range of possible P_y values is negligible on the final result.

5.3.5 Minimisation

An algorithm is implemented to iterate through all selected events and sum each according to the maximum likelihood equation, Eq. (5.12), with P_y fixed at zero, and $C_{x'}$ parameterised as described in the previous subsection. A χ^2 minimisation algorithm is then implemented on this summed function, eventually converging on optimal values for each of the 32 $C_{x'}$ parameters as defined in Eq. (5.14) and Eq. (5.15), giving an optimal solution for $C_{x'}$ as a function of E_γ and θ_N . This allows $C_{x'}$ to be presented as a surface of maximum likelihood $C_{x'}$ values across E_γ and θ_N , shown in Fig. 5.18.

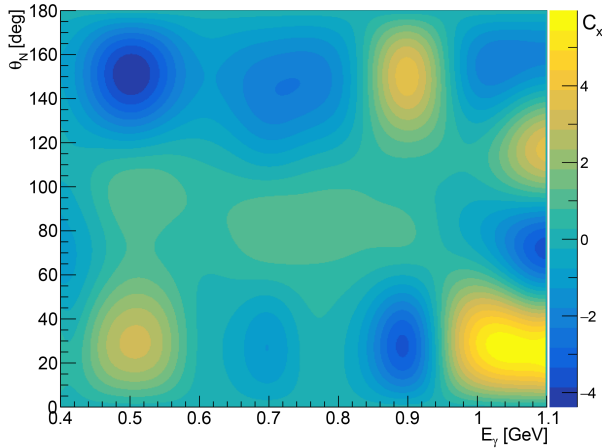


Fig. 5.18 A 2D surface of $C_{x'}$ values across E_γ and θ_N , extracted using a maximum likelihood technique on all selected data. Peaks and troughs of extreme, non-physical values are a result of regions of low statistics.

This first extraction shows sensible values of $C_{x'}$ (around 1) in the region of $E_\gamma = 0.5\text{-}0.9$ GeV, $\theta_N = 60^\circ\text{-}110^\circ$. However, regions corresponding to low statistics have wildly varying values which exceed the physical limits of ± 1 . The peaks and troughs follow the regular intervals of Gaussian spacing, suggesting a bias is being introduced by the effective nodes and anti-nodes. Both of these aspects will be later addressed by an unbiased measure of statistical uncertainty, which is left until the final step. To increase readability, focus on higher statistic regions, and later make valid comparisons, it is preferred to take fixed θ_N values of this 2D surface, and present a 1D function of $C_{x'}$ against E_γ as shown in Fig. 5.19. As this method of presentation allows multiple solutions to be overlaid together, it is also shown in Fig. 5.19 how the $C_{x'}$ extraction varies with P_y . The relatively small variation shows the extent of the systematic uncertainty introduced by P_y . It will be explored more in Sec. 5.3.8 how this affects the final result.

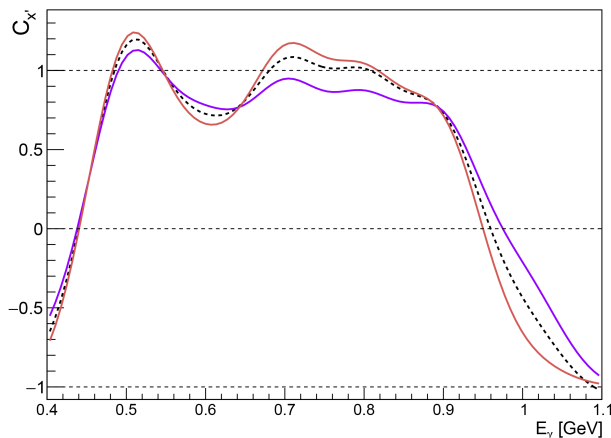


Fig. 5.19 The extracted $C_{x'}$ function of E_γ at $\theta_N = 90^\circ$. Dashed horizontal lines at ± 1 show physical limits. To show the influence of P_y , the same function is shown for $P_y = 0$ (dashed black), 1 (red) and -1 (purple)

5.3.6 Background $C_{x'}$ Measurement

The previously displayed extraction of $C_{x'}$ is found using all data in the region of interest, defined in Sec. 5.2.8. However, as discussed, this region of interest is estimated to be only 73.2% signal. The extraction of $C_{x'}$ is therefore being diluted by the 26.8% background, in a relationship which can be described as follows:

$$\text{Measured } C_{x'} = (0.732 \times \text{Signal } C_{x'}) + (0.268 \times \text{Background } C_{x'}) \quad (5.16)$$

If the background was considered $C_{x',BG} = 0$, as one might naively expect, then the solution would be to simply divide the result by 0.732 (the dilution factor). But as shown by Fig. 5.20 and Fig. 5.21, an extraction of $C_{x'}$ from the background sample yields non-zero results. This could be the result of underlying physics, or non-physical values arising from statistical or systematic uncertainty. Regardless, this background measurement will be used for subsequent sideband subtraction. A later section (Sec. 5.3.11) will explore an assumption of $C_{x',BG} = 0$.

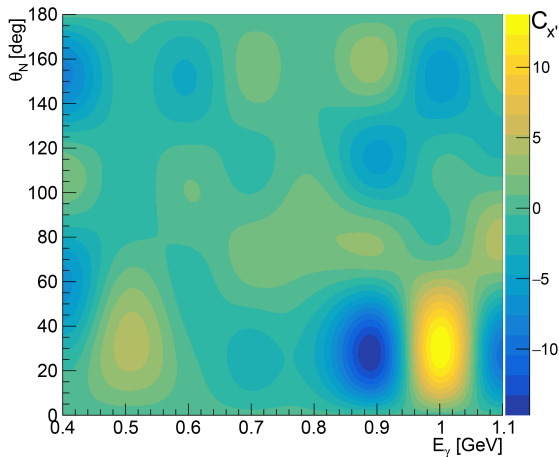


Fig. 5.20 A 2D surface of $C_{x'}$ values across E_γ and θ_N as measured in the background sample. These values will be used in sideband subtraction.

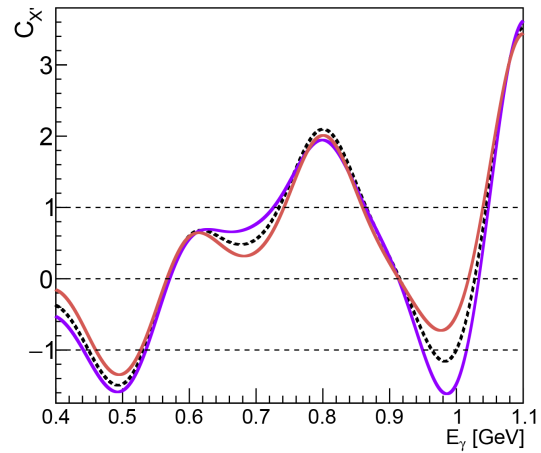


Fig. 5.21 Background $C_{x'}$ vs E_γ at $\theta_N = 90^\circ$. As before, the same function is shown for $P_y = 0$ (dashed black), 1 (red) and -1 (purple).

5.3.7 Sideband Subtraction

Following the logic of Eq. (5.16), a formula is derived to remove background contributions and appropriately scale $C_{x'}$ to acquire a best estimate for the true value. The equation used for this is shown below (see appendix Sec. C.2 for derivation):

$$C_{x'} = \frac{C_{x',\text{raw}}\text{Area}_{\text{hist}} - C_{x',\text{BG}}\text{Area}_{\text{pol}}}{\text{Area}_{\text{hist}} - \text{Area}_{\text{pol}}} \quad (5.17)$$

$C_{x',\text{raw}}$ is the raw extracted $C_{x'}$ values from likelihood without sideband subtraction. $C_{x',\text{BG}}$ is the $C_{x'}$ as measured in the background sample using the same process. The areas are as previously defined in Eq. (5.8) and Eq. (5.9). As visualised in Fig. 5.22, this sideband correction intuitively leads to a scaling of raw $C_{x'}$ based on how much it deviates from background values. Thus, an underestimate of $C_{x',\text{BG}}$ will lead to an overestimate of corrected $C_{x'}$. An over-correction of $C_{x'}$ seems to have occurred at $E_\gamma \approx 0.5\text{GeV}$, which has pushed the value further past the physical limit of $C_{x'} = 1$. It is expected that this would be encapsulated by a full systematic analysis.

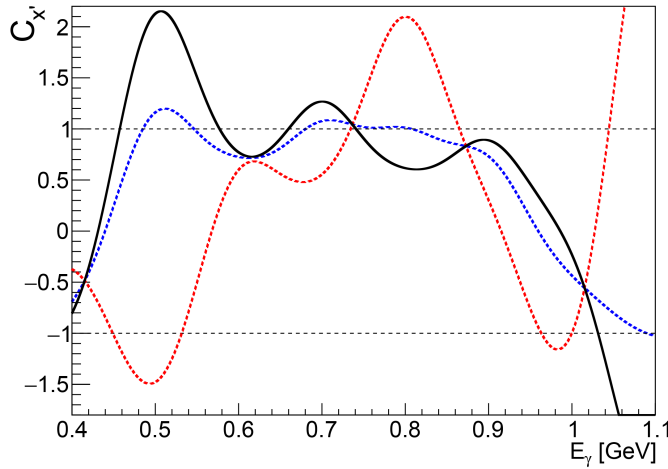


Fig. 5.22 $C_{x'}$ functions of E_γ at $\theta_N = 90^\circ$. The original raw $C_{x'}$ extraction is shown as dashed blue, background $C_{x'}$ is shown as dashed red. The result of implementing sideband subtraction (Eq. (5.17)) is shown as solid black.

5.3.8 Systematic Uncertainty of P_y

As mentioned, this analysis has assumed a P_y value of 0 to reduce the complexity of the likelihood equation and final result. In reality, P_y could take any value between the physical limits of ± 1 . In Fig. 5.19 and Fig. 5.21, it was previously shown how assuming $P_y = \pm 1$ affected the initial extraction of $C_{x'}$ and $C_{x',\text{BG}}$ at $\theta_N = 90^\circ$. In Fig. 5.23, the full process of sideband subtraction is shown for both $\theta_N = 90^\circ$ and $\theta_N = 60^\circ$, for both P_y extremes. Importantly, it is shown how the possible range of P_y

affects the final corrected $C_{x'}$ value, which can be considered a component of systematic uncertainty, although a full analysis of systematic uncertainty is not provided in this work.

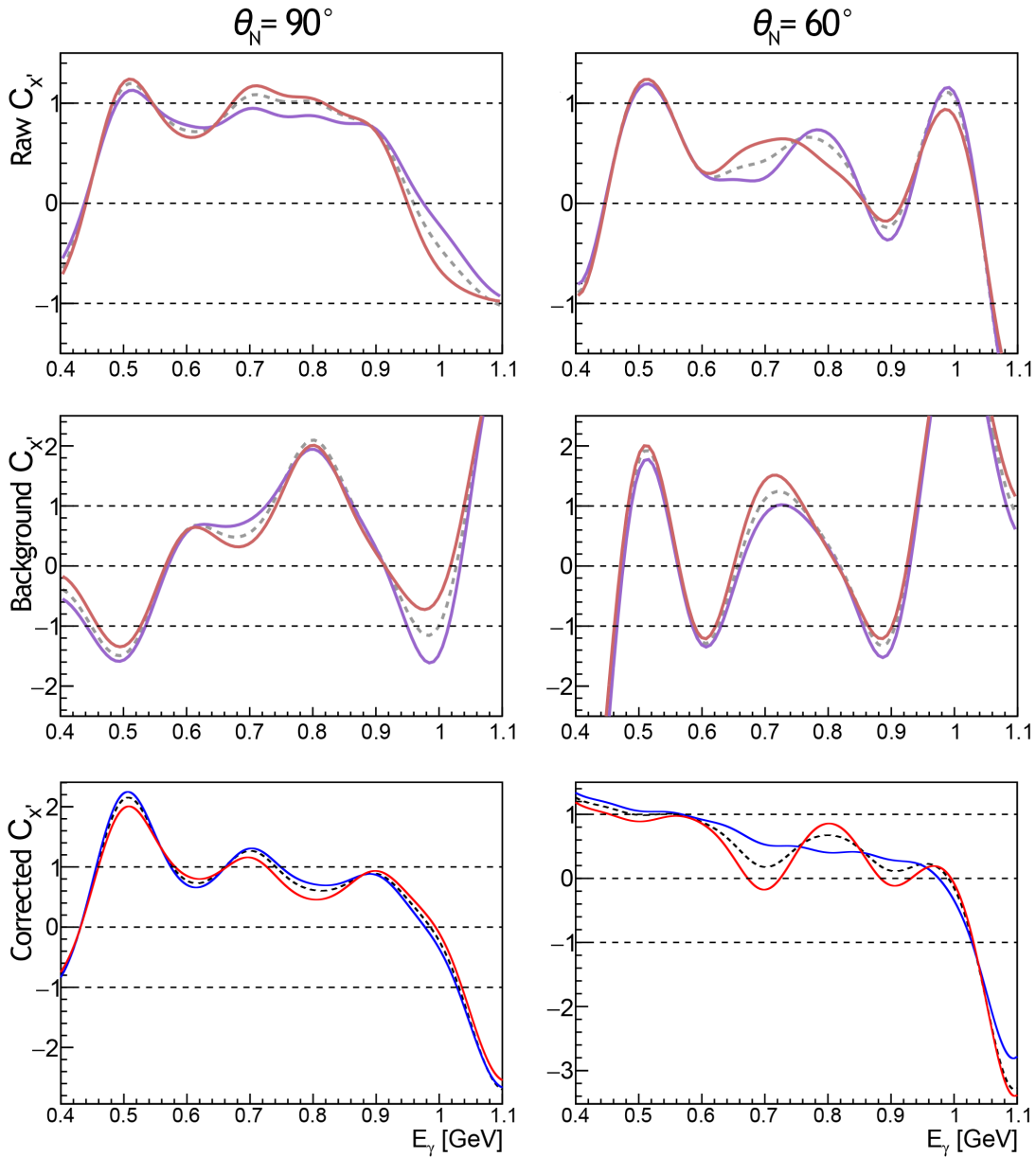


Fig. 5.23 Extracted $C_{x'}$ values at $\theta_N = 90^\circ$ (left) and 60° (right) for the region of interest (top) and the background sample (middle). For each case, the result of fixing P_y at +1 (red) and -1 (blue) for a given $C_{x'}$ extraction is presented. A sideband subtraction operation results in corrected $C_{x'}$ values (bottom), with additional lines corresponding to using the P_y extremes in sideband calculations, showing the effect on the final result.

5.3.9 Capturing Statistical Uncertainty (Bootstrap technique)

It is expected that there is large $C_{x'}$ uncertainty in regions of low statistics (i.e. high photon energies and extreme scattering angles). There is a need to capture statistical uncertainty before any conclusion can be drawn about $C_{x'}$. The chosen method to extract this is the Non-Parametric Bootstrap (NPB) technique [96]. This involves randomly resampling the dataset until a new dataset of the same size is created. Because each entry in this new dataset was independently chosen by random from the original, duplicate entries may appear. To apply this method, the 9.91×10^4 events of interest are randomly sampled from until a new dataset of equivalent size is built. The same likelihood minimisation technique as before is again used to extract a $C_{x'}$ function from this new resampled dataset, resulting in a new "bootstrap" $C_{x'}$ function which has a slight deviation from the original. This process is repeated many times, each creating a new dataset by resampling the original, and extracting a new unique bootstrap $C_{x'}$ function. After many bootstrap functions are created and overlaid together, the distribution captures the statistical uncertainty of $C_{x'}$ (shown Fig. 5.24). With each new likelihood minimisation implemented on a resampled dataset, the Gaussian means are randomly shifted by varying the set b parameter in Eq. (5.15). This prevents the result being biased by the regular intervals of Gaussian peaks, but may result in the original $C_{x'}$ function not being perfectly centred on the average of overlapping bootstrap functions. The latter should be considered the new value of $C_{x'}$.

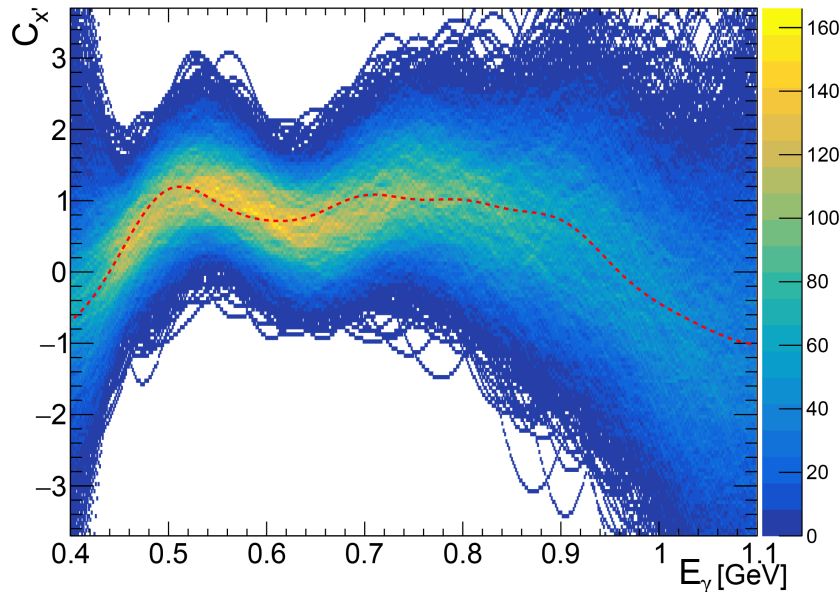


Fig. 5.24 Result of extracting 3000 $C_{x'}$ functions via a bootstrap technique. Colour axis represents number of overlapping functions, indicating stronger confidence in the corresponding value. Dashed red line shows the original minimisation before NPB.

Removing non-converging functions

In some cases, a likelihood minimisation is not able to converge on a bootstrap dataset. The effect of this is visible in Fig. 5.25 as a strong line at $C_{x'} = 0$. To separate these non-converging functions from successful convergences, the volume under each surface function is found by a integration algorithm. This must be done on an absolute version of the function so that "negative" volume is added rather than subtracted. A histogram of these volumes is shown below in Fig. 5.26.

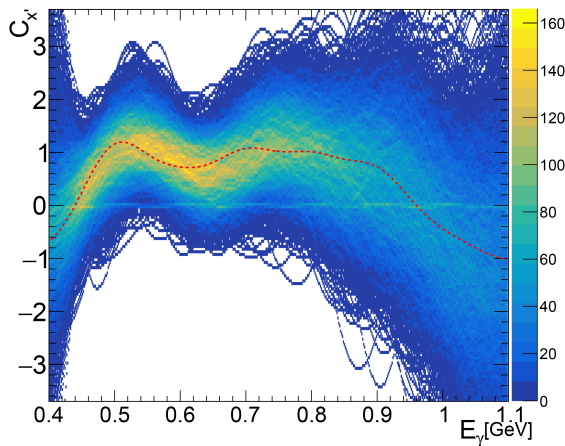


Fig. 5.25 The same result of 3000 bootstrap $C_{x'}$ functions but without removing non-converging results, to demonstrate the resulting erroneous line at $C_{x'} = 0$.

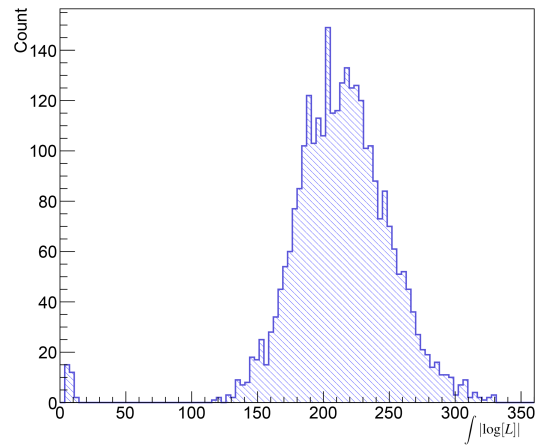


Fig. 5.26 A histogram of the area under absolute bootstrap functions extracted. Non-converging functions are visible as a small peak close to 0, which can be discarded.

Quantifying statistical uncertainty (Area plots)

In order to turn the complex bootstrap result into a more readable $C_{x'}$ function with a quantifiable standard error, fine bins of E_{γ} are taken, and for each, the number of overlapping bootstrap functions is considered as a 1D histogram. To this, a Gaussian function is fitted (Fig. 5.27), from which, the mean (μ) and standard deviation (σ) is used to define a range of $C_{x'}$ ($\mu \pm \sigma$). After all bins across E_{γ} are considered, a region of $C_{x'} \pm \sigma$ is created across E_{γ} (Fig. 5.28), which represents one standard deviation of statistical error. This process is done for both raw $C_{x'}$ (region of interest) and background $C_{x'}$ (sideband region), generating an area plot for each, and hence quantifying statistical uncertainty of each. In the next subsection, these errors will be propagated to the result.

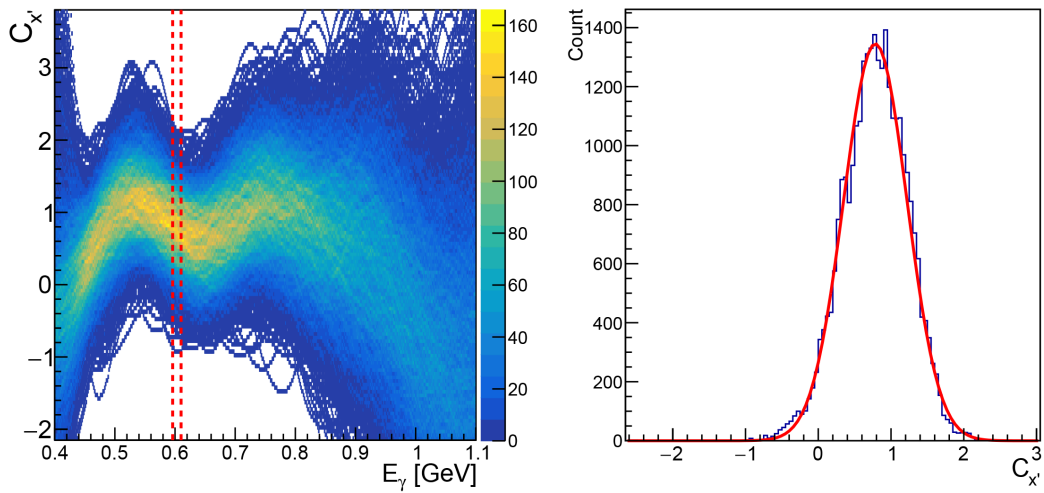


Fig. 5.27 A demonstration of the procedure to create a simple $C_{x'}$ area function from the overlapping bootstrap functions. On the left, a region corresponding to 0.596-0.6 GeV is selected (red dashed lines). This region is projected as a histogram of $C_{x'}$ values (right), to which a Gaussian function (solid red line) is fitted, finding $\mu = 0.784$, $\sigma = 0.435$, which defines the respective mean and height of the area plot for the given bin of E_γ .

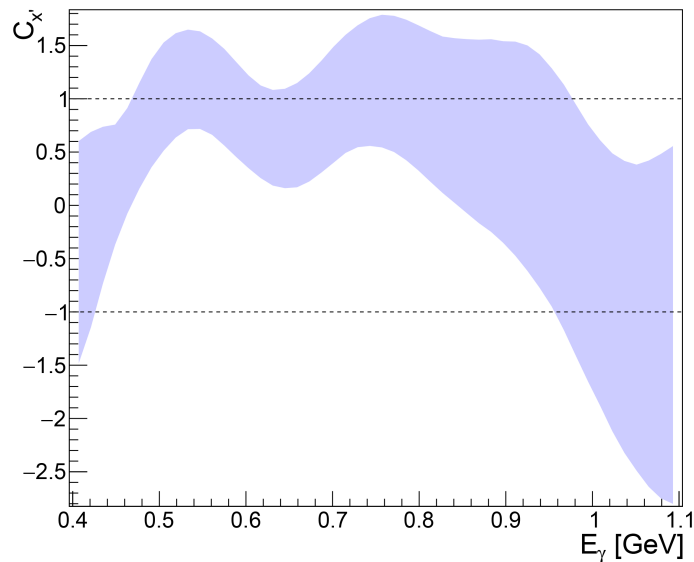


Fig. 5.28 Raw $C_{x'}$ result ($\theta_N = 90^\circ$) presented as an area plot, with height representing one standard deviation of statistical error ($\pm\sigma$).

5.3.10 Statistical Error Propagation

As a final step, the statistical uncertainty of corrected $C_{X'}$ values from sideband subtraction must also be established, so that it too can be displayed in the result. In order to calculate this error ($\delta C_{X'}$), the error of each individual variable in Eq. (5.17) must be considered in how they propagate through the equation. For a full derivation of the $\delta C_{X'}$ formula, see appendix Sec. C.2. This $\delta C_{X'}$ formula is applied over fine bins of E_γ (the same bins used in the previous section), and used to define a range of $C_{X'}$, once again creating an area plot. Fig. 5.29 shows once again the process for both $\theta_N = 90^\circ$ and 60° with statistical uncertainty shown as areas, ultimately presenting the final result as such.

5.3.11 Assuming Background $C_{X'} = 0$

In Sec. 5.3.6, background $C_{X'}$ was found to have non-zero values via the likelihood estimation. However, the statistical uncertainty of these values, measured using the process described in Sec. 5.3.9, showed a large uncertainty (see the middle row of Fig. 5.29), such that $C_{X'} = 0$ is always within 3σ of statistical uncertainty. It's therefore plausible that background is in fact $C_{X'} = 0$, with any apparent value being due to statistical uncertainty. In this subsection, it will be explored how a background of $C_{X'} = 0$ changes the final result. This can be implemented simply into the current process by setting $C_{X',BG}$ (from Eq. (5.17)) and $\delta C_{X',BG}$ (derived in Appendix Sec. C.2) to both be zero in the associated sideband subtraction formulae. Fig. 5.30 shows how the result changes upon implementing this.

The resulting change in the mean value of $C_{X'}$ is minor (relative to statistical uncertainty), due to background being measured as only 26.8% of the data. The change in the overall statistical error is even less noticeable, as this is dominated by the statistical error of $C_{X',raw}$. With this study, it can be concluded that the working assumption of physical, non-zero background contributions (as opposed to simple $C_{X',BG} = 0$ background dilution), has not significantly affected the result. To fully encapsulate both possibilities, this can be considered another contribution to systematic error.

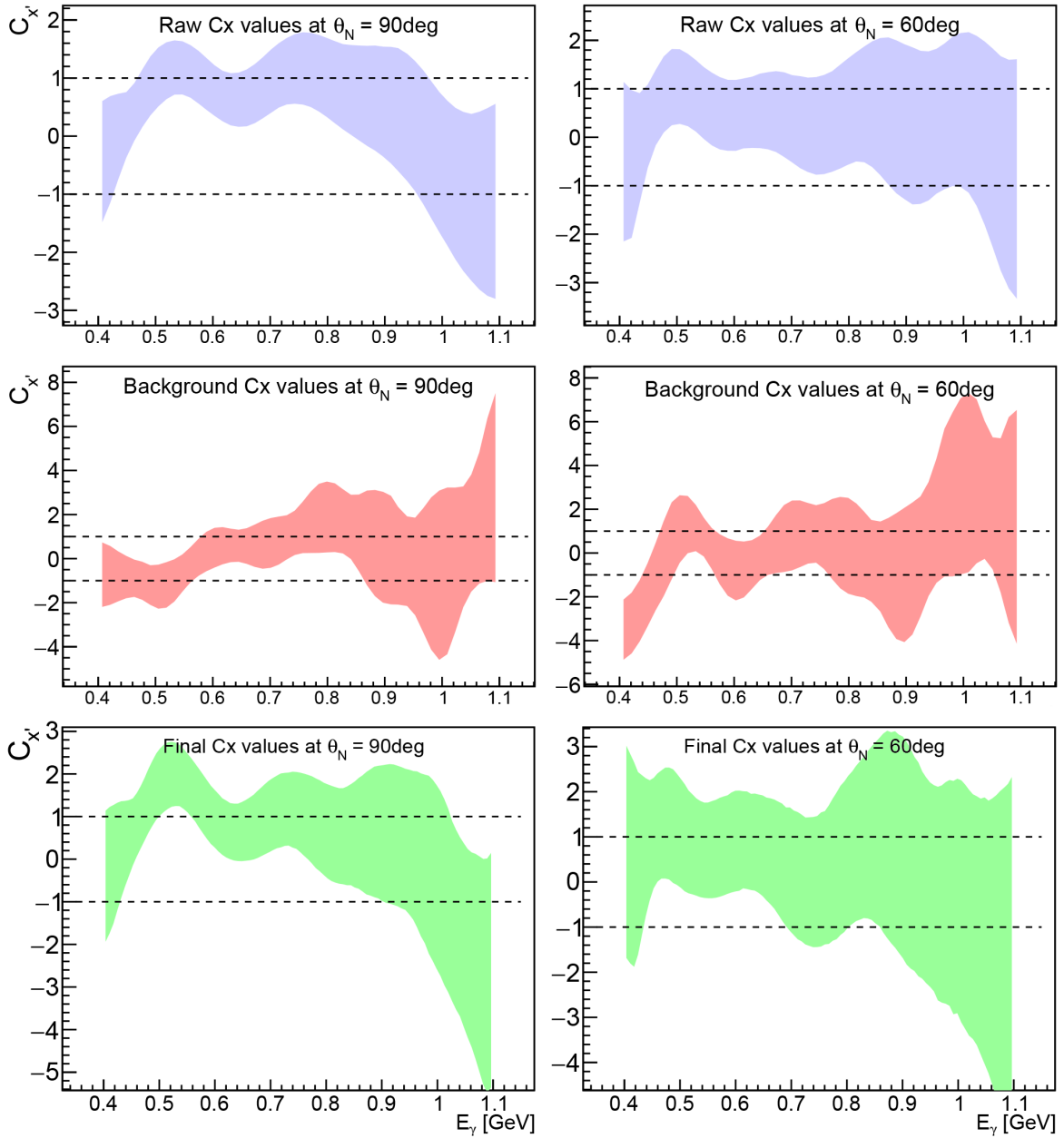


Fig. 5.29 Raw $C_{x'}$ (top) and Background $C_{x'}$ (middle) area plots, and the resulting corrected and final $C_{x'}$ area plot (bottom). Results at both $\theta = 90^\circ$ (left) and $\theta = 60^\circ$ (right) are shown in parallel. Horizontal dashed lines at physical limits are shown throughout.

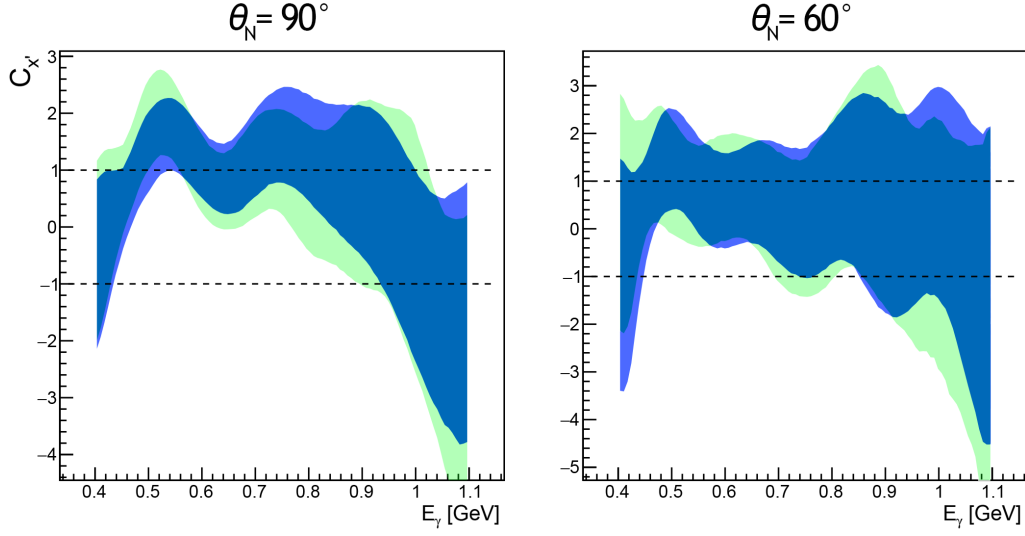


Fig. 5.30 A comparison between two methods of obtaining the sideband corrected $C_{x'}$ result. The blue region corresponds to setting $C_{x',BG} = 0$ (along with associated errors). The light green region is corrected $C_{x'}$ as calculated using the previously established non-zero values of $C_{x',BG}$. Darker areas indicate where both regions overlap.

5.3.12 Binned Asymmetries Method

This subsection details a potential alternative method of extracting both P_y and $C_{x'}$, that was investigated, but ultimately not used in the final analysis due to limitations. It is provided here only for interest, but could be utilised in future work. Considering again Eq. (5.10), it can be seen that the photon polarisation term, P_γ^\odot , only appears with $C_{x'}$, implying an asymmetrical dependence on photon helicity. Considering the cross section of positive and negative photon helicities separately:

$$\begin{aligned} I^+ &= I_0[1 + A_y(P_y \cos \phi_{sc} - C_{x'} |P_\gamma^\odot| \sin \phi_{sc})] \\ I^- &= I_0[1 + A_y(P_y \cos \phi_{sc} + C_{x'} |P_\gamma^\odot| \sin \phi_{sc})] \end{aligned} \quad (5.18)$$

This leads to the following asymmetry formula:

$$\frac{I^+ - I^-}{I^+ + I^-} = \frac{-A_y C_{x'} |P_\gamma^\odot| \sin \phi_{sc}}{1 + A_y P_y \cos \phi_{sc}} \quad (5.19)$$

This formula can be used to extract a measurement of P_y and $C_{x'}$ by using the data to create a histogram of I^+/I^- asymmetry versus ϕ_{sc} , then optimally fitting a function with P_y and $C_{x'}$ as parameters. To create the asymmetry histogram, the data is first sorted into two different ϕ_{sc} histograms

corresponding to positive and negative photon helicity cross sections. Then, a histogram-wise operation is used to produce a new histogram of asymmetry, to which a function can be fitted. To investigate the variance with other parameters, such as photon energy (E_γ), we are forced to bin the data accordingly. It is desired to have sensitivity to both E_γ and θ_N , however low statistics forces a compromise to a few bins of E_γ as shown in Fig. 5.31.

When deciding how to parameterise Eq. (5.19), and what fit function to use, the unknowns should be considered. A_γ and P_γ^\ominus both vary event-by-event, but this information has been lost. One method of accounting for this is to simply lump terms together as single parameters. This enables a simple fit function of the form $[A \sin x]/[1 + B \cos x]$, where $A = -A_\gamma C_{\gamma'} |P_\gamma^\ominus|$ and $B = A_\gamma P_\gamma$. An attempt at fitting this function to each E_γ bin is shown in Fig. 5.31.

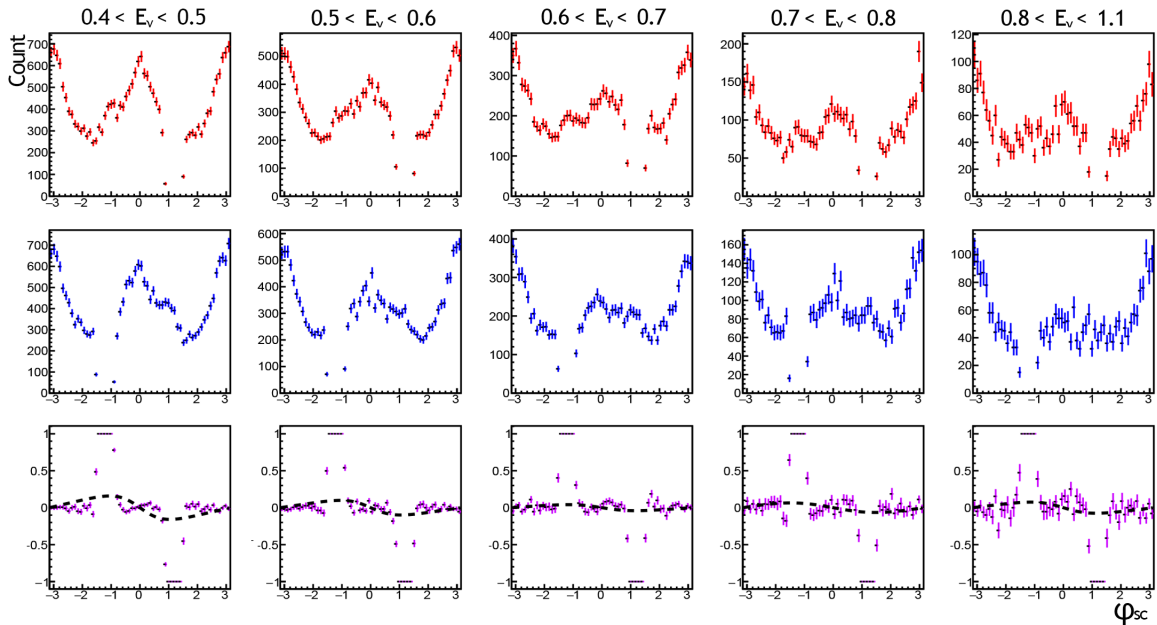


Fig. 5.31 The process of creating asymmetry histograms (bottom row) using positive (top row) and negative (middle row) photon helicity cross sections. Each column corresponds to bins of E_γ (bin limits given above each column in units of GeV). Black dashed lines show the result of fitting functions of the form $A \sin(x)/[1 + B \cos(x)]$ to each bin using a χ^2 minimisation algorithm. The data is subject to systematic uncertainty and acceptance effects which prevent a good fit.

Even with statistical limitations aside, this method has a few problems that currently prevent an obtainable result. First of all, detector acceptance effects create biases in the cross section, as seen in Fig. 5.31 from the gaps in data at 1-1.5 radians. It was explained in Sec. 5.3 how detector acceptance effects made P_γ measurements unreliable, but $C_{\gamma'}$ was unaffected because of the averaging effect of the frequent helicity flips. This time, however, the acceptance effects are not averaged out, because

the ϕ angle is flipped when populating the negative helicity cross section histogram. Hence, the effect is carried into the final asymmetry histograms. A full study of detector acceptance effects is required to account for this. The next problem is background contributions, however this could be accounted for following a similar method as used with the maximum likelihood method. Finally, the extracted parameters would still be tied to other variables (A_γ and P_γ^{\odot}). With all this in mind, the likelihood method with bootstrapping was the preferred technique for this analysis.

Chapter 6

Results

Following analysis, values of the double polarisation observable, $C_{x'}^n$, from deuteron photo-disintegration are extracted from JLab's g13a dataset, and subsequently corrected for background contributions. From this, $C_{x'}^n$ is presented as a surface of values across a range of photon beam energy, E_γ and recoil neutron polar angle, θ_N (Fig. 6.1).

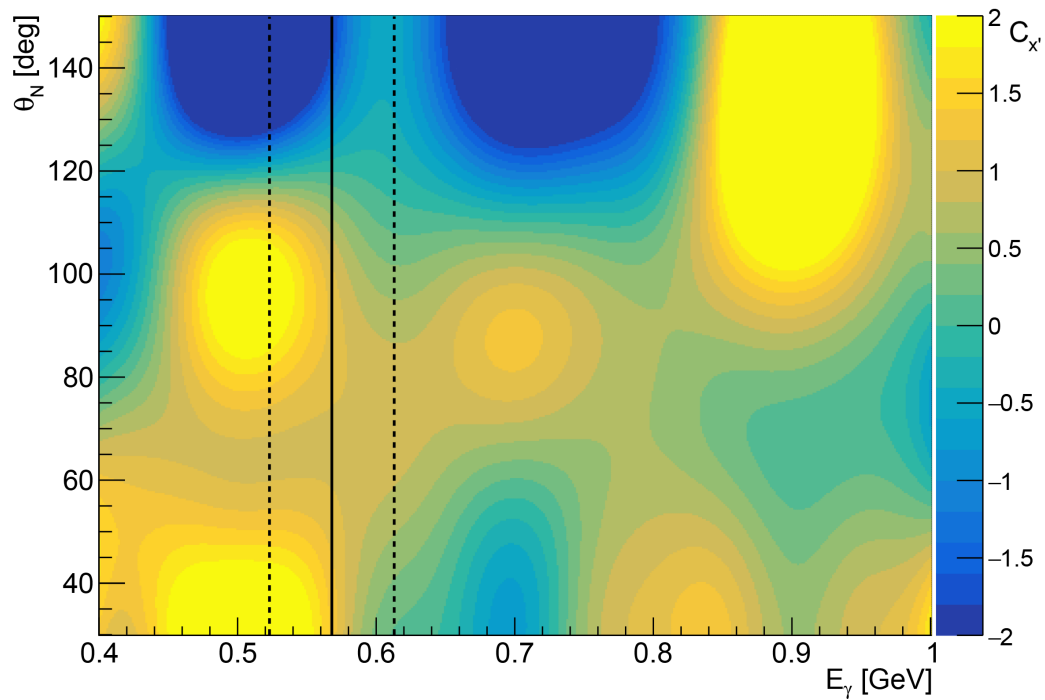


Fig. 6.1 Final $C_{x'}^n$ values after sideband subtraction, presented as a 2D surface of values (represented by a colour axis) across E_γ and θ_N . Hard limits are imposed at $C_{x'} = \pm 2$. Vertical lines show nominal $d^*(2380)$ resonance.

Fig. 6.2 shows slices of this result taken at fixed angles ($\theta_N = 90, 60$) in order to present a calculated statistical uncertainty as a height representing $\pm\sigma$. Also in Fig. 6.2 is a comparison with results from [1]. Note that the result from [1] is inverted, due to a sign flip on $C_{x'}$ in the formula used.

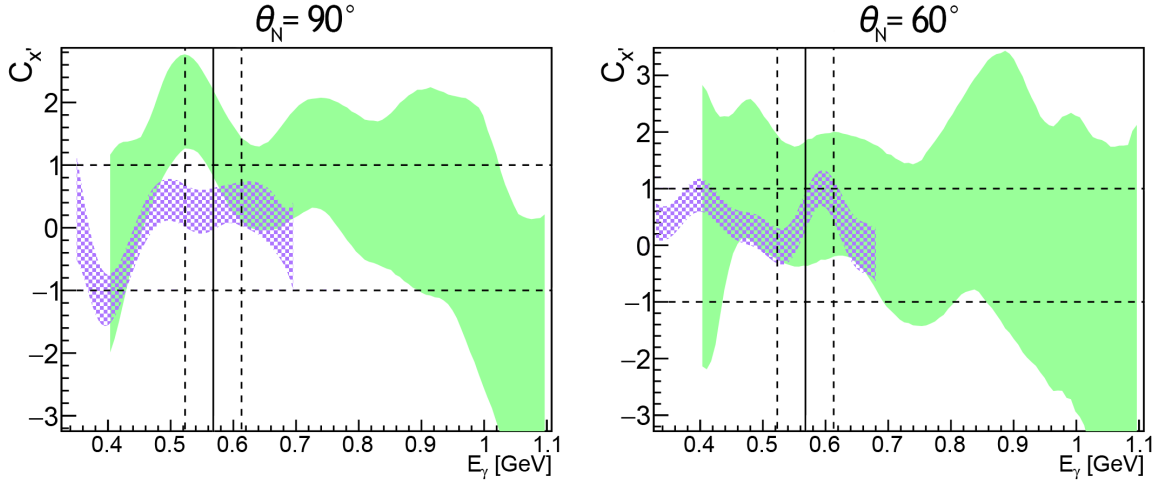


Fig. 6.2 Final $C_{x'}^n$ values versus E_γ at fixed angles after sideband subtraction, presented as an area (green) representing statistical uncertainty only. The overlaid purple shaded area shows results from Bashkanov *et al.* [1]. Vertical lines show nominal $d^*(2380)$ resonance.

These results show a partial agreement with Bashkanov *et al.*'s first $C_{x'}^n$ measurement. For $\theta_N = 90^\circ$, the disagreement between E_γ 460-600 MeV coincides with the result entirely exceeding the physical limits of $C_{x'} = \pm 1$, suggesting the disagreement is caused by a systematic error which is further exaggerated by an over-correction in background subtraction. While the range of the result exceeds Bashkanov *et al.*'s E_γ coverage, the statistical uncertainty becomes large at higher values of E_γ . This uncertainty is also larger at angles away from $\theta_N = 90^\circ$, where less data lies (data distribution shown previously in Fig. 5.17). Because of this, there is no meaningful result above 0.7-0.9 GeV at $\theta_N = 60^\circ$. It is expected that statistics can be improved by the inclusion of g13b, aimed to be incorporated into this analysis in the near-future. Additionally, a full study of systematic uncertainty is required before these results can be published.

Nonetheless, these results are an important proof of concept for a new method of performing polarisation analysis with Jefferson Lab's CLAS data, which utilises a novel technique of measuring neutron polarisation via the start counter, using its detector element as an analysing polarimeter. It is also expected that the same technique can be applied with CLAS12 data (discussed more in Sec. 7.4). If this technique is fully developed and utilised on larger datasets, then physicists can look forward to the list of published measurements for P_y and $C_{x'}$ growing, with CLAS and CLAS12

extending measurements to much greater kinematic coverage. This would mean the reaction of deuteron photo-disintegration would become more understood, and corresponding models would be given more constraints. Modelling the hard-scattering regime and beyond, understanding short-range correlations, and the exciting new efforts into studying hexaquarks are all examples of research areas that would greatly benefit from accessible polarisation analyses of this fundamental reaction. Ultimately, these efforts will contribute to deeper insights into the strong force and hadron structure.

Chapter 7

Future Work

This final chapter will conclude with the desired next steps to develop this analysis further, as well as recommendations for future utilisation of the technique that has been presented.

7.1 Including g13b

The quality of this analysis, like all polarisation analyses, is highly dependent on overall statistics. The entire g13a dataset was used to extract 9.91×10^4 events of interest, with the distribution of data mainly covering $E_\gamma = 0.4\text{-}0.6$ GeV. Due to time constraints and deprecated software, g13b, the linearly polarised photon dataset, was not utilised in this analysis. However, its inclusion is strongly desired, as g13b contains roughly twice as much data as g13a, and better covers the higher photon energy range. Despite the slight change in set-up, repeating the analysis with g13b data would be straight forward. This is because circularly polarised photon events can still be accessed within the linearly polarised dataset, by appropriately selecting data which contains no linear polarisation. This means the same reduced cross-section equation (Eq. (5.10)) is maintained. See Ref. [97] for an example of an analysis which focuses on circularly (or "elliptically") polarised photons from a linearly polarised beam experiment, which can be utilised with JLab data in an identical manner.

It is hoped to augment this analysis with the g13b dataset in the near future to better improve the statistical uncertainty of the result. This increase in statistics may enable methods such as the binned asymmetry technique described in Sec. 5.3.12, and increase the feasibility of the systematic studies described in the next section.

7.2 Systematic Studies

In order for the results of this work to be published, a full analysis of systematic uncertainty is required. In general, this is a consideration for the uncertainty associated with instrumental off-sets and analysis steps, in how they propagate to, or bias the final result. This can be presented as values alongside the result representing the total systematic error (see Fig. 3.2 for an example of this). Two important systematic studies were included in Chap. 5; the possible effect of P_y (see Sec. 5.3.8), and the possibility of $C_{x,BG} = 0$ (see Sec. 5.3.11). In this section, a list of additional recommended systematic studies are provided. Systematic uncertainties can only be well-determined if they outweigh statistical effects. Thus, systematic studies can only be discussed as upper estimates.

7.2.1 Data Selection

Each selection or "cut" made to the data represents a definition being imposed on selected events. For example, the "deltabeta" cut is, in essence, defining a proton as any positive event track within ± 0.015 of the expected $\Delta\beta = 0$ (see Sec. 5.2.3). The systematic error created by such definitions can be investigated by varying the associated selection parameters (typically by 0.5σ), repeating the full analysis, and then measuring the resulting change in the final $C_{x'}$ result. Ideally, in a robust analysis, changing the chosen cut parameters should not significantly affect $C_{x'}$, meaning associated systematic errors should be small. A full systematic study of cuts also affords a more complete and careful measure of cut effectiveness than the study on incremental signal to noise ratio in Sec. 5.2.9.

Changing the initial skim criteria to have no restriction on neutral particles may also yield more data, as this would allow the selection to include events where photons were detected, but not necessarily part of the reaction.

7.2.2 Method of $C_{x'}$ Extraction

The reliability of the chosen method of $C_{x'}$ extraction can be tested using an artificial dataset with the value of $C_{x'}$ (and P_y) pre-set and baked in. This would allow a direct comparison to be made between the true value and extracted value. The accuracy can then be quoted as a systematic error in the method. This requires an event generator and an accurate simulation of detector geometries, acceptance effects and background events, which was beyond the scope of this thesis.

7.2.3 $C_{X'}$ Parameterisation

In the used maximum likelihood technique, for the full parameterisation of $C_{X'}$ (given in Eq. (5.14) and Eq. (5.15)), the number of evenly distributed Gaussian functions across E_γ was chosen to be $G_n = 8$. Other values of G_n should be tested to check if the result is affected. It may also lead to a more efficiently minimising function, or an increase in $C_{X'}$ confidence. A flaw of the current parameterisation method is that regions of lower statistics are offered the same complexity as regions of higher statistics. For more efficiency, the distribution of parameters should instead respect the distribution of statistics. One way of achieving this is having fewer but wider Gaussian functions at higher energy regions.

7.2.4 Signal Ratio Variation

For the purposes of sideband subtraction, an estimation of signal and background ratio is necessary. In this analysis it was measured by calculating the integrals of both the final $MM^2(\gamma d \rightarrow p_1 X)$ histogram and a component polynomial within the predefined region of interest ($Area_{hist}$ and $Area_{BG}$). One major assumption being made is that the ratio between these areas and their associated uncertainties does not change with θ_N or E_γ . This assumption should be tested with a study that measures $Area_{BG} / Area_{hist}$ across θ_N and E_γ . While limiting statistics is a concern when considering additional parameters, it should be noted that the uncertainty in $Area_{hist}$ and $Area_{BG}$ currently has a negligible contribution to the final error in the $C_{X'}$ result, with the majority coming from max likelihood uncertainty. It could therefore be afforded to consider both $Area_{hist}$ and $Area_{BG}$ in terms of an additional parameter. The next most preferred additional parameter is E_γ , as this would most neatly and easily integrate into sideband subtraction, which already operates in terms of E_γ .

7.2.5 $C_{X',BG}$ Variation

Another major assumption of the analysis is that the $C_{X'}$ value as measured in the sideband region, used as the background sample ($C_{X',BG}$), does not vary with $MM^2(\gamma d \rightarrow p_1 X)$, and therefore only a single background measurement is required to know the background value which contributes to the extracted $C_{X'}$. As a first step, this assumption could be tested by comparing a $C_{X'}$ value for background samples taken at both the left and right sides of the $MM^2(\gamma d \rightarrow p_1 X)$ region of interest. Any variation between the left and right should be interpolated to obtain a better estimate of background $C_{X'}$ in the

region of interest. However, it should be noted that the systematic study in Sec. 5.3.11 showed that $C_{x\text{BG}}$ variation does not significantly alter the final result, and therefore has a small contribution to systematic uncertainty.

7.3 Measuring P_y

It is ultimately desired to have a measurement for P_y alongside $C_{x'}$ to fully describe the reaction of deuteron photo-disintegration. It was explained in Sec. 5.3 why this was not feasible in this analysis (low statistics and acceptance effects). However, assuming acceptance effects are accounted for, and a wealth of statistics were available, measuring P_y would become feasible. That said, there are a few important cautions to keep in mind. Firstly, extracting both observables simultaneously requires additional minimisation parameters, leading to stretching data more thinly, longer computational time, and increasing the risk of non-converging functions or otherwise false solutions. Additionally, the current method is not very sensitive to the value of P_y , as shown by the relatively small change in $C_{x'}$ parameter output when using $P_y = \pm 1$ extremes. This could indicate that its measurement would not be very accurate via this method without a massive increase in statistics. Nonetheless, this is worth investigating.

7.4 Extending to CLAS12 and the SVT

The method described in this thesis was focused on data from CLAS [19] (the 6 GeV era), re-purposing the start counter (SC) [78] as an analysing polarimeter. However, the more modern CLAS12 [69] has had many ongoing experiments during the time-frame of this project, with valuable data recently becoming available. This data, which reaches new energy regimes, represents the potential for high impact analyses and investigations of the quark-gluon energy regime of hadrons. It is proposed that a similar method to the CLAS-specific method described in this thesis could be applied to CLAS12. This can be achieved by re-purposing the silicon vertex tracker (SVT) in the same way as the SC.

To briefly summarise, the SVT [98] is a component of CLAS12, the purpose of which is to establish the starting vertex of outgoing particles. The SVT replaces the role of the SC, providing not only a measurement of start time, but detailed positional information. It consists of three circular arrays of semi-conducting silicon modules surrounding the beamline-axis, at radii of 65, 93, and

120 mm. Each module consists of silicon, carbon fibre*, and a bus cable†, with arrangement and thicknesses shown in Fig. 7.1.

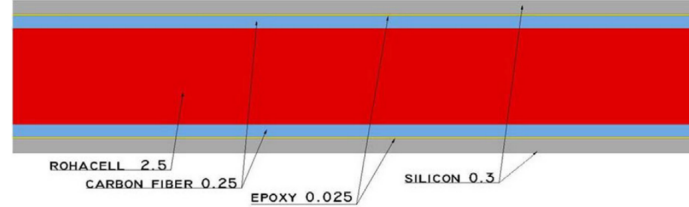


Fig. 7.1 The cross section of the module taken from [98]. The dimensions are in mm.

For utilising the SVT as an analysing polarimeter to be feasible, the neutron scattering cross section of the component must be similar or better than the already proven SC. To estimate this, we can consider the relative area densities (density per unit surface area) of each. As discussed in Sec. 4.3.1, the active region of SC had a thickness of 0.215 cm. The type of scintillator used (EJ-200) has a density of 1.023 g cm^{-3} . Multiplying these gives an area density of 0.22 g cm^{-2} (other material is considered negligible). To estimate the area density of the SVT, first consider the area density of each material in a module as follows (epoxy ignored):

$$\begin{aligned} \text{Rohacell}^\circledast: & \quad 0.25 \text{ cm} \times 0.071 \text{ g cm}^{-3} = 0.0178 \text{ g cm}^{-2} \\ \text{Carbon Fibre}: & \quad 0.025 \text{ cm} \times 2.19 \text{ g cm}^{-3} = 0.0548 \text{ g cm}^{-2} \\ \text{Silicon}: & \quad 0.03 \text{ cm} \times 2.33 \text{ g cm}^{-3} = 0.0699 \text{ g cm}^{-2} \\ \text{Total}: & \quad 0.142 \text{ g cm}^{-2} \end{aligned}$$

There are three SVT regions, meaning three modules along a neutron's potential path, giving a total area density of $3 \times 0.142 = 0.43 \text{ g cm}^{-2}$. This is roughly double the calculation of SC area density (0.22 g cm^{-2}). Based on this, we could therefore expect an increased scattering cross section when using the SVT as an analysing polarimeter, yielding roughly double the events of interest for equivalent statistics, making applying this method to CLAS12 even more powerful than the CLAS-specific method as described within this thesis. Given that CLAS12 will involve even higher statistics experiments, and extend to higher energy regimes, it is highly recommended for this technique and similar analyses to be applied to CLAS12 datasets.

*Mitsubishi type K13C2U [99]

†Rohacell 71 [100]

7.4.1 Other Detector Systems

As a final point, it is expected that the methodology used in this thesis has potential to be applicable to many other apparatuses where energetic nucleons (above ~ 0.1 GeV) are produced in nuclear reactions. However, no further feasibility studies of other systems have been performed at this time.

Bibliography

- [1] M. Bashkanov *et al.*, “First measurement of polarisation transfer C_x^n in deuteron photodisintegration”, *Physics Letters B* **844**, 138080 (2023).
- [2] D. Griffiths, *Introduction to Elementary Particles*, 2nd ed. (Cambridge University Press, 1987).
- [3] Particle Data Group *et al.*, “Review of Particle Physics”, *Progress of Theoretical and Experimental Physics* **2020**, 083C01 (2020), <https://doi.org/10.1093/ptep/ptaa104>.
- [4] R. Mann, *An Introduction to Particle Physics and the Standard Model* (CRC Press, 2010).
- [5] *A dictionary of physics* (Oxford University Press, 2009).
- [6] R. G. Milner, *A Short History of Spin*, Sept. 2013, <https://arxiv.org/abs/1311.5016>.
- [7] R. Shankar, *Principles of Quantum Mechanics*, 2nd ed. (Plenum Press, 233 Spring Street, New York, NY, 10013, 1994).
- [8] A. Pickering, *Constructing Quarks - A Sociological History of Particle Physics* (Edinburgh University Press, 1984).
- [9] D. H. Perkins, *Introduction to High Energy Physics*, 4th ed. (Cambridge University Press, 2000), p. 87.
- [10] M. Gell-Mann, “The eightfold way: a theory of strong interaction symmetry”, 10.2172/4008239 (1961), <https://www.osti.gov/biblio/4008239>.
- [11] F. Halzen and A. D. Martin, *Quarks & Leptons: An Introductory Course in Modern Particle Physics* (John Wiley & Sons, 1984).
- [12] L. D. Roper, “Evidence for a P_{11} Pion-Nucleon Resonance at 556 MeV”, *Phys. Rev. Lett.* **12**, 340–342 (1964), <https://link.aps.org/doi/10.1103/PhysRevLett.12.340>.
- [13] J. Pivarski, “Cross section”, *Fermilab Today* (2013), https://www.fnal.gov/pub/today/archive/archive_2013/today13-03-01.html.
- [14] L. Hoddeson and G. Baym, *Critical assembly: a technical history of Los Alamos during the Oppenheimer years, 1943-1945* (Cambridge University Press, 1993).
- [15] T. Chatterji, *Neutron Scattering from Magnetic Materials* (Elsevier Science, Amsterdam, 2006).
- [16] E. Hecht, *Optics (5th ed.)* (Pearson Education Limited, 2017).
- [17] L. W. Alvarez and F. Bloch, “A Quantitative Determination of the Neutron Moment in Absolute Nuclear Magnetons”, *Phys. Rev.* **57**, 111–122 (1940), <https://link.aps.org/doi/10.1103/PhysRev.57.111>.
- [18] W. Schweika, “Polarized Neutron Scattering and Polarization Analysis”, in 43rd IFF spring school Scattering Methods for Condensed Matter Research: Towards Novel Applications at Future Sources (Forschungszentrum Jülich, Mar. 2012), <https://juser.fz-juelich.de/record/20443>.

- [19] B. Mecking *et al.*, “The CEBAF large acceptance spectrometer (CLAS)”, *Nuclear Instruments and Methods in Physics Research Section A: Accelerators, Spectrometers, Detectors and Associated Equipment* **503**, 513–553 (2003), <https://www.sciencedirect.com/science/article/pii/S0168900203010015>.
- [20] D. G. Ireland, E. Pasyuk, and I. Strakovsky, “Photoproduction reactions and non-strange baryon spectroscopy”, *Progress in Particle and Nuclear Physics* **111**, 103752 (2020), <http://dx.doi.org/10.1016/j.pnpnp.2019.103752>.
- [21] V. Crede and W. Roberts, “Progress towards understanding baryon resonances”, *Reports on Progress in Physics* **76**, 076301 (2013), <http://dx.doi.org/10.1088/0034-4885/76/7/076301>.
- [22] R. Gilman and F. Gross, “Electromagnetic structure of the deuteron”, *Journal of Physics G: Nuclear and Particle Physics* **28**, R37–R116 (2002).
- [23] P. Rossi *et al.* (CLAS Collaboration), “Onset of asymptotic scaling in deuteron photodisintegration”, *Phys. Rev. Lett.* **94**, 012301 (2005).
- [24] I. Pomerantz *et al.*, “Hard photodisintegration of a proton pair”, *Physics Letters B* **684**, 106–109 (2010).
- [25] J. Napolitano *et al.*, “Measurement of the Differential Cross Section for the reaction ${}^2\text{H}(\gamma, p)n$ at High Photon Energies and $\theta_{\text{c.m.}} = 90^\circ$ ”, *Phys. Rev. Lett.* **61**, 2530–2533 (1988).
- [26] S. J. Freedman *et al.*, “Two-body disintegration of the deuteron with 0.8–1.8 gev photons”, *Phys. Rev. C* **48**, 1864–1878 (1993).
- [27] J. E. Belz *et al.*, “Two-body photodisintegration of the deuteron up to 2.8 gev”, *Phys. Rev. Lett.* **74**, 646–649 (1995).
- [28] C. Bochna *et al.*, “Measurements of deuteron photodisintegration up to 4.0 gev”, *Phys. Rev. Lett.* **81**, 4576–4579 (1998).
- [29] E. C. Schulte *et al.*, “Measurement of the high energy two-body deuteron photodisintegration differential cross section”, *Phys. Rev. Lett.* **87**, 102302 (2001).
- [30] E. C. Schulte *et al.*, “High energy angular distribution measurements of the exclusive deuteron photodisintegration reaction”, *Phys. Rev. C* **66**, 042201 (2002).
- [31] M. Mirazita *et al.* (CLAS Collaboration), “Complete angular distribution measurements of two-body deuteron photodisintegration between 0.5 and 3 GeV”, *Phys. Rev. C* **70**, 014005 (2004).
- [32] M. M. Sargsian, “Polarization observables in hard rescattering mechanism of deuteron photodisintegration”, *Physics Letters B* **587**, 41–51 (2004).
- [33] S. Kay, “First investigation of electromagnetic coupling of the $d^*(2380)$ hexaquark”, PhD thesis (The University of Edinburgh, Nov. 2018).
- [34] H. Clement, “On the history of dibaryons and their final observation”, *Progress in Particle and Nuclear Physics* **93**, 195–242 (2017), <https://www.sciencedirect.com/science/article/pii/S0146641016300771>.
- [35] M. Bashkanov *et al.*, “Dibaryons and where to find them”, *Journal of Physics G: Nuclear and Particle Physics* **51**, 045106 (2024).
- [36] J. Vijande, A. Valcarce, and J.-M. Richard, “Stability of hexaquarks in the string limit of confinement”, *Phys. Rev. D* **85**, 014019 (2012), <https://link.aps.org/doi/10.1103/PhysRevD.85.014019>.
- [37] F. J. Dyson and N.-H. Xuong, “ $Y = 2$ States in $\text{su}(6)$ theory”, *Phys. Rev. Lett.* **13**, 815–817 (1964), <https://link.aps.org/doi/10.1103/PhysRevLett.13.815>.

- [38] P. Adlarson *et al.* (WASA-at-COSY Collaboration), “Abashian-Booth-Crowe Effect in Basic Double-Pionic Fusion: A New Resonance?”, *Phys. Rev. Lett.* **106**, 242302 (2011), <https://link.aps.org/doi/10.1103/PhysRevLett.106.242302>.
- [39] P. Adlarson *et al.*, “Isospin decomposition of the basic double-pionic fusion in the region of the ABC effect”, *Physics Letters B* **721**, 229–236 (2013), <https://www.sciencedirect.com/science/article/pii/S0370269313002311>.
- [40] P. Adlarson *et al.*, “Measurement of the $pn \rightarrow pp\pi^0\pi^-$ reaction in search for the recently observed resonance structure in $d\pi^0\pi^0$ and $d\pi^+\pi^-$ systems”, *Physical Review C* **88**, 10.1103/physrevc.88.055208 (2013), <http://dx.doi.org/10.1103/PhysRevC.88.055208>.
- [41] M. Bashkanov, S. J. Brodsky, and H. Clement, “Novel six-quark hidden-color dibaryon states in QCD”, *Physics Letters B* **727**, 438–442 (2013), <https://www.sciencedirect.com/science/article/pii/S0370269313008666>.
- [42] M. Bashkanov *et al.*, “Deuteron photodisintegration by polarized photons in the region of the $d^*(2380)$ ”, *Physics Letters, Section B: Nuclear, Elementary Particle and High-Energy Physics* **789**, 7–12 (2019), <http://arxiv.org/abs/1809.09398>.
- [43] J. C. McGeorge *et al.*, “Upgrade of the Glasgow photon tagging spectrometer for Mainz MAMI-C”, *The European Physical Journal A*, <https://doi.org/10.1140/epja/i2007-10606-0> (2008).
- [44] T. Walcher, “The mainz microtron facility MAMI”, *Progress in Particle and Nuclear Physics* **24**, 189–203 (1990).
- [45] M. Nicol, “Exploring The Strong Interaction Through Electroproduction Of Exotic Particles”, PhD thesis (The University Of York, 2022).
- [46] G. Clash, “Search for a Singly Strange Hexaquark Using Polarization Data From CLAS12 at Jefferson Lab Virginia”, PhD thesis (The University Of York, 2023).
- [47] R. Weiss *et al.*, “The nuclear contacts and short range correlations in nuclei”, *Physics Letters B* **780**, 211–215 (2018).
- [48] J. Aubert *et al.*, “The ratio of the nucleon structure functions F_2^N for iron and deuterium”, *Physics Letters B* **123**, 275–278 (1983).
- [49] K. Wijesooriya *et al.* (Jefferson Lab Hall A Collaboration), “Polarization measurements in high-energy deuteron photodisintegration”, *Phys. Rev. Lett.* **86**, 2975–2979 (2001).
- [50] D. Watts, D. Glazier, and J. Annand, “Polarisation observables using the nucleon polarimeter with the crystal ball at MAMI”, (2009).
- [51] P. Adlarson *et al.*, “Evidence for a new resonance from polarized neutron-proton scattering”, *Physical Review Letters* **112**, 10.1103/PhysRevLett.112.202301 (2014).
- [52] P. Adlarson *et al.* (WASA-at-COSY Collaboration and SAID Data Analysis Center), “Neutron-proton scattering in the context of the $d^*(2380)$ resonance”, *Phys. Rev. C* **90**, 035204 (2014).
- [53] K. Wijesooriya *et al.* (Jefferson Lab), “Polarization Measurements in High-Energy Deuteron Photodisintegration”, *Phys. Rev. Lett.* **86**, 2975–2979 (2001), <https://link.aps.org/doi/10.1103/PhysRevLett.86.2975>.
- [54] M. Schwamb and H. Arenhövel, “The two-nucleon system in the Δ region including full meson retardation”, **603**, 10.1063/1.1436621 (2001).
- [55] Y. Kang, PhD thesis (University of Bonn, 1993).
- [56] *JLab timeline*, <https://www.jlab.org/about/visitors/history>, Accessed: 14.06.2022.
- [57] A. Accardi *et al.*, *Strong Interaction Physics at the Luminosity Frontier with 22 GeV Electrons at Jefferson Lab*, 2023, <https://arxiv.org/abs/2306.09360>.

- [58] C. E. Reece, “Continuous wave superconducting radio frequency electron linac for nuclear physics research”, *Phys. Rev. Accel. Beams* **19**, 124801 (2016), <https://link.aps.org/doi/10.1103/PhysRevAccelBeams.19.124801>.
- [59] R. Kazimi *et al.*, “CEBAF injector achieved world’s best beam quality for three simultaneous beam with a wide range of bunch charges”, in (July 2004), <https://www.osti.gov/biblio/827516>.
- [60] T. Siggins *et al.*, “Performance of a DC GaAs photocathode gun for the Jefferson lab FEL”, *Nuclear Instruments and Methods in Physics Research Section A: Accelerators, Spectrometers, Detectors and Associated Equipment* **475**, FEL2000: Proc. 22nd Int. Free Electron Laser Conference and 7th FEL Users Workshop, 549–553 (2001), <https://www.sciencedirect.com/science/article/pii/S0168900201015960>.
- [61] Y.-C. Chao *et al.*, “Achieving beam quality requirements for parity experiments at Jefferson Lab”, *Proceedings of EPAC 2004*, Lucerne, Switzerland (2004), <https://www.osti.gov/biblio/827526>.
- [62] R. Paschotta, *Pockels cells*, RP Photonics Encyclopedia, https://www.rp-photonics.com/pockels_cells.html (visited on 02/13/2025).
- [63] R. Flood *et al.*, *Helicity control board user’s guide*, Jefferson Science Associates, LLC, Nov. 2010.
- [64] L. Merminga, D. Douglas, and G. Krafft, “High-current energy-recovering electron linacs”, *Annual Review of Nuclear and Particle Science - ANNU REV NUCL PAR SCI* **53**, 387–429 (2003).
- [65] C. Leemann, D. Douglas, and G. Krafft, “The Continuous Electron Beam Accelerator Facility: CEBAF at the Jefferson Laboratory”, *Annu. Rev. Nucl. Part. Sci* **51**, 413–50 (2001).
- [66] Thomas Jefferson National Accelerator Facility - Office of Science Education, *Jefferson Lab Site Tour*, <https://education.jlab.org/sitetour/>, Accessed: 14.05.2024.
- [67] C. Leemann, “CEBAF - Design Overview and Project Status”, (1987), <https://www.osti.gov/biblio/834864>.
- [68] R. Legg, “Operating experience at CEBAF”, U.S. Department of Energy Technical Report, 10.2172/10153669 (1996), <https://www.osti.gov/biblio/10153669>.
- [69] V. Burkert *et al.*, “The CLAS12 Spectrometer at Jefferson Laboratory”, *Nuclear Instruments and Methods in Physics Research Section A: Accelerators, Spectrometers, Detectors and Associated Equipment* **959**, 163419 (2020).
- [70] D. Sober *et al.*, “The bremsstrahlung tagged photon beam in Hall B at JLab”, *Nuclear Instruments and Methods in Physics Research Section A: Accelerators, Spectrometers, Detectors and Associated Equipment* **440**, 263–284 (2000), <https://www.sciencedirect.com/science/article/pii/S0168900299007846>.
- [71] U. Timm, “Coherent bremsstrahlung of electrons in crystals”, *Fortschritte der Physik* **17**, 765–808 (1969).
- [72] The CLAS collaboration, “Kaon production on the deuteron using polarized photons”, PAC30 Proposal: PR-06-103 (2006).
- [73] H. Olsen and L. C. Maximon, “Photon and electron polarization in high-energy bremsstrahlung and pair production with screening”, *Phys. Rev.* **114**, 887–904 (1959).
- [74] P. L. Cole *et al.*, “The commissioning of the hall-B beamline of jefferson lab for coherently producing a beam of linearly-polarized photons”, in *Electromagnetic Interactions in Nuclear and Hadron Physics* (), pp. 688–697, https://www.worldscientific.com/doi/abs/10.1142/9789812777218_0070.

-
- [75] Thomas Jefferson National Accelerator Facility, *CLAS - photos*, <https://www.jlab.org/Hall-B/album/>, Accessed: 20.05.2024.
- [76] M. Mestayer *et al.*, “The CLAS drift chamber system”, *Nuclear Instruments and Methods in Physics Research Section A: Accelerators, Spectrometers, Detectors and Associated Equipment* **449**, 81–111 (2000), <https://www.sciencedirect.com/science/article/pii/S0168900200001510>.
- [77] *Eljen Technology*, *General purpose scintillators*, Accessed: 07.05.2024, <https://eljentechnology.com/products/plastic-scintillators/>.
- [78] Y. Sharabian *et al.*, “A new highly segmented start counter for the CLAS detector”, *Nuclear Instruments and Methods in Physics Research Section A: Accelerators, Spectrometers, Detectors and Associated Equipment* **556**, 246–258 (2006).
- [79] S. Taylor *et al.*, “The CLAS start counter”, *Nuclear Instruments and Methods in Physics Research*, 484–493 (2001).
- [80] G. Adams *et al.*, “The CLAS Cerenkov detector”, *Nuclear Instruments and Methods in Physics Research Section A: Accelerators, Spectrometers, Detectors and Associated Equipment* **465**, 414–427 (2001), <https://www.sciencedirect.com/science/article/pii/S0168900200013139>.
- [81] R. C. Fernow, *Introduction to experimental particle physics* (Cambridge University Press, 2022).
- [82] E. Smith *et al.*, “The time-of-flight system for CLAS”, *Nuclear Instruments and Methods in Physics Research Section A: Accelerators, Spectrometers, Detectors and Associated Equipment* **432**, 265–298 (1999), <https://www.sciencedirect.com/science/article/pii/S0168900299004842>.
- [83] V. Burkert *et al.*, *Photomultipliers for the electromagnetic shower calorimeter of the CEBAF large acceptance calorimeter*, tech. rep. CLAS-NOTE-92-009 (Jefferson Lab, Apr. 3, 1992).
- [84] M. Anghinolfi *et al.*, “Response to cosmic rays of the large-angle electromagnetic shower calorimeter of the CLAS detector”, *Nuclear Instruments and Methods in Physics Research Section A: Accelerators, Spectrometers, Detectors and Associated Equipment* **447**, 424–431 (2000), <https://www.sciencedirect.com/science/article/pii/S0168900299012875>.
- [85] *G13 CLAS information page*, https://clasweb.jlab.org/rungroups/g13/wiki/index.php/Main_Page, Accessed: 03.06.2024.
- [86] S. Christo, *The Jefferson Lab Hall B Cryotarget Page*, https://userweb.jlab.org/~christo/target_intro.html, Accessed: 13.03.2024.
- [87] M. Williams, D. Applegate, and C. A. Meyer, *Determining Momentum and Energy Corrections for g1c Using Kinematic Fitting*, tech. rep. CLAS-NOTE-04-017 (Jefferson Lab, June 2004).
- [88] K. Nakamura and (Particle Data Group), “Review of particle physics”, *Journal of Physics G: Nuclear and Particle Physics* **37**, 075021 (2010).
- [89] P. Mattione, “ $K^*(892)^0\Lambda$ and $K^+\Sigma^*(1385)^-$ Photoproduction on the Deuteron”, PhD thesis (Rice University, May 2011).
- [90] P. Mattione and D. Carman, *CLAS g13 Experiment Studies*, tech. rep. CLAS-NOTE-17-001 (Jefferson Lab, Jan. 2017).
- [91] N. Zachariou, “Determination of the Azimuthal Asymmetry of Deuteron Photodisintegration in the Photon-energy Region between 1.1 and 2.3 GeV”, MA thesis (The George Washington University, 2012).
- [92] R. A. Arndt *et al.*, “Updated analysis of NN elastic scattering to 3 GeV”, *Phys. Rev. C* **76**, 025209 (2007).

- [93] The George Washington University, *Scattering Analysis Interactive Dial-in facility (SAID)*, <https://gwdac.phys.gwu.edu/>.
- [94] G. B. Arfken, H. J. Weber, and F. E. Harris, *Mathematical Methods for Physicists, A Comprehensive Guide*, 7th ed. (2012).
- [95] M. Bashkanov, Email, Private communication, Feb. 2023.
- [96] A. Pastore, “An introduction to bootstrap for nuclear physics”, *Journal of Physics G: Nuclear and Particle Physics* **46**, 052001 (2019).
- [97] F. Afzal *et al.* (A2 Collaboration at MAMI), “First measurement using elliptically polarized photons of the double-polarization observable E for $\gamma p \rightarrow p\pi^0$ and $\gamma p \rightarrow n\pi^+$ ”, *Phys. Rev. Lett.* **132**, 121902 (2024), <https://link.aps.org/doi/10.1103/PhysRevLett.132.121902>.
- [98] M. Antonioli *et al.*, “The CLAS12 silicon vertex tracker”, *Nuclear Instruments and Methods in Physics Research Section A: Accelerators, Spectrometers, Detectors and Associated Equipment* **962**, 163701 (2020).
- [99] *Mitsubishi pitch fiber specifications*, Accessed: 05.08.2024, <https://mccfc.com/pitch-fiber/>.
- [100] *Evonik Industries AG, Rohacell[®] PMI foam specifications*, Accessed: 05.08.2024, <https://performance-foams.evonik.com/en/products-and-solutions/rohacell>.
- [101] A. Acker *et al.*, “The CLAS12 forward tagger”, *Nuclear Instruments and Methods in Physics Research Section A: Accelerators, Spectrometers, Detectors and Associated Equipment* **959**, 163475 (2020), <https://www.sciencedirect.com/science/article/pii/S0168900220300838>.
- [102] W. Rindler, *Introduction to Special Relativity*, 2nd ed. (Oxford University Press Higher Education Division, 1991).

Appendix A

Establishing the electron efficiency of CLAS12's Forward Tagger

This is a supplementary chapter detailing a calibration project undertaken in parallel with the work associated with the thesis topic. This work was in collaboration with a group assigned to CLAS12's calorimeter, as service to Jefferson Lab, a requirement of being a JLab user with access to JLab's wealth of experimental data.

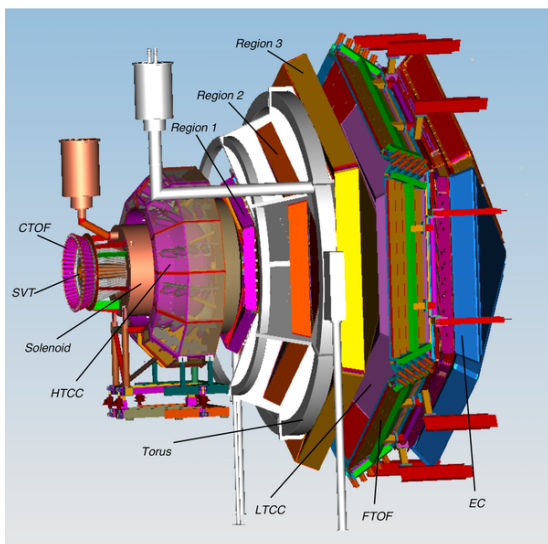


Fig. A.1 Commonly seen schematic layout of the CLAS12 design.

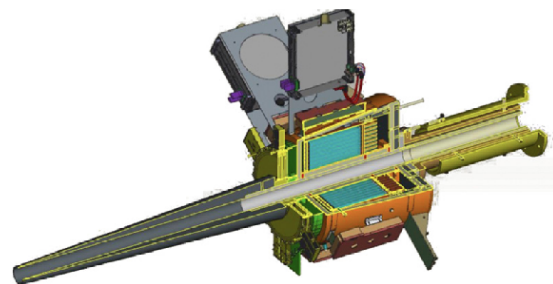


Fig. A.2 A 3D design of CLAS12's forward tagger, taken from [101]. The FT calorimeter is shown in cyan.

A.1 Experimental Setup

CLAS12, shown in Fig. A.1, is the upgraded version of CLAS, to pair with the 12 GeV CEBAF upgrade, capable of accepting these new beam energies. Many components of CLAS were recycled into CLAS12, however some new detectors and components were added, such as the forward tagger. The forward tagger is an important component of CLAS12, designed to detect both electrons and photons at polar angles (θ) of 2 to 5 degrees (outgoing from the target material) during CLAS12's experiments [101]. It consists of three main parts: The hodoscope (FT-Hodo), composed of plastic scintillators, and designed to distinguish between photons and electrons; the micromegas tracker (FT-Trk), used to precisely determine electron angles for track reconstruction; and, the focus of this service work project, the calorimeter (FT-cal), formed of an array of parallel lead tungstate (PbWO_4) crystals, cuboid in shape, and each 200 mm in length (individual crystal shown in Fig. A.4). To cover the aforementioned θ range, these scintillator crystals are arranged such that they surround the central Z-axis beamline. The square fronts of each crystal contribute to the calorimeter face, forming a pixelated ring (shown in Fig. A.3) that intercepts a low angular range.

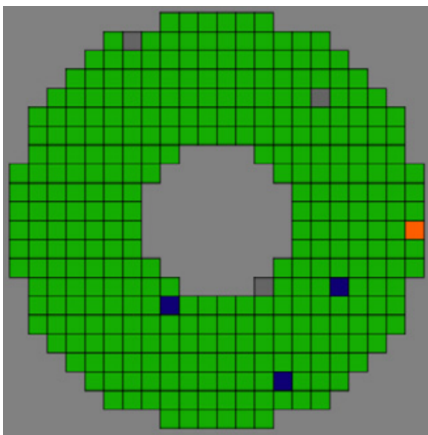


Fig. A.3 Layout of scintillators elements in the FT, from a noise analysis [101]. Colour represents the status of the crystal: green corresponds to a fully functional element, blue/orange to an element with noise below/above the typical range, and gray for no data recorded.



Fig. A.4 The assembly of a single FT-cal crystal, consisting of a $15 \times 15 \times 200$ mm block of lead tungstate coupled to a photo-diode and readout (downstream end) and LED (upstream end), and wrapped in reflective film.

The data for this analysis comes from Run Group A's Spring 2019 experimental data, which used an electron beam with an energy of 10.1998 GeV incident on a hydrogen target. This dataset contains 11.78 billion particle events worth of data.

A.2 Analysis

The electron detector efficiency is simply the ratio between successfully detected electrons and the total of electrons that hit the detector. This can be expressed mathematically in the following way:

$$\text{Efficiency} = \frac{\text{No. of electrons detected}}{\text{Total No. of electrons}} \quad (\text{A.1})$$

In order to observe the positional dependence of electron efficiency, this operation must be done with respect to XY position of electrons. This process therefore requires knowledge of the XY positions of all electrons that hit the FT. However, we do not have direct information on undetected electrons. Instead, we have to focus on a specific reaction channel in which we can reliably reconstruct an electron using 4-vector momentum conservation (see Appendix Sec. B on 4-vectors).

For this analysis, the reaction $ep \rightarrow (e')p\pi^+\pi^-$ was chosen and identified by selecting events where the forward detector detects one of each p , π^+ and π^- . To further ensure this, additional filter conditions include tight particle ID selection, and the Z component of particle vertices are selected to be between -6 cm and 0 cm. This is to ensure selected events are occurring inside the hydrogen target, which spans -5 to 0 cm in the Z-vertex (an extra cm is included within the cuts to allow for some inaccuracies). Missing electron mass ($MM^2(p\pi^+\pi^-)$) cuts were also applied, with limits defined by a fitted Gaussian function, which we be explained in more detail later. See thesis Chap. 5 for more detail on similar data selection techniques.

In this selected dataset, there are both events where the electron is detected, and events where the electron is missing - for which, a reconstruction is necessary. The electron can be reconstructed using momentum conserving 4-vector arithmetic as shown below:

$$\vec{P}_{e'} = \vec{P}_e + \vec{P}_H - \vec{P}_p - \vec{P}_{\pi^+} - \vec{P}_{\pi^-} \quad (\text{A.2})$$

Where \vec{P} represents momentum vectors associated with each subscript particle, including the incident electron beam, e the target hydrogen, H, the scattered electron e' , the proton, p , the positive pion, π^+ , and negative pion, π^- . This 4-vector reconstruction allows us to estimate the trajectory of the missing electron. However, the magnetic field in which the electron moves through must also be considered, as this causes charged particles to move in a spiraling path. The process of reconstructing an electron's path through a magnetic field is known as "swimming". Swimming is a necessary part

of CLAS12 vertex reconstruction in order to estimate the starting vertex of a detected particle, and record it into the CLAS12 data bank. In this calibration project, swimming must be done in the opposite direction, taking/creating a particle start vertex and momentum vector, and then "swimming" it forward to the detector, to determine where it lands. For this work, swimming corrections to the electron's path were implemented by Raffaella De Vita, based on the well known magnetic field maps.

To validate these swimming corrections, we can look only at detected electron events in our sample, and compare the XY hit position as reported by the forward tagger with a reconstructed position, created by taking the electron's momentum vector as it was recorded in the particle data banks, and applying these swimming corrections to its projected path to obtain an XY position at the Z-vertex of the forward tagger. We should expect these two positions to be identical, as the electron's momentum vector in the particle bank was calculated using the FT hit position, (as well as the energy deposited in the calorimeter) and by swimming this electron back to the reaction vertex using the same magnetic field map. Our calculated detector XY position merely involves the reverse operation, and so there should be no change. Upon populating two histograms, one with FT hit information and one with reconstructed XY positions using swimming, two perfectly identical histograms are created, showing that the correct swimming functions are being used. Fig. A.5 shows one of these FT hit position histograms, which demonstrates the acceptance of the FT.

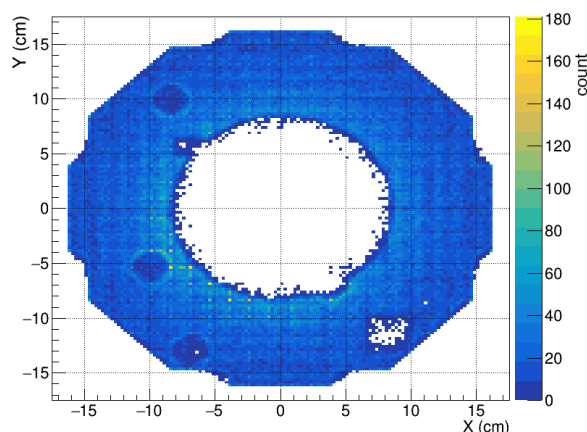


Fig. A.5 A histogram of detected electron positions by CLAS12's forward tagger in a sample of events from run group A's spring 2019 experimental run period. Dead crystals are visible as gaps in the acceptance.

With the now validated method of reconstruction via swimming, it's possible to estimate the XY position of "missing" (undetected) electrons. To better select the region of the FT, there is a requirement that these reconstructed electrons have a polar (θ) angle between 2 and 5 degrees,

and an energy between 1 and 5 GeV (the working energy range of the FT). The accuracy of this missing electron reconstruction can be checked by once again focusing on detected electron events, by comparing the detected electron FT position with a calculated position made as if this detected electron was missing. The result of this comparison is shown in Fig. A.6.

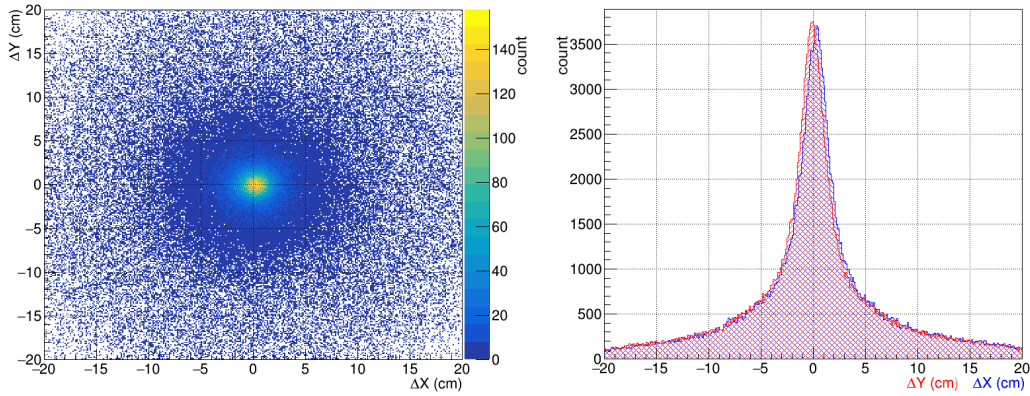


Fig. A.6 Histograms showing the difference between electron XY positions at the Z-vertex of the Forward Tagger as defined by either recorded FT hit position, or reconstructed electron position using a missing electron 4-vector created from $e p \rightarrow X p \pi^+ \pi^-$. Left shows the full 2D histogram of ΔY vs ΔX , right shows two overlapping 1D projections of the 2D plot, with ΔY in red, and ΔX in blue.

As can be seen by this comparison, there is a significant uncertainty in the reconstructed electron hit position. This is caused by inaccuracies in the particle reconstruction of p , π^+ and π^- , as well as misidentified events (to be addressed shortly). This uncertainty will carry over to the final calculation of FT electron efficiency.

Despite this inaccuracy, when performing the division operation (Eq. (A.1)), it's important that both the numerator and the denominator are consistent, with both associated histograms filled with reconstructed electron positions only. This consistency allows the two histograms to overlap correctly, such that detected electrons appear in the same XY position in both, allowing for a valid division that will not produce any negative/non-real values.

A.3 Formula to remove background contributions

This section will deal with background estimation and subtraction, a topic also addressed as part of the analysis of the main thesis topic (Chap. 5). So far, in this CLAS12 project, it has been shown how a histogram of the FT's effective electron efficiency can be calculated. However, performing this calculation with the current data will produce an apparent efficiency of around 30%, due to the

presence of background in the sample, corresponding to misidentified events which still exist in the data, despite our best selection efforts. The background is apparent when creating a histogram of missing electron mass (Fig. A.7).

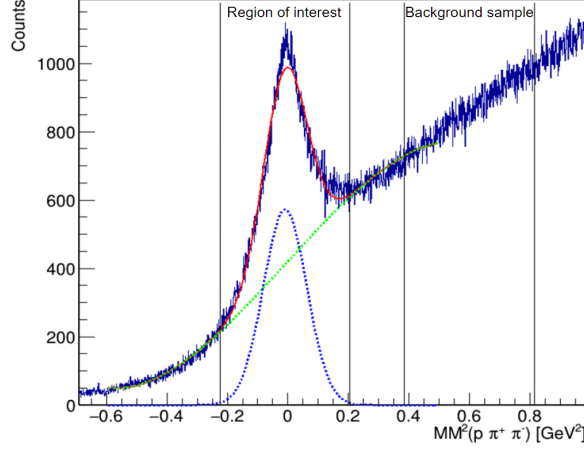


Fig. A.7 A histogram of missing electron mass (solid blue), showing how the electron mass peak is sitting on a shoulder of background. The histogram is fitted with a function summing a Gaussian and polynomial (red line), allowing the shape of both the peak and background to be separately defined by the Gaussian (blue dashed line) and polynomial (green dashed line) respectively. This in turn allows a region of data and a region of background to be defined.

Within the data set, there is data corresponding to the reaction of interest, with an associated "real" electron efficiency, Eff_{real} , that we wish to ultimately calculate. But there are also background events, which also have a calculable value of "efficiency", Eff_{BG} , which is technically meaningless, and not associated with any physical property. What is actually being calculated when we analyse this mixed dataset is an efficiency value, Eff_{mixed} , that lies somewhere between the two.

As an equation, this would be:

$$\text{Eff}_{real} = \frac{\text{Detected}_{real}}{\text{Total}_{real}} \Rightarrow \text{Detected}_{real} = \text{Eff}_{real} \times \text{Total}_{real} \quad (\text{A.3})$$

$$\text{Eff}_{BG} = \frac{\text{Detected}_{BG}}{\text{Total}_{BG}} \Rightarrow \text{Detected}_{BG} = \text{Eff}_{BG} \times \text{Total}_{BG} \quad (\text{A.4})$$

$$\text{Eff}_{mixed} = \frac{\text{Detected}_{mixed}}{\text{Total}_{mixed}} \Rightarrow \text{Detected}_{mixed} = \text{Eff}_{mixed} \times \text{Total}_{mixed} \quad (\text{A.5})$$

The desirable goal is to have a formula for Eff_{real} that only uses obtainable information. As shown in Fig. A.7, we can select a background sample away from the missing electron mass peak to obtain a

value of Eff_{BG} . Note that there is a major assumption being made here - that the value of Eff_{BG} does not vary with $MM^2(p\pi^+\pi^-)$ or θ_e . This assumption will be explored in the next section.

To begin deriving the background removal formula, it must first be understood that the number of real events and background events both sum to make the complete sample of mixed events in both the detected and undetected electron events:

$$\text{Detected}_{mixed} = \text{Detected}_{real} + \text{Detected}_{BG} \quad (\text{A.6})$$

$$\text{Total}_{mixed} = \text{Total}_{real} + \text{Total}_{BG} \quad (\text{A.7})$$

This information can then be substituted into Eq. (A.5) to make the following:

$$\text{Detected}_{BG} + \text{Detected}_{real} = \text{Eff}_{mixed} \times (\text{Total}_{BG} + \text{Total}_{real}) \quad (\text{A.8})$$

Then, Detected_{BG} can be substituted for Eq. (A.4).

$$(\text{Eff}_{BG} \times \text{Total}_{BG}) + \text{Detected}_{real} = \text{Eff}_{mixed} \times (\text{Total}_{BG} + \text{Total}_{real}) \quad (\text{A.9})$$

Expanding:

$$(\text{Eff}_{BG} \times \text{Total}_{BG}) + \text{Detected}_{real} = (\text{Eff}_{mixed} \times \text{Total}_{BG}) + (\text{Eff}_{mixed} \times \text{Total}_{real}) \quad (\text{A.10})$$

Rearranging:

$$\text{Detected}_{real} = (\text{Eff}_{mixed} \times \text{Total}_{BG}) + (\text{Eff}_{mixed} \times \text{Total}_{real}) - (\text{Eff}_{BG} \times \text{Total}_{BG}) \quad (\text{A.11})$$

Factorising:

$$\text{Detected}_{real} = \text{Total}_{BG}(\text{Eff}_{mixed} - \text{Eff}_{BG}) + (\text{Eff}_{mixed} \times \text{Total}_{real}) \quad (\text{A.12})$$

Dividing through by Total_{real} gives us:

$$\text{Eff}_{real} = \frac{\text{Detected}_{real}}{\text{Total}_{real}} = \frac{\text{Total}_{BG}}{\text{Total}_{real}}(\text{Eff}_{mixed} - \text{Eff}_{BG}) + \text{Eff}_{mixed} \quad (\text{A.13})$$

At this point, it is useful to define a signal ratio, R , where:

$$R = \frac{\text{Total}_{real}}{\text{Total}_{mixed}} = \frac{\text{Total}_{real}}{\text{Total}_{real} + \text{Total}_{BG}} \quad (\text{A.14})$$

Rearranging this:

$$\text{Total}_{BG} = \frac{\text{Total}_{real}}{R} - \text{Total}_{real} = \text{Total}_{real} \left(\frac{1}{R} - 1 \right) = \text{Total}_{real} \left(\frac{1-R}{R} \right) \quad (\text{A.15})$$

Finally, substituting this back into Eq. (A.13):

$$\text{Eff}_{real} = \left(\frac{1-R}{R} \right) (\text{Eff}_{mixed} - \text{Eff}_{BG}) + \text{Eff}_{mixed} \quad (\text{A.16})$$

This gives us a formula to calculate Eff_{real} , requiring only Eff_{mixed} , which as shown previously we can already calculate, Eff_{BG} , which requires calculating effective efficiency of a background sample, and R , which requires an estimate of the fraction of events of interest compared to all events in the mixed data. This formula tells us that as the signal ratio, R , approaches 1 (meaning all signal, no background) the true electron efficiency, Eff_{real} , becomes equal to Eff_{mixed} . This is logical, as the real data and the mixed data become identical datasets at $R = 1$. However as R approaches 0, the formula becomes invalid, as in this case there are no events of interest to analyse.

A.4 Establishing R

In order to estimate R , the fraction of events of interest against all events in the sample, a function was fitted to the missing electron mass histogram (using a χ^2 minimization fitting algorithm) to attempt to extract its apparent features. This allows the areas under each feature to be estimated via integration, and therefore the value of R . After trialing various functions, a Gaussian function was chosen to define the peak, and the background was defined with a third order polynomial. Examples of these fits can be seen in both Fig. A.7 and Fig. A.8. Defining the signal in this way also means defining the region of interest, which can now be said to be the mean of the Gaussian function $\pm 3\sigma$.

It can be seen in Fig. A.7 and Fig. A.8 that the Gaussian function does not manage to reach the full height of the apparent peak, however the background shoulder seems to be well captured within the area of interest. Therefore it was decided to not use the area under the Gaussian function when

calculating R , instead only considering the area under the histogram, and the area under the third order polynomial that defines the background. Therefore:

$$R = \frac{\text{Area}_{hist} - \text{Area}_{BG}}{\text{Area}_{hist}} = 1 - \frac{\text{Area}_{BG}}{\text{Area}_{hist}} \quad (\text{A.17})$$

Hence, through error propogation, the error associated in R is given by:

$$\delta R = \frac{\text{Area}_{BG}}{\text{Area}_{hist}} \sqrt{\left(\frac{\delta \text{Area}_{BG}}{\text{Area}_{BG}}\right)^2 + \left(\frac{\delta \text{Area}_{hist}}{\text{Area}_{hist}}\right)^2} \quad (\text{A.18})$$

Where δArea_{BG} is obtained from an integral error algorithm that respects the original function fit parameter errors, and $\delta \text{Area}_{hist}$ is simply the square root of the number of events found in the region of interest, $\delta \text{Area}_{hist} = \sqrt{\text{Area}_{hist}}$ (assuming Poisson statistics). This allows for further simplification:

$$\delta R = \frac{\text{Area}_{BG}}{\text{Area}_{hist}} \sqrt{\left(\frac{\delta \text{Area}_{BG}}{\text{Area}_{BG}}\right)^2 + \frac{1}{\text{Area}_{hist}}} \quad (\text{A.19})$$

A.5 Establishing Eff_{BG}

As previously mentioned, a major assumption being made is that Eff_{BG} does not vary with $\text{MM}^2(p\pi^+\pi^-)$, and therefore the value of Eff_{BG} , sampled at some arbitrary region away from the missing electron mass peak, will be the same inside the region of interest. To investigate this, and possibly obtain a better estimate of Eff_{BG} , several samples of background data are taken by binning in $\text{MM}^2(p\pi^+\pi^-)$. These bins must be taken far away enough from the missing electron mass peak to ensure they are purely background, otherwise the apparent value of Eff_{BG} would begin approaching Eff_{mixed} . After obtaining values of Eff_{BG} from these sample bins, it can be checked whether a trend emerges, in which case the value of Eff_{BG} in the region of interest can be obtained through fitting a function to the trend. This method was successfully tested and implemented in simulated data, in which the background was artificially created by taking a certain fraction of simulated events, and applying some randomisation to the vectors of p , π^+ , π^- . The result of this is shown in Fig. A.9. However, when applying this method to the real dataset, it was found that values on the left-hand side of the region of interest were much more imprecise when compared to the right-hand side, due to small statistics. The extracted values were also inconsistently high, suggesting that they were being still being influenced by the real data, despite the assumption that it was entirely contained by $\pm 3\sigma$ of a Gaussian function. It was

therefore decided that the best estimate of Eff_{BG} should only consider the background information at the right-hand side of the peak, and a value was acquired by averaging these right-hand samples of Eff_{BG} .

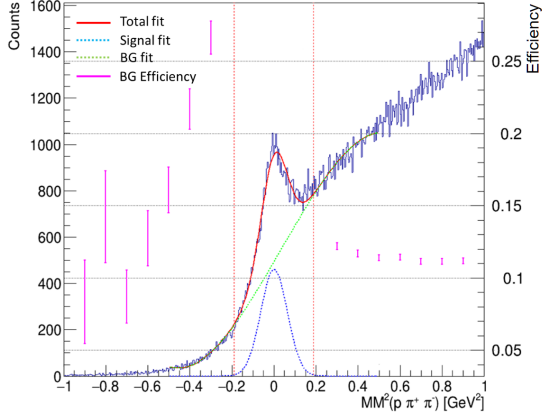


Fig. A.8 Another histogram of missing electron mass (solid blue), fitted with the same functions as before. Values of background efficiency (pink) are calculated from binned $MM^2(p\pi^+\pi^-)$ samples of data, taken either side of the region of interest (red dashed lines).

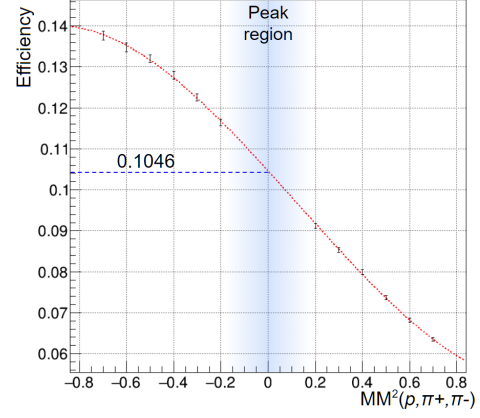


Fig. A.9 A background efficiency analysis on a sample of simulated data, in which a background was artificially created. Values of efficiency follow a clear trend, allowing for the Eff_{BG} value behind the signal to be estimated via fitting a polynomial.

The final method settled on involved taking six $MM^2(p\pi^+\pi^-)$ bins of width 0.1 GeV, with the first centred at 0.4 GeV, and the rest following at increments of 0.1. In each of these $MM^2(p\pi^+\pi^-)$ bins, the integral of the numerator histogram is divided by the integral of the denominator histogram, and a value of Eff_{BG} is obtained from each. These six values are then averaged to obtain the final estimation of Eff_{BG} , such that:

$$\text{Eff}_{BG} = \frac{1}{6}(\text{Eff}_{BG1} + \text{Eff}_{BG2} + \dots + \text{Eff}_{BG5} + \text{Eff}_{BG6}) \quad (\text{A.20})$$

Through error propagation, it follows that the error in Eff_{BG} is given by:

$$\delta\text{Eff}_{BG} = \frac{1}{6}\sqrt{\text{Eff}_{BG1}^2 + \text{Eff}_{BG2}^2 + \dots + \text{Eff}_{BG5}^2 + \text{Eff}_{BG6}^2} \quad (\text{A.21})$$

A.6 Considering Electron Theta

One final assumption that must be addressed is the assumption that all of the previous calculated parameters are constant throughout electron polar scattering angles, θ_e . It can be assumed that nothing changes with the radial angle, ϕ_e , as the reaction has a rotational symmetry. However a larger θ_e correlates to a longer electron path, and a more scattered electron. This can be addressed by binning in terms of θ_e , and repeating the full process to calculate R , Eff_{BG} and Eff_{mixed} , on each of these bins. The resulting values can then be plotted against θ_e , and fitted with polynomial functions which relate each parameter to θ_e . The full process of this is shown in A.10 These radial functions can then be converted into the form of 2D histograms of X and Y positions on the FT plane. This means that the final equation to calculate Eff_{real} (Eq. (A.16)) has a histogram for each term, and the entire calculation is a histogram-wise operation.

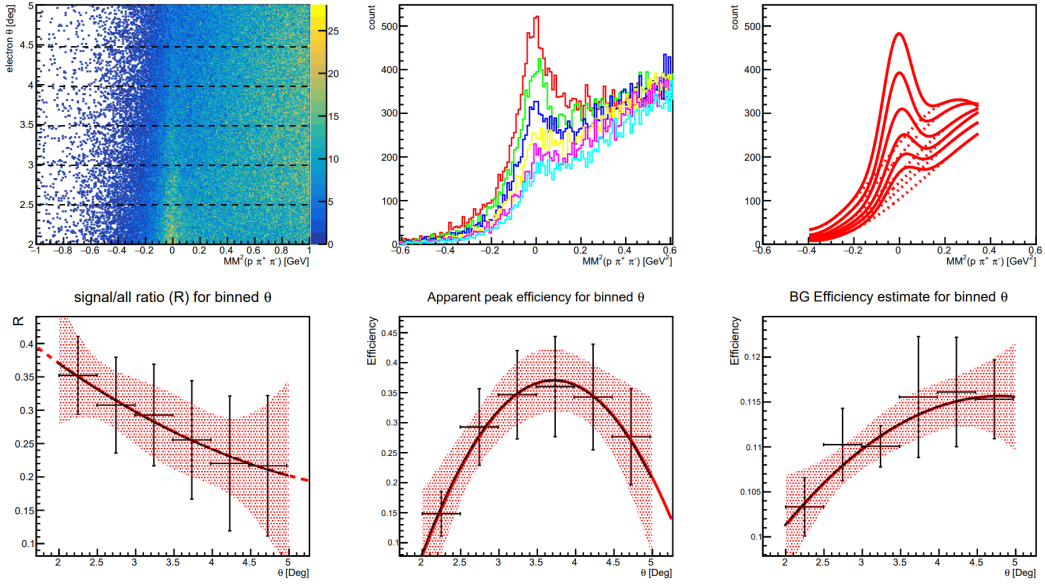


Fig. A.10 All steps involved in calculating electron efficiency with respect to θ_e . Top left: 2D histogram of θ_e vs $\text{MM}^2(p\pi^+\pi^-)$, showing where data is divided into 6 bins of θ_e . Top centre: Projections of $\text{MM}^2(p\pi^+\pi^-)$, one for each bin of θ_e , as defined by the previous histogram. Top right: Each previous histogram is fitted with a Gaussian and third order polynomial to identify peak regions and background ratios. With this information it's possible to obtain calculations of the signal-to-all ratio, R (bottom left), apparent efficiency, Eff_{mixed} (bottom centre), and background efficiency, Eff_{BG} (bottom right), for each of the defined θ_e bins, with associated errors. A second order polynomial function is fitted to each of these variables, with 70% confidence intervals shown as a red area.

A.7 Results

The end result can finally be calculated with histogram operations following Eq. (A.16). This can be displayed as a histogram of X vs Y, which shows a map of calculated efficiency across the detector face, which is useful for visualising specific defects in the detector, shown by regions of lower efficiency. Alternatively, the result can be shown as a 1D histogram of efficiency against θ_e , which allows the uncertainty to be displayed with the result. Both of these visualisations of the result are shown in Fig. A.11.

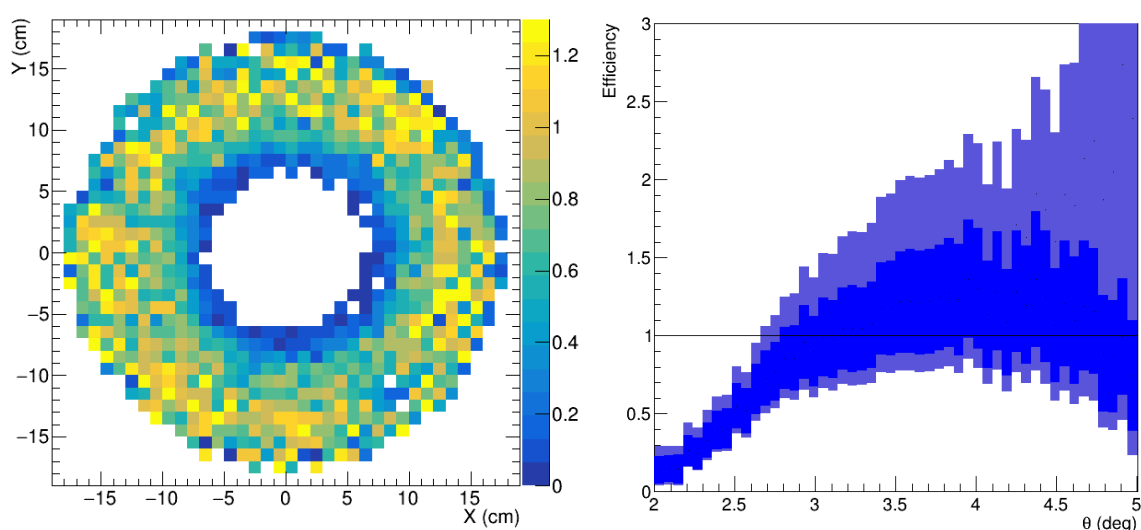


Fig. A.11 Final results of the FT electron efficiency calculation process. Left shows efficiency across X and Y positions of the FT, in which the lower efficiency regions corresponding to dead crystals is visible. Right shows this same efficiency as a function of θ_e . The dark blue region represents statistical uncertainty. The larger light blue region includes additionally the confidence in the θ_e functions for R , Eff_{mixed} and Eff_{BG} .

The result suggest that, within statistics, the forward tagger's electron efficiency is consistently close to 1, except for the region closest to the centre. This is expected, as electrons in a "shower" can leak out of crystals they initially travel through, which exit the FT if said crystals are at the edge of the detector. Electrons leaking into surrounding crystals may also lead to a more smeared result. We also expect a lower amount of electrons reaching the lower angle region of the FT due to the radiation shielding in place to block Møller electrons [101]. In the 2D XY histogram, there are regions of lower efficiency corresponding to dead crystals, as seen in the histogram of forward tagger acceptance (Fig. A.5). However, there is a lot of statistical noise in the result which makes this harder to see. This statistical uncertainty is visualised more in the 1D θ_e histogram, showing very large error bars,

especially at higher values of θ_e , where there is less data. In conclusion, this method of determining electron efficiency has yielded expected results but with large uncertainties. The precision of this result could be improved by using a larger dataset, or having a cleaner signal, possibly by improved background reduction techniques. This work will be continued by the group assigned to calorimeter analysis at JLab.

Appendix B

Relativistic Kinematics

This appendix is a supplementary chapter giving a basic overview of relativistic kinematics, one of the foundational concepts necessary for hadron and particle physics. In such scientific fields, we typically deal with particles moving at relativistic speeds. This is a way of saying that they move close to the speed of light, c , and hence must be considered through the lens of special relativity. Special relativity states that c is a constant value ($2.998 \times 10^8 \text{ ms}^{-1}$) in every inertial frame. The consequences of this are counter-intuitive from our non-relativistic perspective.

As an every-day example of relativity, if a moving car is overtaken by a slightly faster car, from each driver's relative perspective, the other car would pass by slowly. But from the frame of reference of a person standing at the side of the road, both cars zoom past with high velocity. However, imagine one car moving at half the speed of light. Special relativity tells us an observer in this car would still measure c to be the same value as the stationary observer (here, stationary means in the Earth's frame of reference).

To show this mathematically, consider two inertial frames, S and S', where S' moves at velocity, v , with respect to S. If the axes of both frames are aligned such that relative motion is confined to the x or x' direction, and both systems are centred on each other at $t = t' = 0$, then S can be transformed to S' in the following way [4, 102]:

$$\begin{aligned} x' &= \gamma(x - vt) \\ y' &= y \\ z' &= z \\ t' &= \gamma(t - vx/c^2) \end{aligned} \quad \text{where } \gamma = \frac{1}{\sqrt{1 - v^2/c^2}} \quad (\text{B.1})$$

This is known as Lorentz transformation, where γ is known as the Lorentz factor, which has a negligible effect until v approaches c . Note that as S' moves at velocity v with respect to S, S therefore moves at $-v$ with respect to S'. Thus the inverse operation to transform from S' to S is made by substituting v with $-v$ in equation (B.1).

These frame transformations have two important consequences; length contraction and time dilation. Length contraction is the phenomena of moving objects being shortened along the direction of motion. This is important for the application of particle physics, as accelerator and detector components have a shorter effective length from the perspective of relativistic particles, which must be taken into account during construction. Time dilation is the phenomena of time appearing to move slower for a moving object from the perspective of outsider observers. This again plays a role in particle physics; the faster particles move, the longer it takes for them to decay.

Special relativity unifies space and time into a four-dimensional continuum known as space-time. To handle this mathematically, we introduce 4-vectors, which combine spatial and temporal components. For example, a 4-position vector is given by:

$$x^\mu = (ct, x, y, z) \quad (\text{B.2})$$

Here, the index μ is a convention of lorentz vectors that denotes that there are four components, 0 to 3, where the 0th (x^0) component is time. Time, t , is multiplied by the speed of light, c , to have x^0 in units of length, the same as the spatial terms. ct thus represents the distance light travels during time t .

Velocity, v , is defined as the differential of position with respect to time, $\frac{dx}{dt}$. But to derive the 4-velocity vector, u^μ , we can't simply use time, as time is relative, as discussed. Instead we define *proper time*, τ , which is time as measured in the frame of the vector relative to the observer. An infinitesimal interval of, $d\tau$ is related to dt by $d\tau = \frac{dt}{\gamma}$, which is a mathematical description of time dilation. Now, 4-velocity can be defined as:

$$u^\mu = \frac{dx^\mu}{d\tau} \quad (\text{B.3})$$

Applying this to both time and space components separately:

Time component:

$$u^0 = \frac{d(ct)}{d\tau} = c \frac{dt}{d\tau} = c\gamma \quad (\text{B.4})$$

Spatial components:

$$u^i = \frac{dx^i}{d\tau} = \frac{dx^i}{dt} \frac{dt}{d\tau} = v^i \gamma \quad \text{where } i = 1, 2, 3 \quad (\text{B.5})$$

Therefore:

$$u^\mu = \gamma(c, v_x, v_y, v_z) \quad (\text{B.6})$$

An interesting property of the velocity 4-vector is that its magnitude is equal to c , as shown below:

$$u \cdot u = \gamma^2 (c^2, \vec{v} \cdot \vec{v}) = c^2 \gamma^2 (1 - \vec{v} \cdot \vec{v} / c^2) = c^2 \quad (\text{B.7})$$

$$|u| = c$$

This is an invariant value, meaning it does not change with a Lorentz transformation, and is the same in all inertial frames. An intuitive way to understand this is to realise that a fundamental property of the universe is that everything moves through spacetime at a constant speed of c . A stationary object simply has its 4-velocity orientated entirely in the time direction. This can also help in understanding time dilation, as for an object to gain any velocity in spatial directions, it must "trade" some of its velocity in the time direction to maintain this constant magnitude.

Next consider 4-momentum, p^μ . We know that in the familiar world of Newtonian physics, momentum is simply (mass) \times (velocity). Let's once again apply this logic to the spatial and time components separately.

Time component:

$$p^0 = mu^0 = mc\gamma \quad (\text{B.8})$$

Spatial components:

$$p^i = mu^i = mv^i\gamma \quad (\text{B.9})$$

Therefore:

$$p^\mu = \gamma(mc, p_x, p_y, p_z) \quad (\text{B.10})$$

Taking the magnitude of the 4-momentum vector:

$$\begin{aligned} p \cdot p &= m^2 p \cdot p = m^2 c^2 \\ |p| &= mc \end{aligned} \quad (\text{B.11})$$

The momentum 4-vector is a very powerful tool in particle physics, as momentum is conserved throughout collisions, and 4-momentum is an invariant value, agreed by all inertial frames, demonstrated by Eq. B.11. A common application of this is through the "missing mass" technique, where a "missing" (undetected) particle can be reconstructed as a 4-vector by considering the net of all other reactant and product particle 4-vectors.

In classical physics, kinetic energy is related to momentum by $E = p^2/2m$, however the implication of 4-momentum is that there is a component of momentum, and therefore energy, in the time direction. just by virtue of a particle having mass. This is in essence the meaning of the famous energy-mass relationship, $E = mc^2$, one of the cornerstones of special relativity. Under this interchangeability, if a particle has energy in units of eV, then it's mass can be given in units of eV/c^2 .

If we consider a stationary (at rest) particle ($v = 0, \gamma = 1$), then we can say it is timelike, meaning the only non-zero component of p^μ is $p^0 = mc$. This is known as rest mass, or rest energy. A particle's total energy is the sum of its rest energy and energy created by spatial momentum as given by the following relativistic relationship:

$$E = \sqrt{p^2c^2 + m^2c^4} \quad (\text{B.12})$$

Note that there are many (and more formal) ways to derive the formulae given in this section (see [102]), however for the purposes of this thesis, it is only necessary to understand how special relativity is necessary for the analysis of particle physics.

Appendix C

Supplementary Formulae

C.1 DOCA formula

Follows from section 5.2.2.

For two non-intersecting 3D lines given by:

$$\begin{cases} \vec{v}_1 = \vec{u}_1 + t_1 \hat{u}_1 \\ \vec{v}_2 = \vec{u}_2 + t_2 \hat{u}_2 \end{cases}$$

The vector between two respective points is given by:

$$\Delta \vec{v} = \vec{v}_1 - \vec{v}_2$$

The distance $|\Delta \vec{v}|$ is minimised when:

$$\begin{cases} \Delta \vec{v} \cdot \hat{u}_1 = 0 \\ \Delta \vec{v} \cdot \hat{u}_2 = 0 \end{cases}$$

To calculate the corresponding vectors, \vec{v}_1 and \vec{v}_2 , that meet this condition, solve for t_1 or t_2 , as follows:

$$\begin{cases} \Delta \vec{v} \cdot \hat{u}_1 = (\vec{v}_1 - \vec{v}_2) \cdot \hat{u}_1 = 0 \\ \Delta \vec{v} \cdot \hat{u}_2 = (\vec{v}_1 - \vec{v}_2) \cdot \hat{u}_2 = 0 \end{cases}$$

$$\begin{cases} ((\vec{u}_1 + t_1 \hat{u}_1) - (\vec{u}_2 + t_2 \hat{u}_2)) \cdot \hat{u}_1 = 0 \\ ((\vec{u}_1 + t_1 \hat{u}_1) - (\vec{u}_2 + t_2 \hat{u}_2)) \cdot \hat{u}_2 = 0 \end{cases}$$

$$\begin{cases} \vec{u}_1 \cdot \hat{u}_1 + t_1 \hat{u}_1 \cdot \hat{u}_1 - \vec{u}_2 \cdot \hat{u}_1 - t_2 \hat{u}_2 \cdot \hat{u}_1 = 0 \\ \vec{u}_1 \cdot \hat{u}_2 + t_1 \hat{u}_1 \cdot \hat{u}_2 - \vec{u}_2 \cdot \hat{u}_2 - t_2 \hat{u}_2 \cdot \hat{u}_2 = 0 \end{cases}$$

$$\begin{cases} t_1 = t_2 \hat{u}_1 \cdot \hat{u}_2 + \vec{u}_2 \cdot \hat{u}_1 - \vec{u}_1 \cdot \hat{u}_1 \\ t_2 = t_1 \hat{u}_1 \cdot \hat{u}_2 + \vec{u}_1 \cdot \hat{u}_2 - \vec{u}_2 \cdot \hat{u}_2 \end{cases}$$

$$\begin{cases} t_1 = (t_1 \hat{u}_1 \cdot \hat{u}_2 + \vec{u}_1 \cdot \hat{u}_2 - \vec{u}_2 \cdot \hat{u}_2) \hat{u}_1 \cdot \hat{u}_2 + \vec{u}_2 \cdot \hat{u}_1 - \vec{u}_1 \cdot \hat{u}_1 \\ t_2 = (t_2 \hat{u}_1 \cdot \hat{u}_2 + \vec{u}_2 \cdot \hat{u}_1 - \vec{u}_1 \cdot \hat{u}_1) \hat{u}_1 \cdot \hat{u}_2 + \vec{u}_1 \cdot \hat{u}_2 - \vec{u}_2 \cdot \hat{u}_2 \end{cases}$$

$$\begin{cases} t_1 - t_1 (\hat{u}_1 \cdot \hat{u}_2)^2 = \hat{u}_1 \cdot \hat{u}_2 (\vec{u}_1 \cdot \hat{u}_2 - \vec{u}_2 \cdot \hat{u}_2) + \vec{u}_2 \cdot \hat{u}_1 - \vec{u}_1 \cdot \hat{u}_1 \\ t_2 - t_2 (\hat{u}_1 \cdot \hat{u}_2)^2 = \hat{u}_1 \cdot \hat{u}_2 (\vec{u}_2 \cdot \hat{u}_1 - \vec{u}_1 \cdot \hat{u}_1) + \vec{u}_1 \cdot \hat{u}_2 - \vec{u}_2 \cdot \hat{u}_2 \end{cases}$$

$$\begin{cases} t_1 = \frac{\hat{u}_1 \cdot \hat{u}_2 (\vec{u}_1 \cdot \hat{u}_2 - \vec{u}_2 \cdot \hat{u}_2) + \vec{u}_2 \cdot \hat{u}_1 - \vec{u}_1 \cdot \hat{u}_1}{1 - (\hat{u}_1 \cdot \hat{u}_2)^2} \\ t_2 = \frac{\hat{u}_1 \cdot \hat{u}_2 (\vec{u}_2 \cdot \hat{u}_1 - \vec{u}_1 \cdot \hat{u}_1) + \vec{u}_1 \cdot \hat{u}_2 - \vec{u}_2 \cdot \hat{u}_2}{1 - (\hat{u}_1 \cdot \hat{u}_2)^2} \end{cases}$$

C.2 $C_{x'}$ sideband subtraction

Follows from section 5.3.7.

$$C_{x',\text{raw}} = \left(\frac{\text{Area}_{\text{hist}} - \text{Area}_{\text{pol}}}{\text{Area}_{\text{hist}}} \times C_{x'} \right) + \left(\frac{\text{Area}_{\text{pol}}}{\text{Area}_{\text{hist}}} \times C_{x',\text{BG}} \right)$$

$$C_{x'} = \frac{\text{Area}_{\text{hist}}}{\text{Area}_{\text{hist}} - \text{Area}_{\text{pol}}} \left(C_{x',\text{raw}} - \frac{\text{Area}_{\text{pol}} \times C_{x',\text{BG}}}{\text{Area}_{\text{hist}}} \right)$$

$$C_{x'} = \frac{C_{x',\text{raw}} \times \text{Area}_{\text{hist}}}{\text{Area}_{\text{hist}} - \text{Area}_{\text{pol}}} - \left(\frac{\text{Area}_{\text{pol}} \times C_{x',\text{BG}}}{\text{Area}_{\text{hist}}} \times \frac{\text{Area}_{\text{hist}}}{\text{Area}_{\text{hist}} - \text{Area}_{\text{pol}}} \right)$$

$$C_{x'} = \frac{C_{x',\text{raw}} \times \text{Area}_{\text{hist}}}{\text{Area}_{\text{hist}} - \text{Area}_{\text{pol}}} - \frac{\text{Area}_{\text{pol}} \times C_{x',\text{BG}}}{\text{Area}_{\text{hist}} - \text{Area}_{\text{pol}}}$$

$$C_{x'} = \frac{C_{x',\text{raw}} \text{Area}_{\text{hist}} - C_{x',\text{BG}} \text{Area}_{\text{pol}}}{\text{Area}_{\text{hist}} - \text{Area}_{\text{pol}}}$$

C.2.1 Deriving $\delta C_{x'}$

$$\delta C_{x'} = \sqrt{\left(\frac{\partial C_{x'}}{\partial \text{Area}_{\text{pol}}} \delta \text{Area}_{\text{pol}} \right)^2 + \left(\frac{\partial C_{x'}}{\partial \text{Area}_{\text{hist}}} \delta \text{Area}_{\text{hist}} \right)^2 + \left(\frac{\partial C_{x'}}{\partial C_{x',\text{raw}}} \delta C_{x',\text{raw}} \right)^2 + \left(\frac{\partial C_{x'}}{\partial C_{x',\text{BG}}} \delta C_{x',\text{BG}} \right)^2}$$

Partial derivative of Area_{pol}

Using quotient rule:

$$\frac{\partial C_{x'}}{\partial \text{Area}_{\text{pol}}} = \frac{-\frac{\partial v}{\partial \text{Area}_{\text{pol}}} u + \frac{\partial u}{\partial \text{Area}_{\text{pol}}} v}{v^2}$$

$$u = C_{x',\text{raw}} \text{Area}_{\text{hist}} - C_{x',\text{BG}} \text{Area}_{\text{pol}} \quad \frac{\partial u}{\partial \text{Area}_{\text{pol}}} = -C_{x',\text{BG}}$$

$$v = \text{Area}_{\text{hist}} - \text{Area}_{\text{pol}} \quad \frac{\partial v}{\partial \text{Area}_{\text{pol}}} = -1$$

$$\begin{aligned} \frac{\partial C_{x'}}{\partial \text{Area}_{\text{pol}}} &= \frac{(C_{x',\text{raw}} \text{Area}_{\text{hist}} - C_{x',\text{BG}} \text{Area}_{\text{pol}}) - C_{x',\text{BG}} (\text{Area}_{\text{hist}} - \text{Area}_{\text{pol}})}{(\text{Area}_{\text{hist}} - \text{Area}_{\text{pol}})^2} \\ &= \frac{\text{Area}_{\text{hist}} (C_{x',\text{raw}} - C_{x',\text{BG}})}{(\text{Area}_{\text{hist}} - \text{Area}_{\text{pol}})^2} \end{aligned}$$

Partial derivative of Area_{hist}

Using quotient rule:

$$\frac{\partial C_{x'}}{\partial \text{Area}_{hist}} = \frac{-\frac{\partial v}{\partial \text{Area}_{hist}}u + \frac{\partial u}{\partial \text{Area}_{hist}}v}{v^2}$$

$$\begin{aligned} u &= C_{x',raw}\text{Area}_{hist} - C_{x',BG}\text{Area}_{pol} & \frac{\partial u}{\partial \text{Area}_{hist}} &= C_{x',raw} \\ v &= \text{Area}_{hist} - \text{Area}_{pol} & \frac{\partial v}{\partial \text{Area}_{hist}} &= 1 \end{aligned}$$

$$\begin{aligned} \frac{\partial C_{x'}}{\partial \text{Area}_{hist}} &= \frac{-(C_{x',raw}\text{Area}_{hist} - C_{x',BG}\text{Area}_{pol}) + C_{x',raw}(\text{Area}_{hist} - \text{Area}_{pol})}{(\text{Area}_{hist} - \text{Area}_{pol})^2} \\ &= \frac{\text{Area}_{pol}(C_{x',BG} - C_{x',raw})}{(\text{Area}_{hist} - \text{Area}_{pol})^2} \end{aligned}$$

Partial derivative of $C_{x',raw}$

$$\frac{\partial C_{x'}}{\partial C_{x',raw}} = \frac{\text{Area}_{hist}}{\text{Area}_{hist} - \text{Area}_{pol}}$$

Partial derivative of $C_{x',BG}$

$$\frac{\partial C_{x'}}{\partial C_{x',BG}} = \frac{-\text{Area}_{pol}}{\text{Area}_{hist} - \text{Area}_{pol}}$$

Combining

$$\delta C_{x'} = \sqrt{\left[\frac{\text{Area}_{hist}(C_{x',raw} - C_{x',BG})}{(\text{Area}_{hist} - \text{Area}_{pol})^2} \delta \text{Area}_{pol} \right]^2 + \left[\frac{\text{Area}_{pol}(C_{x',BG} - C_{x',raw})}{(\text{Area}_{hist} - \text{Area}_{pol})^2} \delta \text{Area}_{hist} \right]^2 + \left[\frac{\text{Area}_{hist}}{\text{Area}_{hist} - \text{Area}_{pol}} \delta C_{x',raw} \right]^2 + \left[\frac{-\text{Area}_{pol}}{\text{Area}_{hist} - \text{Area}_{pol}} \delta C_{x',BG} \right]^2}$$

C.2.2 Origins of Variable Errors **δArea_{pol} :**

After fitting the full function (Gaussian + Polynomial) via a χ^2 algorithm, elements of the fit parameters and covariance matrix corresponding to the polynomial are extracted, and used to calculate error via an algorithm (see TF1::IntegralError() function description in CERN ROOT documentation for more information).

δArea_{hist} :

Error is taken to be $\sqrt{\text{Area}_{hist}}$, based on Poisson statistics.

$\delta C_{x',\text{raw}}$ and $\delta C_{x',\text{BG}}$:

Taken as the standard deviation of Gaussian functions fitted to the corresponding overlaid (fixed θ_N) $C_{x'}$ functions in bins of E_γ . Process shown in Section 5.3.9.

